

AD _____

Award Number: W81XWH-11-1-0423

TITLE: "Development of a Dedicated Radiotherapy Unit with Real-Time Image Guidance and Motion Management for Accelerated Partial Breast Irradiation"

PRINCIPAL INVESTIGATOR: Dr. K.S. Clifford Chao

CONTRACTING ORGANIZATION: The New Year Presbyterian Hospital
525 East 68th Street, Box 88
New York, N.Y. 10065

REPORT DATE: August 2012

TYPE OF REPORT: Annual

PREPARED FOR: U.S. Army Medical Research and Materiel Command
Fort Detrick, Maryland 21702-5012

DISTRIBUTION STATEMENT: Approved for Public Release;
Distribution Unlimited

The views, opinions and/or findings contained in this report are those of the author(s) and should not be construed as an official Department of the Army position, policy or decision unless so designated by other documentation.

| | | | | | |
|---|-------------------------|----------------------------|---|--|---|
| REPORT DOCUMENTATION PAGE | | | | <i>Form Approved</i> <i>OMB No. 0704-0188</i> | |
| Public reporting burden for this collection of information is estimated to average 1 hour per response, including the time for reviewing instructions, searching existing data sources, gathering and maintaining the data needed, and completing and reviewing this collection of information. Send comments regarding this burden estimate or any other aspect of this collection of information, including suggestions for reducing this burden to Department of Defense, Washington Headquarters Services, Directorate for Information Operations and Reports (0704-0188), 1215 Jefferson Davis Highway, Suite 1204, Arlington, VA 22202-4302. Respondents should be aware that notwithstanding any other provision of law, no person shall be subject to any penalty for failing to comply with a collection of information if it does not display a currently valid OMB control number. PLEASE DO NOT RETURN YOUR FORM TO THE ABOVE ADDRESS. | | | | | |
| 1. REPORT DATE 01-01-00 | | 2. REPORT TYPE A | | 3. DATES COVERED 01-01-00 to 01-01-00 | |
| 4. TITLE AND SUBTITLE Development of a Dedicated Radiotherapy Unit with Real-Time Image Guidance and Management for Accelerated Partial Breast Irradiation | | | | 5a. CONTRACT NUMBER | |
| | | | | 5b. GRANT NUMBER W81XWH-11-1-0423 | |
| | | | | 5c. PROGRAM ELEMENT NUMBER | |
| 6. AUTHOR(S) Dr. K.S. Clifford Chao E-Mail: clc9026@nyp.org | | | | 5d. PROJECT NUMBER | |
| | | | | 5e. TASK NUMBER | |
| | | | | 5f. WORK UNIT NUMBER | |
| 7. PERFORMING ORGANIZATION NAME(S) AND ADDRESS(ES) The New York and Presbyterian Hospital 525 East 68 th Street W-104 New York, NY 10021 | | | | 8. PERFORMING ORGANIZATION REPORT NUMBER | |
| 9. SPONSORING / MONITORING AGENCY NAME(S) AND ADDRESS(ES) U.S. Army Medical Research and Materiel Command Fort Detrick, Maryland 21702-5012 | | | | 10. SPONSOR/MONITOR'S ACRONYM(S) USAMRMC | |
| | | | | 11. SPONSOR/MONITOR'S REPORT NUMBER(S) | |
| 12. DISTRIBUTION / AVAILABILITY STATEMENT Approved for Public Release; Distribution Unlimited | | | | | |
| 13. SUPPLEMENTARY NOTES | | | | | |
| 14. ABSTRACT The purpose of this study is to develop a dedicated image-guided external-beam radiotherapy system for accelerated partial breast irradiation (APBI). We have made significant progress in the past year for this grant focusing on building each sub-system of the proposed apparatus - Aim 1 for the x-ray generator, Aim 2 for the imaging sub system and Aim 3 for the treatment planning. For Aim 1 we are concentrating on analyzing the shielding cost and imaging quality for different energies using Monte Carlo simulations. These results are critical to our final decision on the x-ray source. The panoramic CBCT technology is the heart of the imaging sub system as it reduces the hardware and construction cost. To these ends, we have spent a significant amount of resources on image stitching algorithms and developed parallel processing schemes using GPU for speeding up CBCT reconstructions. Treatment planning is also critical to a successful radiotherapy system. Because the design of the proposed APBI machine is different from conventional linear accelerator, a new treatment planning system (TPS) is being built using the Clarkson and pencil beam convolution methods. An inverse planning algorithm has also been developed using a generic algorithm that takes advantages of the novel irradiation geometries of the proposed ABPI apparatus. | | | | | |
| 15. SUBJECT TERMS Panoramic CBCT, dedicated ABPI apparatus, treatment planning system. | | | | | |
| 16. SECURITY CLASSIFICATION OF: | | | 17. LIMITATION OF ABSTRACT UU | 18. NUMBER OF PAGES 103 | 19a. NAME OF RESPONSIBLE PERSON USAMRMC |
| a. REPORT U | b. ABSTRACT U | c. THIS PAGE U | | | 19b. TELEPHONE NUMBER (include area code) |



DOD Year 2 Report

July 18, 2011 to August 17, 2012

Radiation Oncology

Weill Cornell Medical College

**Dr. K.S. Clifford Chao, M.D. – Chairman Radiation
Oncology and P.I.**

Contents

| | |
|--|----|
| Introduction..... | 5 |
| Specific Aims..... | 5 |
| The Project Milestone Schedule..... | 7 |
| Year 2 Project Plan and Status..... | 10 |
| Year 2 Publications | 13 |
| Year 2 Results | 15 |
| Discussion of Year 2 Project Results | 31 |
| References..... | 32 |
| Appendix: Year 2 Publications | 33 |

Introduction

Although radiotherapy is an effective treatment for breast cancers, it also brings significant late morbidity. In order to reduce the treatment complications, Accelerated Partial Breast Irradiation (APBI) has been used to irradiate the post lumpectomy cavity instead of the whole breast for early stage breast cancer patients. However, conventional external beam radiotherapy is not optimal for APBI due to inadequate understanding of the exact location of the post lumpectomy cavity, insufficient setup/monitoring accuracy and limited beam selection. The goal of this study is to develop a dedicated image-guided treatment system for APBI. We will first determine the optimal techniques for localizing and tracking the post lumpectomy cavity. Historically, x-ray projection imaging, cone-beam CT and optical surface imaging have been used to image/track the surrogate for post lumpectomy cavity, including surgical clips, seroma, and shape of the breast to guide ABPI. However, each of these methods experiences some variation during the treatment period and the performance between surgery and simulation is not well understood. In this study the performance of these methods will be fully investigated and understood from surgery to the end of treatment. The optimal system for imaging/tracking the post lumpectomy cavity will then be used to guide a cost-effective, dedicated irradiator for ABPI. This unit will use a single x-ray source for imaging and therapy, and will have a compact, self-shielded housing to reduce the cost. The head of the irradiator will rotate around the breast being treated to increase the flexibility of beam selection and will be able to deliver intensity modulated beams to spare heart and lung. A treatment planning system will also be developed for real-time imaging/tracking and re-planning. Successful completion of the proposed breast irradiator will have a significant impact on ABPI as the setup accuracy, delivery efficiency and treatment outcome are expected to be comparable or even better than the current standard. The low-cost and compact design will also make ABPI more accessible to women in uniform and in developing or undeveloped countries.

Specific Aims

For early stage breast cancer patients, post lumpectomy Accelerated Partial Breast Irradiation (APBI) has been used as an alternative to whole breast irradiation. The objective of APBI is to deliver a highly conformal and lethal dose of radiation to the cancer cells within the target volume (TV, the area of the lumpectomy cavity) while avoiding morbidity in the surrounding healthy tissue. To accomplish this, APBI relies on the precise and accurate TV localization and dose delivery for each fraction of the treatment. However, current external beam APBI is delivered using a general-purpose x-ray irradiator (e.g., linear accelerator or cobalt unit), which is sizable, expensive, and most importantly, suboptimal as the beam selection is very restricted.

The goal of this study is to develop a dedicated image-guided external-beam radiotherapy system for APBI. The central hypothesis of this application is that a dedicated radiotherapy unit customized for prone breast setup/irradiation considering all the technical challenges is much more optimal and cost-effective for APBI than conventional general-purpose external beam unit. The rationale for this application is that, a more cost-effective and compact dedicated breast irradiator will make ABPI more accessible to women in uniform, in under-served population, and in developing countries, and will improve the control/cure rates with better cosmetic outcomes for breast cancer patients in those populations. We plan to test our central hypothesis and accomplish the objective of this application by pursuing the following three specific aims:

1. Design and prototype a dedicated radiation delivery apparatus for partial breast irradiation:
 - 1.1. Determine the optimal X-ray energy for imaging, therapy and shielding purposes.
 - 1.2. Optimize the space and shielding requirement by integrating real-time imaging and tracking systems and beam stopper into a small form factor.
 - 1.3. Construct a prone breast patient immobilization board to optimize patient comfort, setup accuracy, and reproducibility.
 - 1.4. Build a smart beam-shading device that can deliver pencil beam IMRT in non-isocentric and non-coplanar manner.
 - 1.5. Evaluate dosimetric accuracy and delivery efficiency in phantoms.
2. Develop an image-guidance system for patient setup and tracking:
 - 2.1. Determine the optimal configuration of imager and control circuit for the dedicated APBI unit in Aim 1.
 - 2.2. Develop efficient CBCT reconstruction algorithms for the source and imaging geometry.
 - 2.3. Construct hardware and software motions phantoms to simulation breathing motion during treatment.
 - 2.4. Build and test a real-time image-guided software module for patient setup and motion management.
3. Develop a real-time image-guided treatment planning system for the dedicated breast radiotherapy apparatus in Aim 1 and 2:
 - 3.1. Develop an inverse planning algorithm for the proprietary delivery mechanism.
 - 3.2. Explore an efficient scheme for real-time re-planning of the treatment based on the tumor location and deformation.

Successful completion of the proposed dedicated breast irradiator will have a significant impact on partial breast irradiation as the setup accuracy, delivery efficient and treatment outcome are expected to be comparable or even better than the current treatment approach using a standard linear accelerator. However, the small and compact design of the irradiation apparatus will allow breast radiotherapy to be performed in many clinics without large vault for modern external radiotherapy unit. The self-shielding design will also significantly reduce the shielding requirement. As a result, breast radiotherapy can be more available to people at the community hospital rather than at the regional cancer center that might be 40-50 miles (or even further) away. For military personnel, this means less time spent on travel to military hospitals or VA medical with radiotherapy facility, which is sparse around the country. The low cost and small size apparatus will also benefit many women with breast cancers in the developing or under-developed countries who usually don't have easy access to radiotherapy treatment for their diseases.

The Project Milestone Schedule

The project milestone schedule marks the project's major aim and subaims and establishes the planned timeline for their completion. A milestone schedule for the aims of this project is presented in Figure 1. The high-level tasks are also briefly described below.

1. Design and prototype a dedicated radiation delivery apparatus for partial breast irradiation:
 - 1.1. Determine the optimal X-ray energy for imaging, therapy and shielding purposes: We will use Monte Carlo code to calculate projection images for 300 kVp to 6 MV photons and studied the image qualities of reconstructed CBCT. We will also produce percent depth dose and beam profiles of different energies. A cost function will be developed considering image quality, beam penetration, normal tissue toxicity and construction cost as an objective metric for evaluating the merit of each beam.
 - 1.2. Optimize the space and shielding requirement by integrating real-time imaging and tracking systems and beam stopper into a small form factor: We will use Monte Carlo simulation and theoretical analysis to simulate the quality of different beam energies ranging from 300 kVp to 6 MV, and estimate the shielding requirements and cost. Lower energy-beam can be produced by directly lowering the accelerating potential in Monte Carlo simulation. The energy spectrum can be further manipulated (softened or hardened) using targets of various Z numbers in simulation. Once the leakage profile of the proposed unit is available from the Monte Carlo simulation, shielding requirements and cost can be calculated based on the available shielding data.
 - 1.3. Construct a prone breast patient immobilization board to optimize patient comfort, setup accuracy, and reproducibility: We plan to design and construct a prone breast board for the dedicated APBI apparatus. This prone breast board will address most deficiencies of current available prone boards and will work with the special geometry and beam shaping device to provide maximal comfort, stability and accuracy for APBI.
 - 1.4. Build a smart beam-shading device that can deliver pencil beam IMRT in non-isocentric and non-coplanar manner: At the end of the first year, we have designed a smart beam shaping device that can deliver pencil beam IMRT in non-isocentric and non-coplanar manner. We have also mathematically solved this aiming problem for this device in the grant proposal for the 2nd year. We plan to build a real-size prototype that will implement the aiming algorithm.
 - 1.5. Evaluate dosimetric accuracy and delivery efficiency in phantoms: As a baseline, the output of the flattened beams of the proposed radiotherapy system for APBI will first be calibrated according to the AAPM TG51 protocol¹. Since non-flattened and non-standard fields, shorter SSD and rotational radiation delivery will also be used for treatment, a calibration protocol will be developed for clinical use following the formalism developed by Alfonso et al². Calibrated ionization chambers, diode/TLD dosimeters and radiochromic films will be used to measure the dosimetric accuracy and delivery efficiency for test treatment plans on phantoms.
2. Develop an image-guidance system for patient setup and tracking:
 - 2.1. Determine the optimal configuration of imager and control circuit for the dedicated APBI unit in Aim 1: Because the space limitation, a small imager (< 20 cm in width and length) is expected to be used. The optimal imager configuration therefore depends on how accurate the imager can be calibrated for measuring the radiation fluence and how well images can be stitched together to form a larger projection image. We will first model the detector response, develop an EPID calibration and an image stitching algorithms. The optimal configuration will be determined based on the requirements of both algorithms.

- 2.2. Develop efficient CBCT reconstruction algorithms for the source and imaging geometry: We plan to develop a CBCT reconstruction technique that patches projection images from multiple scans to increase the reconstruction volume and minimizes artifacts. We will implement the Feldkamp algorithm³ or the simultaneous algebraic reconstruction technique (SART)⁴ for CBCT reconstruction. Graphic processing unit (GPU) will be used to speed up the reconstruction, particularly for SART.
- 2.3. Construct hardware and software motions phantoms to simulation breathing motion during treatment:
 - 2.3.1. Hardware motion phantom: We will build and design a breathing phantom of a female torso to support the development and evaluation of the proposed image-guidance system. The phantom will be designed to include the breast structures and significant anatomical boney structures and soft tissue to produce a realistic patient breathing motion. The phantom soft tissue will be made using elastomeric materials that will replicate the characteristics of the corresponding human tissues. The phantom will include a computer controlled respiratory system that will produce respiratory motion patterns driven by recorded patient respiratory data in addition to parameterized, regular breathing patterns. The phantom control application software will be written to run on a computer using the Microsoft Windows operating system.
 - 2.3.2. Software motion phantom: We plan to license the XCAT digital motion phantom for general simulation. We will also build at least two moving thorax phantom—one from the 4D CT scan of the hardware motion phantom and one from the 4D CT scan of a real patient. The moving phantom will have multiple CT volumes—one for each breathing phase. The CT volume of each breathing phase will be segmented and linked to the appropriate lookup table for NIST mass attenuation coefficients. Siddon's method⁵ will be used to calculate the X-ray transmission line integral through the attenuation phantom from the X-ray source to the detector.
- 2.4. Build and test a real-time image-guided software module for patient setup and motion management: We will first formulate the requirements of the real-time image-guided software module. Different components of this software module will be built and tested. An efficient image segmentation algorithm will be developed to identify the treatment volume and critical organs considering the temporal and spatial variation of the patient anatomy. The “real-time image-guided treatment planning system” in Aim 3.2 will be interfaced with this software module. This software module will be tested and refined using the image data from digital motion phantoms and hardware motion phantoms.
3. Develop a real-time image-guided treatment planning system for the dedicated breast radiotherapy apparatus in Aim 1 and 2:
 - 3.1. Develop an inverse planning algorithm for the proprietary delivery mechanism: We plan to build a simple treatment planning system (TPS) first using Clarkson algorithm for dose calculation and 3D mathematical functions to define patient body, treatment targets and organs at risk. This simple TPS provide a convenient tool for optimizing the proprietary delivery mechanism. 3D pencil beam convolution algorithm for CT-based dose computation will later be implemented to evaluate the proposed machine using realistic patient scans. Different inverse planning algorithms using DVH and NTCP will be tested in the simple TPS first for comparison. The identified optimal algorithm will then be implemented in the CT-based TPS.
 - 3.2. Explore an efficient scheme for real-time re-planning of the treatment based on the tumor location and deformation: We plan to test the proposed workflow for daily real-time re-planning using the simple TPS (Aim 3.1) and the hardware phantom (Aim 2.3).

| | 1 st Quarter 09/11-11/11 | 2 nd Quarter 12/12-02/12 | 3rd Quarter 03/12-05/12 | 4 th Quarter 06/12-08/12 |
|--|--|---|--|--|
| 1. Design and prototype a dedicated radiation delivery apparatus for partial breast irradiation: | | | | |
| 1.1. Determine the optimal X-ray energy for imaging, therapy and shielding purposes. | MC code evaluation, equipment acquisition | System configuration and install MC codes | Build imager geometry | Simulate images for different energies |
| 1.2. Optimize the space and shielding requirement by integrating real-time imaging and tracking systems and beam stopper into a small form factor. | Personnel recruitment and MC code evaluation | System configuration and install MC codes | Build machine/room geometry | 1 st round simulations and refining |
| 1.3. Construct a prone breast patient immobilization board to optimize patient comfort, setup accuracy, and reproducibility. | Clinical data analysis, CAD software selection and training | | Analyze the requirements and design using CAD software | |
| 1.4. Build a smart beam-shading device that can deliver pencil beam IMRT in non-isocentric and non-coplanar manner. | Construct “Curved-Surface Collimator” (CSC) assembly | | Build a functional model of the smart beam-shaping device | |
| 1.5. Evaluate dosimetric accuracy and delivery efficiency in phantoms. | No activity until the 4 th quarter of the 2 nd year. | | | Identify vendors for x-ray source |
| 2. Develop an image-guidance system for patient setup and tracking: | | | | |
| 2.1. Determine the optimal configuration of imager and control circuit for the dedicated APBI unit in Aim 1. | Mathematical modeling of detector responses. | | Develop (1) calibration method for array detector and (2) image stitching algorithms | |
| 2.2. Develop efficient CBCT reconstruction algorithms for the source and imaging geometry. | Develop panoramic CBCT technique using simulation data | | GPU parallel processing for forward projections | |
| 2.3. Construct hardware motion phantom (HMP) and software motion phantom (SMP) to simulation breathing motion during treatment. | Build & test in-house digital phantom. | | SMP: license and test XCAT, MCAT | |
| | | | HMP: develop requirements and look for vendors | |
| 2.4. Build and test a real-time image-guided software module for patient setup and motion management. | No activity until the 3 rd quarter of the 2 nd year. | | Formulate the requirements | |
| 3. Develop a real-time image-guided treatment planning system for the dedicated breast radiotherapy apparatus in Aim 1 and 2: | | | | |
| 3.1. Develop an inverse planning algorithm for the proprietary delivery mechanism. | No activity until the 3 rd quarter of the 2 nd year. | | Simple geometry TPS: forward and inverse planning | |
| 3.2. Explore an efficient scheme for real-time re-planning of the treatment based on the tumor location and deformation. | No activity until the 3 rd year. | | | |

Figure 1. Time project milestone schedule for the 2nd year.

Year 2 Project Plan and Status

The progress of the project is shown in Figure 2. As of the end of 2nd year, the overall project is on schedule – most sub aims are on or ahead of schedule and some are slightly behind the schedule. The following presents the personnel and resource allocations and progress of each sub aims for this quarter:

1. Design and prototype a dedicated radiation delivery apparatus for partial breast irradiation:
 - 1.1. Determine the optimal X-ray energy for imaging, therapy and shielding purposes:
 - Personnel: Dr. Song Wang supervised by Dr. Jenghwa Chang.
 - Resources: A DELL Precision T7500 Tower Workstation was purchased for this purpose. This workstation is reconfigured by installing Linux OS so that EGS/NRC Monte Carlo software can be installed and run on this workstation.
 - Progress: On schedule.
 - 1.2. Optimize the space and shielding requirement by integrating real-time imaging and tracking systems and beam stopper into a small form factor:
 - Personnel: Dr. Bertrand Biritz and Dr. Leo Li supervised by Mr. John Cheeseborough.
 - Resources: Fluka Monte Carlo software was installed on a Linux server with 16 cores.
 - Progress: On schedule.
 - 1.3. Construct a prone breast patient immobilization board to optimize patient comfort, setup accuracy, and reproducibility:
 - Personnel: Dr. Fridon Kulidzhanov and Dr. Leo Li are responsible for this project.
 - Resources: A copy of Turbo CAD software was purchased for designing the prone breast board.
 - Progress: On schedule.
 - 1.4. Build a smart beam-shading device that can deliver pencil beam IMRT in non-isocentric and non-coplanar manner:
 - Personnel: Mr. John Cheesborough is responsible for this project.
 - Resources: A copy of Dessault Systems SolidWorks was purchased for the design of the device. Rapid prototyping equipment was used to construct a functional model.
 - Progress: On schedule.
 - 1.5. Evaluate dosimetric accuracy and delivery efficiency in phantoms:
 - Dr. Clifford Chao is responsible for this project by contacting different for potential x-ray sources.
 - Progress: On schedule.
2. Develop an image-guidance system for patient setup and tracking
 - 2.1. Determine the optimal configuration of imager and control circuit for the dedicated APBI unit in Aim 1:
 - Personnel: Dr. Song Wang and Dr. Leo Li supervised by Dr. Jenghwa Chang are responsible for developing the calibration algorithm. Dr. Xing Wang was hired in the fourth quarter and supervised by Dr. Jenghwa Chang for developing the image stitching algorithm.
 - Resources: the EPID on the Varian iX LINAC and the MapCheck device for IMRT QA.
 - Progress: Mathematical modeling of detector response and development of the calibration algorithm is on schedule. Development of the image stitching algorithm is delayed by ~2 months due to slow recruiting.

2.2. Develop efficient CBCT reconstruction algorithms for the source and imaging geometry:

- Personnel: Dr. Lili Zhou supervised by Dr. Jenghwa Chang.
- Resources: A DELL 7400 workstation and two NVIDIA Tesla C2050 GPGPU cards was purchased for parallel processing of the reconstruction algorithms. 4D MCAT (Mathematical Cardiac Torso phantom) and XCAT (extended cardiac-torso) digital motion phantoms were used to generated simulated projection images. Projection images of the CT CatPhan phantom for CBCT reconstruction were also generated using the EPID no the Varian iX LINAC.
- Progress: On schedule.

2.3. Construct hardware and software motions phantoms to simulation breathing motion during treatment:

- Personnel: Dr. Lili Zhou supervised by Dr. Jenghwa Chang is responsible for the software motion phantom. Dr. Xin Wang was hired and supervised by Dr. Jenghwa Chang is responsible for developing the hardware motion phantom.
- Resources: 4D MCAT (Mathematical Cardiac Torso phantom) and XCAT (extended cardiac-torso) digital motion phantom software were purchased for generating projection images. We have also contacted potential vendors who might be able to customize their physical motion phantoms to serve our needs.
- Progress: Development of the software phantom is on schedule. Development of the hardware phantom is behind schedule by ~1 months due to slow recruiting.

2.4. Build and test a real-time image-guided software module for patient setup and motion management:

- Personnel: Mr. Hansen Chen is responsible for this project.
- Resources: VTK, ITK, DCMTK toolkits.
- Progress: on schedule.

3. Develop a real-time image-guided treatment planning system for the dedicated breast radiotherapy apparatus in Aim 1 and 2:

3.1. Develop an inverse planning algorithm for the proprietary delivery mechanism:

- Personnel: Drs. Song Wang and Daniel Li supervised by Dr. Jenghwa Chang.
- Resources: Drs. Wang and Li are currently using their personal notebook computers. Two DELL Precision workstations are recently ordered to speed up this project.
- Progress: on schedule.

3.2. Explore an efficient scheme for real-time re-planning of the treatment based on the tumor location and deformation:

- Personnel: Mr. Hansen Chen is responsible for this project.
- Resources: Not applicable
- Progress: on schedule.

Note: No activity until the 3rd year after the simple TPS in Aim 3.1 is completed.

| | 1 st Quarter 09/11-11/11 | 2 nd Quarter 12/12-02/12 | 3rd Quarter 03/12-05/12 | 4 th Quarter 06/12-08/12 |
|--|--|---|--|--|
| 1. Design and prototype a dedicated radiation delivery apparatus for partial breast irradiation: | | | | |
| 1.1. Determine the optimal X-ray energy for imaging, therapy and shielding purposes. | MC code evaluation, equipment acquisition | System configuration and install MC codes | Build imager geometry | Simulate images for the first energy |
| 1.2. Optimize the space and shielding requirement by integrating real-time imaging and tracking systems and beam stopper into a small form factor. | Personnel recruitment and MC code evaluation | System configuration and install MC codes | Build machine/room geometry | 1 st round simulations and refining |
| 1.3. Construct a prone breast patient immobilization board to optimize patient comfort, setup accuracy, and reproducibility. | Clinical data analysis, CAD software selection and training | | Analyze the requirements and design using CAD software | |
| 1.4. Build a smart beam-shading device that can deliver pencil beam IMRT in non-isocentric and non-coplanar manner. | Construct “Curved-Surface Collimator” (CSC) assembly | | Build a functional model of the smart beam-shaping device | |
| 1.5. Evaluate dosimetric accuracy and delivery efficiency in phantoms. | No activity until the 4 th quarter of the 2 nd year. | | | Identify vendors for x-ray source |
| 2. Develop an image-guidance system for patient setup and tracking: | | | | |
| 2.1. Determine the optimal configuration of imager and control circuit for the dedicated APBI unit in Aim 1. | Mathematical modeling of detector responses. | | Develop calibration method for array detector and image stitching algorithms | |
| 2.2. Develop efficient CBCT reconstruction algorithms for the source and imaging geometry. | Develop panoramic CBCT technique using simulation data | | GPU parallel processing for forward projections | |
| 2.3. Construct hardware motion phantom (HMP) and software motion phantom (SMP) to simulation breathing motion during treatment. | Build & test in-house digital phantom. | | SMP: license and test XCAT, MCAT | |
| | | | HMP: develop requirements and look for vendors | |
| 2.4. Build and test a real-time image-guided software module for patient setup and motion management. | No activity until the 3 rd quarter of the 2 nd year. | | Formulate the requirements | |
| 3. Develop a real-time image-guided treatment planning system for the dedicated breast radiotherapy apparatus in Aim 1 and 2: | | | | |
| 3.1. Develop an inverse planning algorithm for the proprietary delivery mechanism. | No activity until the 3 rd quarter of the 2 nd year. | | Simple geometry TPS: forward and inverse planning | |
| 3.2. Explore an efficient scheme for real-time re-planning of the treatment based on the tumor location and deformation. | No activity until the 3 rd year. | | | |

Figure 2. Progress of the project. The blue arrow indicates the progress of each task.

Year 2 Publications

In this section we list the peer-reviewed papers, abstracts and presentations that were published during the 2nd year:

Peer-reviewed papers:

1. J. Chang, L. Zhou, S. Wang, KSC. Chao, "Panoramic cone beam computed tomography," *Medical Physics* 2012;39:2930-2946.
2. L. Zhou, K. S. C. Chao, and J. Chang, "Fast Poly-energetic Forward Projection for Image Formation Using OpenCL on a Heterogeneous Parallel Computing Platform," submitted to the *Medical Physics*.

Abstracts:

1. R. Bassalow, A. Sabbas, M. Delamerced, S. Trichter, F. Kulidzhanov, L. Nedialkova, D. Nori, K. Chao, and J. Chang, "SU-E-T-337: Monte-Carlo Study of Dose Perturbation Effects in External Beam Therapy of the Prostate Caused by the Presence of Post-Implant Brachytherapy Seeds," *Proc. AAPM 2010 Annual Meeting, Medical Physics* **38**, 3565-3565 (2011).
2. R. Bassalow, S. Trichter, A. Sabbas, B. Parashar, F. Kulidzhanov, L. Nedialkova, G. Wernicke, D. Nori, K. Chao, and J. Chang, "SU-E-T-582: Monte-Carlo Study of Dosimetric Effects of Brachytherapy Seeds Presence in Lung External Beam SBRT," *Proc. AAPM 2011 Annual Meeting, Medical Physics* **38**, 3623-3623 (2011).
3. J. Chang, L. Zhou, and K. Chao, "SU-E-J-10: Panoramic Cone Beam Computed Tomography (CBCT)," *Proc. AAPM 2011 Annual Meeting, Medical Physics* **38**, 3443-3443 (2011).
4. F. Kulidzhanov, A. Sabbas, J. Chang, S. Trichter, M. Hayes, G. Wernicke, D. Nori, and K. Chao, "SU-E-T-497: Experience in Prone Breast Setup Accuracy Improvement," *Proc. AAPM 2011 Annual Meeting, Medical Physics* **38**, 3603-3603 (2011).
5. A. Sabbas, F. Kulidzhanov, S. Trichter, R. Bassalow, B. Biritz, B. Parashar, D. Nori, K. S. Chao, and J. Chang, "SU-E-T-574: Assessment of Target Motion in SBRT Lung Patients Using the Frame-Based Stereotactic Coordinates," *Proc. AAPM 2011 Annual Meeting, Medical Physics* **38**, 3621-3621 (2011).
6. S. Trichter, S. Chiu-Tsao, M. Zaider, A. Sabbas, F. Kulidzhanov, J. Chang, G. Cohen, D. Nori, and K. Chao, "WE-A-BRB-01: Accurate Dosimetric Characterization of a Fully Loaded 20 Mm COMS I-125 Eye Plaque Using Specially Designed GAFCHROMICTM Film," *Proc. AAPM 2011 Annual Meeting, Medical Physics* **38**, 3791-3791 (2011).
7. L. Zhou and J. Chang, "SU-E-J-23: Construction of Digital Phantoms for X-Ray Image-Guided Radiotherapy (IGRT)," *Proc. AAPM 2011 Annual Meeting, Medical Physics* **38**, 3446-3447 (2011).
8. L. Nedialkova, M. Delamerced, A. Sabbas, J. Chang, and C. Chao, "Non-Vertical Co-Planar Beam Arrangement Can Improve Dose to Organs at Risk (OARs)," *International journal of radiation oncology, biology, physics* **81**, S907 (2011).
9. L. Zhou, Y. Chi, K. S. C. Chao, and J. Chang, "Feasibility Study of Panoramic Cone Beam Computed Tomography (CBCT)," *International journal of radiation oncology, biology, physics* **81**, S825 (2011).
10. P. Yan, L. Zhou, Z. Li, Y. Chi, J. Chang, and C. Chao, "SU-C-BRA-01: 4D Cone-Beam CT Acquisition Using Respiratory Phase Predication Technique," *Proc. AAPM 2012 Annual Meeting, Medical Physics* **39**, 3602-3602 (2012).
11. L. Zhou and J. Chang, "TH-C-BRA-03: Fast Iterative Cone Beam CT Reconstruction on GPGPU Using OpenCL," *Proc. AAPM 2012 Annual Meeting, Medical Physics* **39**, 4000-4000 (2012).

Presentations (oral or poster):

1. B. Biritz, "Treatment Planning for 106Ru Eye Plaques" 2012 Sal Vacirca Young Investigators Symposium of Radiological and Medical Physics Society of New York (RAMPS), Tuesday, March 27, 2012, New York, New York.
2. L. Zhou, "Fast Iterative Cone Beam CT Reconstruction on GPGPU using OpenCL," 2012 Sal Vacirca Young Investigators Symposium of Radiological and Medical Physics Society of New York (RAMPS), Tuesday, March 27, 2012, New York, New York.
3. Ping Yan, Ph.D.-Columbia, "Ultrasound-based Diaphragm Tracking Mitigates Respiratory Phase Variance by External Surrogate-based Respiratory Gating System," 2012 Sal Vacirca Young Investigators Symposium of Radiological and Medical Physics Society of New York (RAMPS), Tuesday, March 27, 2012, New York, New York.
4. H. Nagar, L.i Zhou, B. Biritz, J. Chang, C. Sison, M. Smith, D. Nori, K.S. C. Chau, M.K. Hayes "Is There a Tradeoff in Using Modified High Tangent Field Radiation for Treating an Undissected Node Positive Axilla?" NewYork Hospital Queens Residents and Fellows Research Day, May 16. 2012, Queens, New York.

Year 2 Results

1. Design and prototype a dedicated radiation delivery apparatus for partial breast irradiation:

1.1. Determine the optimal X-ray energy for imaging, therapy and shielding purposes.

Figure 3 shows the preliminary Monte Carlo simulations performed with the “egs_cbct” code⁶⁻⁷ to analyze the image quality as a function of field size for an on-board imaging panel of 40 kV point (or equivalently 120 kV x-ray) source. The irradiated phantom was a $60 \times 60 \times 30 \text{ cm}^3$ water phantom with one embedded bone insert of 20 cm length and $2 \times 2 \text{ cm}^2$ cross section. The source was placed 100 cm upstream of the iso-center and the water phantom centered at the iso-center. The imaging panel was positioned 50 cm downstream of the iso-center and comprised of 200×200 pixels with 0.2 cm pixel pitch. Simulations were conducted for field sizes ranging from 5×20 to $45 \times 20 \text{ cm}^2$ defined at the iso-centric plane (or 7.5×30 to $67.5 \times 30 \text{ cm}^2$ at the imaging plane) while the source fluence was kept constant for all simulations. Air kerma was scored as the detector response.

Since the same number of photons was used in the Monte Carlo simulation for each field size, results in Figure 3 indicate that for the same mAs, the image quality is better for the smaller field size. Better image quality for projection images also leads to better image quality for CBCT reconstruction. We plan to repeat the simulation and study the image quality for energies ranging from 120 kVp - 6MV during the 3rd year. We will also use the MC simulation to produce the percent depth dose for those energies. The combination of both studies will provide critical information for deciding the optimal energy for the proposed dedicated radiation delivery apparatus.

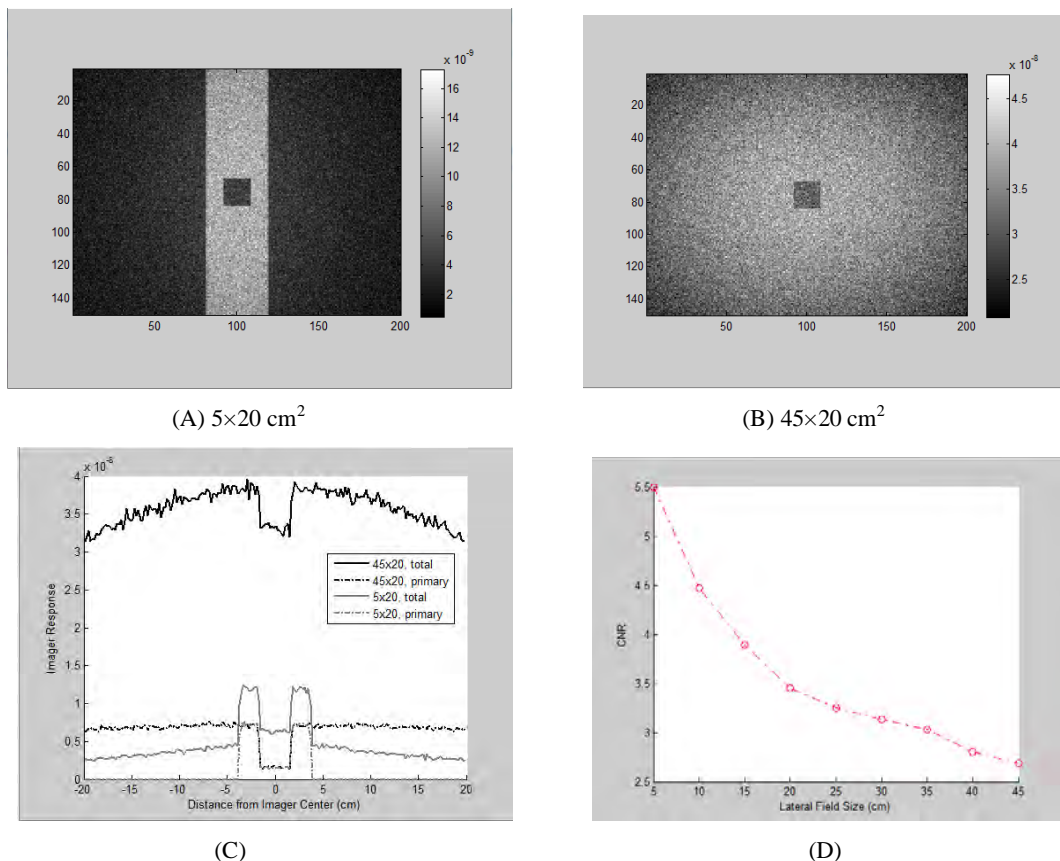


Figure 3: Simulated projection images for (A) $5 \times 20 \text{ cm}^2$ and (B) $45 \times 20 \text{ cm}^2$ fields respectively. Panel (C) shows the central profiles of the total signal and primary signal of both fields and Panel (D) is the contrast-to-noise ratio vs. the field size.

1.2. Optimize the space and shielding requirement by integrating real-time imaging and tracking systems and beam stopper into a small form factor.

FLUKA is a fully integrated particle physics Monte Carlo simulation package running on Linux. It is a mature and robust package developed at European Organization for Nuclear Research (CERN), an international high energy particle physics lab in Geneva Switzerland. To run this software efficiently, we built a parallel processing environment which included 4 Dell *PowerEdge* rack mounted servers, each with an Intel Xeon Quad Core CPU with TurboBoost technology running Fedora Linux.

Figure 4 show the preliminary Monte Carlo simulation results of the shielding requirements for 2 MV source and the current machine design, i.e., multiple-cone geometry. The geometry is: 10×10 cm field size, SAD of 58 cm, 130 cm from target to beam stopper (dimensions 50×35×20 cm, W×H×D), and 2 in. thick lead walls. As can be seen the beam stopper and lead walls already shield most of the primary and secondary radiation.

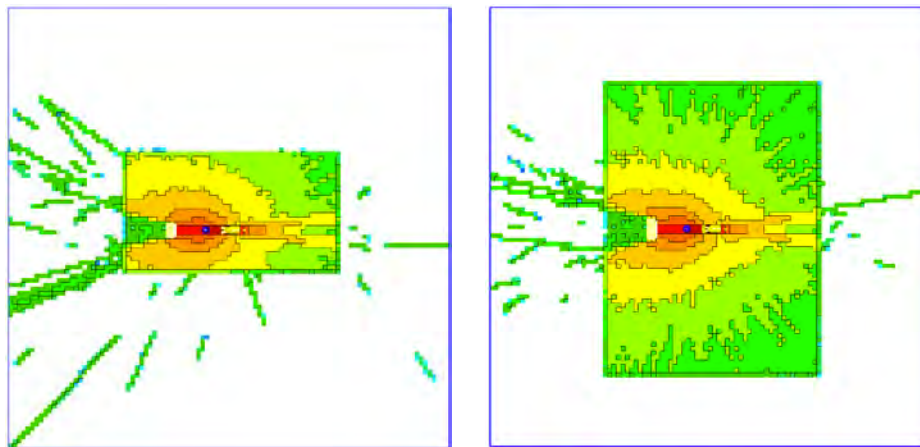


Figure 4. Monte Carlo simulation of the shielding requirements for 2 MV source.

The maximum value impinging on the wall to which the beam is 5.72 R/week. Using the NCRP 151 guideline of dose equivalent calculation for beams with energy less than 10 MeV, the dose equivalent is $5.72/104 = 0.055$ Sv/week = 55 mSv/week. Note that the above simulation is for one static beam. Since the proposed ABPI machine irradiates the patients from multiple angles, we can use similar parameters for CyberKnife shielding design. Assuming the use factor = 0.05, the dose equivalent is $55 \times 0.05 = 2.75$ mSv/week. To reduce the dose equivalent to 0.1 mSv/week, the required attenuation

is $\log\left(\frac{2.75}{0.1}\right) = 1.4$ TVL. Assuming the scattering energy is 500k, the attenuation can be achieved with $11.9 \times 1.4 = 16$ mm lead or $11.7 \times 1.4 = 16.4$ cm concrete.

We plan to continue the above simulation for different energies. Similar minimum requirements for shielding will be calculated and the design for proposed APBI machine will be modified accordingly.

1.3. Construct a prone breast patient immobilization board to optimize patient comfort, setup accuracy, and reproducibility.

We analyzed the clinical data and developed requirements for the proposed breast patient immobilization board. We also had a draft for the first round of design and are currently putting the design in the TurboCad software. We will have by the end of the 1st quarter of the 3rd year a complete design in CAD format that can be forwarded to the machine shop for construction.

1.4. Build a smart beam-shading device that can deliver pencil beam IMRT in non-isocentric and non-coplanar manner.

We have completed the construction of the mechanical components of a functional model of the smart beam-shaping device. The assembly consists of the “Curved-Surface Collimator” (CSC) assembly mounted on a two-axis gimbals assembly. Figure 5 shows the CSC and two-axis gimbals as a combined servo-mechanical assembly. It describes the designation of each axis of motion. The CSC is the smart beam-shaping device while the gimbals add the capability for non-isocentric, non-coplanar treatment.

We have selected a Gallil, DMC-4183 motion controller for the servo-mechanical assembly. This controller has been used successfully in other radiation therapy systems and we are confident that it will be a good fit for this application. We have begun the development of the diagnostic level functions of the application software to control the model.

Collimation Device – Axis Definitions for Motion Control System

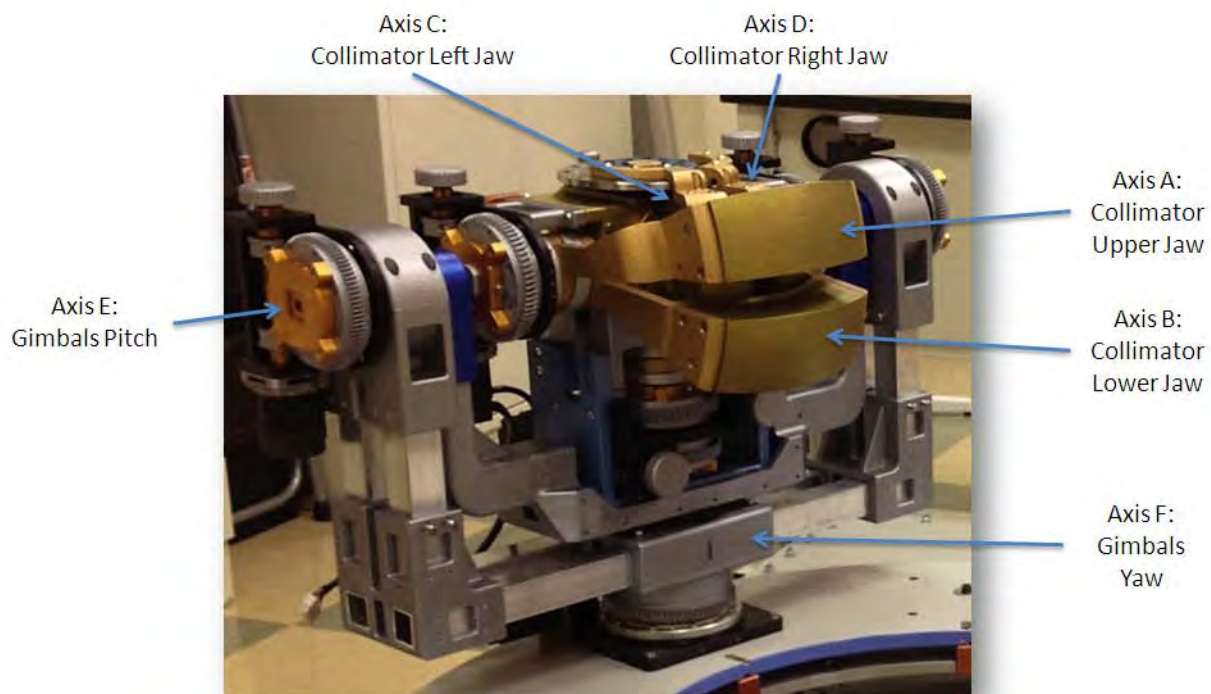
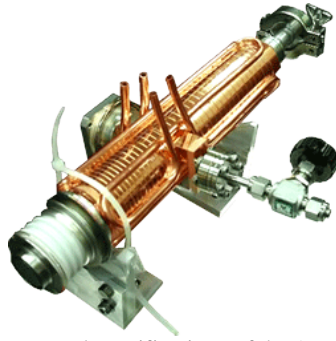


Figure 5: Photo of the smart beam-shaping device prototype.

We will develop the user interface for diagnostic control starting the 1st quarter of the 3rd year. When this is complete, we will begin the integration of the hardware and software, to be followed by the continued development of the operation of the smart beam-shaping device as a servo-mechanical assembly.

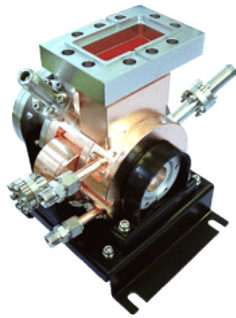
1.5. Evaluate dosimetric accuracy and delivery efficiency in phantoms.

We are currently investigating a few x-ray sources from different vendors. The most attractive products are manufactured by AET, Inc (<http://www.aetjapan.com>). The Compact Linear Accelerator developed by AET has maximum beam energy of 50MeV and accelerator length of 70cm or less, and is capable of high electric field acceleration. Figure 6 shows the pictures and specifications of the 1MeV X-Band Compact Linear Accelerator and 2 MeV S-Band Compact Linear Accelerator by AET, Inc., that we are seriously consider for this project.



| | |
|-------------------------------|-------------------------------|
| Structure | On-axis coupled standing wave |
| Accelerator Material | OFHC |
| Accelerator Length | 25cm |
| Acceleration Frequency | 9,400MHz |
| Qo Value | 8,500 |
| Shunt Impedance | 70MΩ/m |
| Beam Energy | 1MeV @250KW |
| Beam Current | 150mA |

Figure 6A. Picture and specifications of the 1MeV X-Band Compact Linear Accelerator by AET, Inc.



| | |
|-------------------------------|----------------------------|
| Structure | Side coupled standing wave |
| Accelerator Material | OFHC |
| Accelerator Length | 15cm |
| Acceleration Frequency | 2,856MHz |
| Qo Value | 14,500 |
| Shunt Impedance | 90MΩ/m |
| Beam Energy | 2MeV @2MW |
| Beam Current | 500mA |

Figure 6B. Picture and specifications of the 2 MeV S-Band Compact Linear Accelerator by AET, Inc.

2. Develop an image-guidance system for patient setup and tracking:

2.1. Determine the optimal configuration of imager and control circuit for the dedicated APBI unit in Aim

Two-dimensional (2D) detector arrays, such as electronic portal image device (EPID) and “MapCheck”, are routinely used for dosimetric quality assurance (QA) of radiation treatment plans. Calibration of an array of 2D detectors is not trivial because it is impractical to irradiate one detector at a time. Instead, an open-field beam can be used to irradiate the whole or a part of the 2D array so that the sensitivity of each detector can be derived from the raw detector readings and the fluence of the irradiated field; the latter is actually not uniform and usually need to be determined or modified as well. Several methods have been developed in the past for calibration of the 2D detector array and most of them are very time consuming.

We have developed an efficient method to determine the sensitivities of a 2D detector array for the APBI machine. This method only requires the irradiation of the 2D array with a wide open-field beam at the central and two (one laterally and one longitudinally) shifted locations. The irradiations at the central and lateral locations are required to reconstruct the relative lateral beam profiles, as shown in Figure 7A, and the irradiations at the central and longitudinal locations are used to reconstruct the relative longitudinal beam profiles,.

For a specific longitudinal location Y' ,

$$\frac{M_C(X, Y')}{M_{LAT}(X, Y')} = \frac{R(X, Y') \times S(X, Y')}{R(X-1, Y') \times S(X, Y')} = \frac{R(X, Y')}{R(X-1, Y')} \quad (1)$$

Rewriting this formula gives

$$R(X, Y') = R(X-1, Y') \times \frac{M_C(X, Y')}{M_{LAT}(X, Y')} = R(X-2, Y') \times \frac{M_C(X-1, Y')}{M_{LAT}(X-1, Y')} \times \frac{M_C(X, Y')}{M_{LAT}(X, Y')}$$

$$= R(X - M, Y') \times \frac{M_C(X - M + 1, Y')}{M_{LAT}(X - M + 1, Y')} \times \frac{M_C(X - M + 2, Y')}{M_{LAT}(X - M + 2, Y')} \times \dots \times \frac{M_C(X, Y')}{M_{LAT}(X, Y')} \quad (2)$$

From the above formula, the relative beam profile at any lateral position M on the positive X axis and longitudinal position Y' can be derived from the ratio of two measurements, iteratively from 1 to M . Similarly, relative 1D longitudinal beam profiles at lateral position X' and longitudinal position N can be derived.

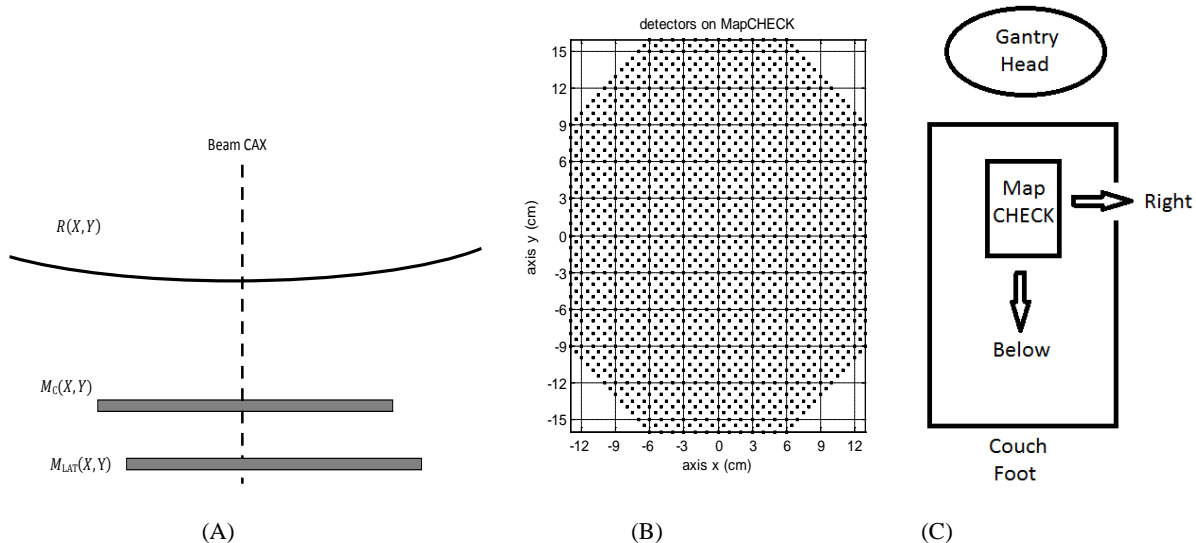


Figure 7. (A) Measurements required to calculate relative lateral beam profiles. $M_C(X,Y)$ is a wide-beam irradiation at the central detector array with respect to the central axis (CAX), $M_{LAT}(X,Y)$ is a wide-beam irradiation with the array shifted laterally and $R(X,Y)$ is the two-dimensional beam profile in question. (B) The dimension of the MapCHECK device and the detectors (plotted as dots) (C) The orientation of the setup.

We have tested this algorithm using the MapCHECK device (Figure 7B) as its calibration is simpler and already available. MapCHECK has its own calibration routine, and the sensitivity of all detectors can be read readily, which was used as the “gold standard” for comparison in this study. The orientation of the setup is shown in Figure 7C. We also developed a “shift with error-locking” method to minimize the error propagation and implemented the method developed by Greer et al⁸ for comparison. Figure 8 shows the central beam profiles measured by the vendor routine, the “shift with error-locking” method and the Greer’s method. Figure 8A is the beam profiles along X axis and Figure 8B is along Y axis. It is observed that these three methods agree with each other quite well in the central area but diverge at the beam borders. This is expected since beam penumbra is not considered in our model.

In conclusion, we have developed a sensitivity calibration method for calibrating array detector. This method requires only two shifts of detector for data collection (large field irradiation), from which the sensitivity of the detector can be reconstructed recursively. Additional 3-4 small field irradiations are needed with the “shift with error-locking” method, which can significantly reduce the error propagation. The results showed that our “shift with error-locking” method is comparable with the Greer method but requires much fewer measurements. In addition, this method requires no complicated modeling (using Monte Carlo simulations), does not use beam flattening. Moreover, no rotation of the detector is needed for our method, which is particularly suitable for 2D arrays with no rotation function like EPID and

MapCheck. We are currently improving the model of the detector array to address this problem at the penumbra regions.

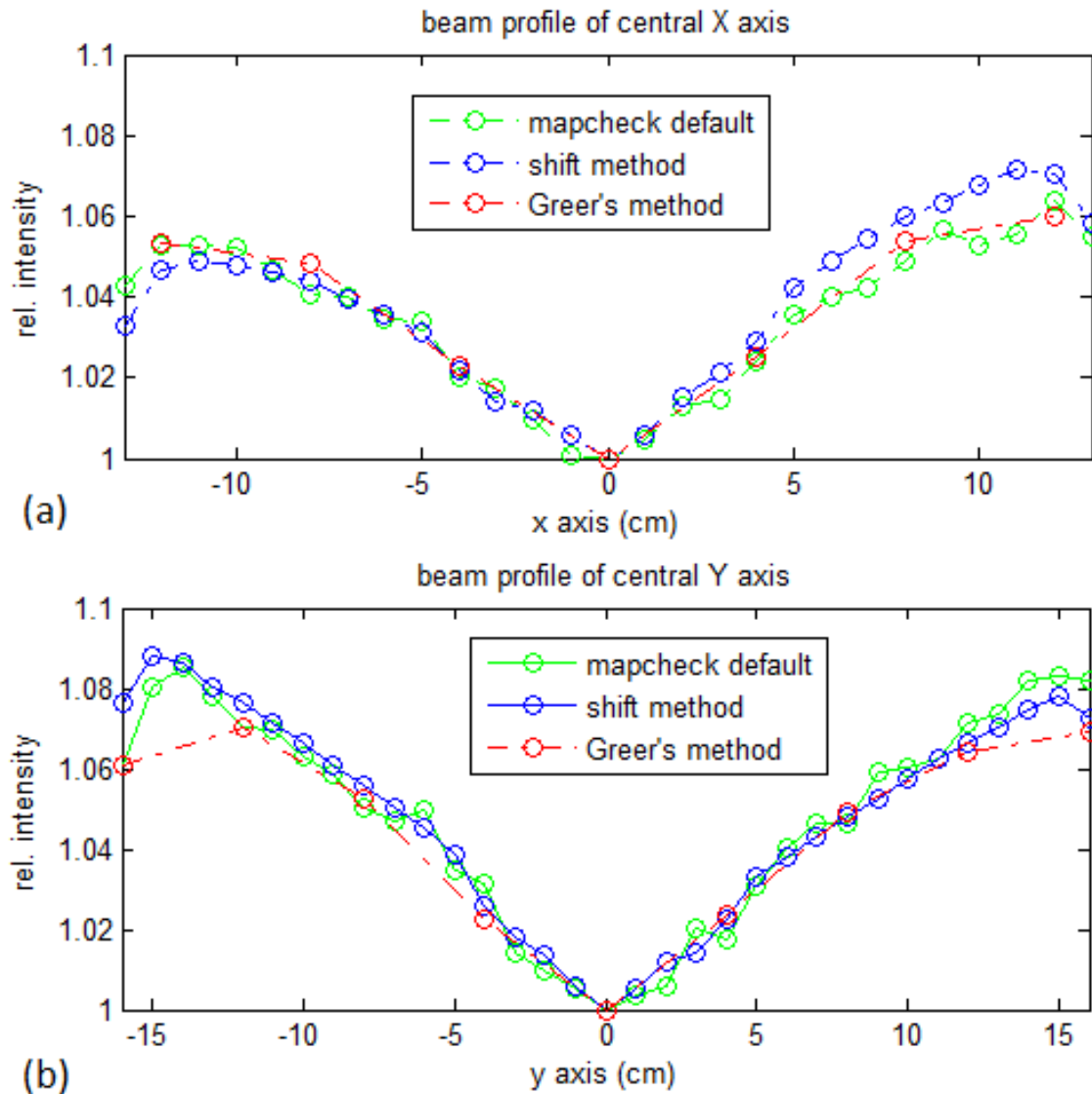


Fig. 8 Central beam profiles by the vendor routine inside MapCHECK, by the “shift with error-locking” method and the Greer’s method are compared. (a) are beam profiles along X axis. (b) are beam profiles along Y axis.

2.2. Develop efficient CBCT reconstruction algorithms for the source and imaging geometry.

2.2.A. Panoramic CBCT

Cone-beam computed tomography (CBCT) is the main imaging tool for image-guided radiotherapy but its functionality is limited by a small imaging volume and restricted image position (imaged at the central instead of the treatment position for peripheral lesions to avoid collisions). Here, we present the concept of “panoramic CBCT” which can image patients at the treatment position with an imaging volume as large as practically needed.

As shown in Figure 9, in this novel “panoramic CBCT” technique, the target is scanned sequentially from multiple view angles. For each view angle, a half scan ($180^\circ + \theta_{\text{cone}}$ where θ_{cone} is the cone angle) is performed with the imaging panel positioned in any location along the beam path. The panoramic projection images of all views for the same gantry angle are then stitched together with the direct image stitching method (i.e., according to the reported imaging position) and full-fan, half-scan CBCT reconstruction is performed using the stitched projection images.

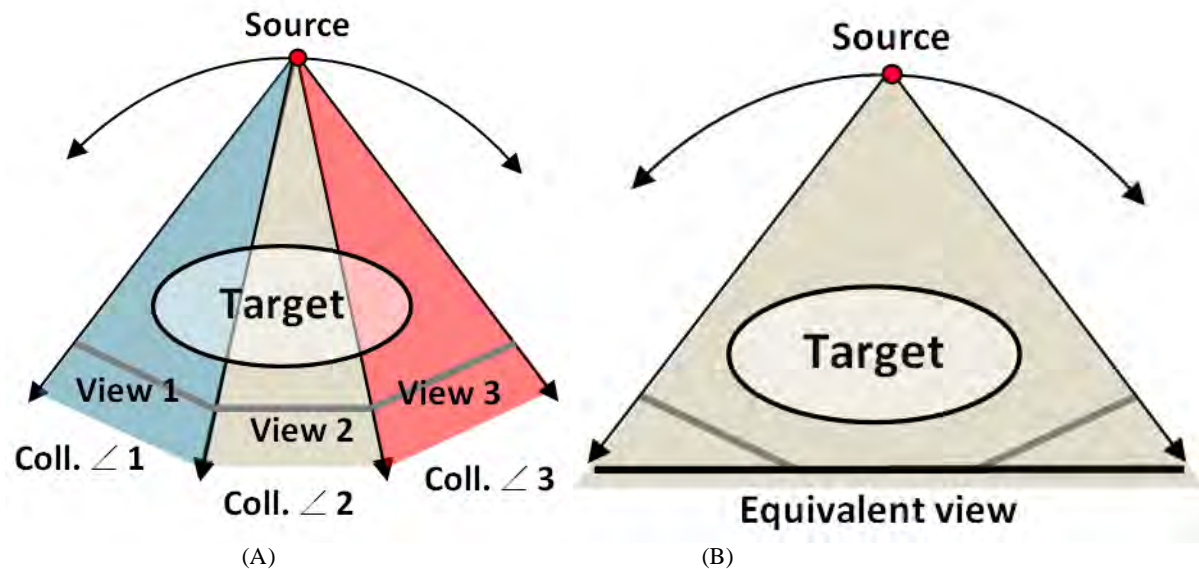


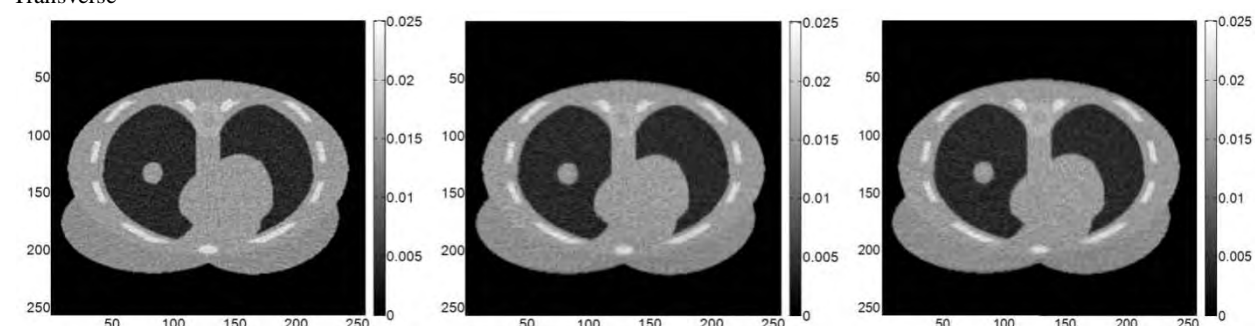
Figure 9. Illustration of the concept of panoramic CBCT. (A) Three panoramic views achieved by sequentially collimating the source (Coll. ∠ 1, Coll. ∠ 2 or Coll. ∠ 3) to irradiate a part of the target for half scan. The field size is comparable to the size of the imaging panel positioned along the beam path for each view. (B) The “equivalent” view from the three panoramic views re-binned at a plane normal to the central axis of the source, which is equivalent to scan the target using an “equivalent” imaging panel large enough to encompass the whole target.

To validate this imaging technique, we simulated cone-beam projection images of the Mathematical Cardiac Torso (*MCAT thorax phantom*) for three panoramic views. Gaps, repeated/missing columns and different exposure levels were introduced between adjacent views to simulate imperfect image stitching due to uncertainties in imaging position or output fluctuation. A modified simultaneous algebraic reconstruction technique (modified SART) was developed to reconstruct CBCT images directly from the stitched projection images. As a gold standard, full-fan, full-scan (360° gantry rotation) CBCT reconstructions were also performed using projection images of one imaging panel large enough to encompass the target. Contrast-to-noise ratio (CNR) and geometric distortion were evaluated to quantify the quality of reconstructed images.

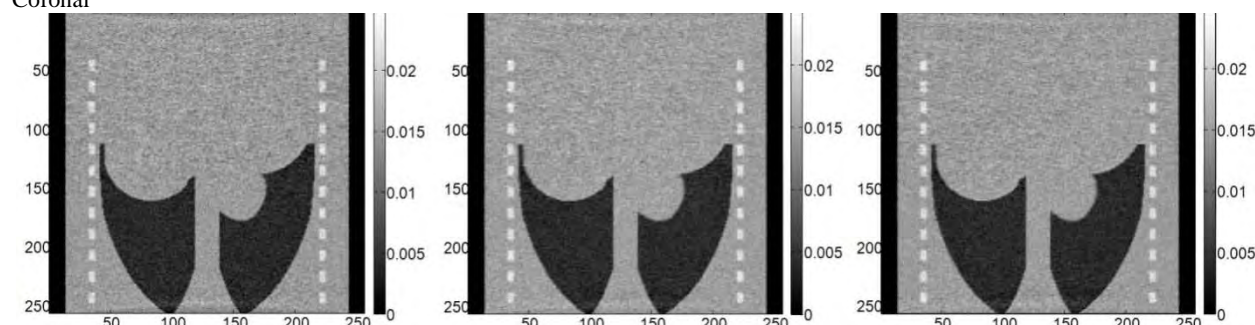
The results show that truncated images with artifacts were observed for the CBCT reconstruction using projection images of the central view only. As shown in Figure 10, when the image stitching was perfect, complete reconstruction was obtained for the panoramic CBCT using the modified SART with the image quality similar to the gold standard (full-scan, full-fan CBCT using one large imaging panel). Imperfect image stitching, on the other hand, lead to (streak, line or ring) reconstruction artifacts, reduced CNR and/or distorted geometry.

In conclusion, we have developed a panoramic CBCT technique and demonstrated with simulation data that it can image tumors of any location for patients of any size at the treatment position with comparable or less imaging dose and time. However, the image quality of this CBCT technique is sensitive to the reconstruction artifacts caused by imperfect image stitching. Better algorithms are therefore needed to improve the accuracy of image stitching for panoramic CBCT.

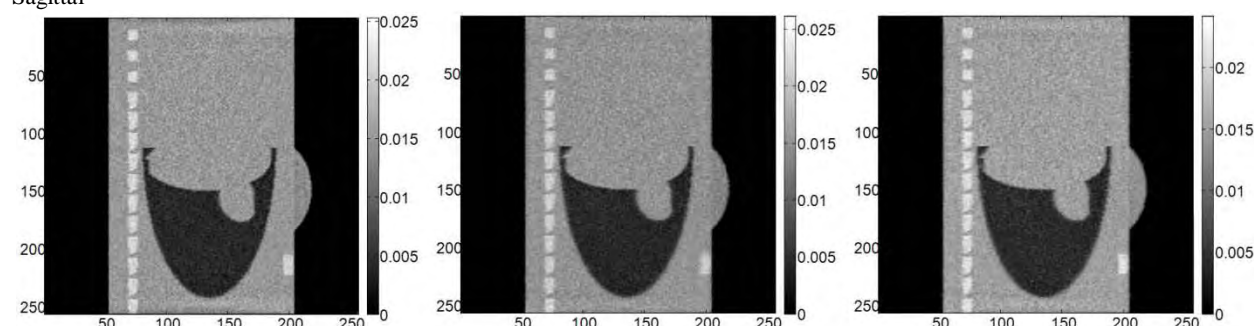
Transverse



Coronal



Sagittal



(A) 1 big panel/full scan

(B) 1 big panel/half scan

(C) 3 panoramic views/half scan

Figure 10. Comparison of transverse, coronal and sagittal slices for CBCT reconstructions using projection images from (A) 1 big panel/full scan (the standard for comparison), (B) 1 big panel/half scan, and (C) 3 panoramic views/half-scan. Standard SART was used for CBCT reconstructions of (A) and (B) while “modified SART” was used for (C). Full scan: 360° gantry rotation. Half scan: 200° gantry rotation.

2.2.B. Fast Forward Projection for Image Formation Using OpenCL

We are also investigating the use of parallel processing to speed up the CBCT reconstruction. The first step is to accelerate forward and backward projections on GPGPU Using OpenCL. Simulated projection images of digital phantoms constructed from CT scans have been widely used for clinical and research applications but their computation speed are not fast enough for real-time comparison with the radiography. To address this obstacle, we performed poly-energetic forward projections (see 2.3.A *Software Phantom* for more details) using Open Computing Language (OpenCL) in a parallel computing ecosystem consisting of CPU and GPGPU (general purpose graphics processing unit) for fast image formation.

Figure 11A illustrates the ray trace method for calculating the line integral along different rays for a two-dimensional object. The solid dots indicate the boundaries of intersecting pixels and the interval between two neighboring dots defines the chord length of intersection. The numbers of intersecting pixels along ray 1 and ray 2 are different. The Siddon's method⁵ is used to compute the x-ray transmission line integral and the x-ray fluence is the exponential of line with added Poisson noise. To accelerate the calculation we partitioned the workloads using the task parallelism (TP) and data parallelism (DP) and scheduled them in a parallel computing ecosystem consisting of CPU and GPGPU (NVIDIA Tesla C2050) using OpenCL *only*. Figure 11B illustrates the GPU architecture used to parallel-process the forward and backward projections in Figure 11A. We explored the task overlapping strategy and the sequential method for generating the first and subsequent DRRs. A dispatcher was designed to drive the high-degree parallelism of the task overlapping strategy. Numerical experiments were conducted to compare the performance of the OpenCL/GPGPU-based implementation with the CPU-based implementation.

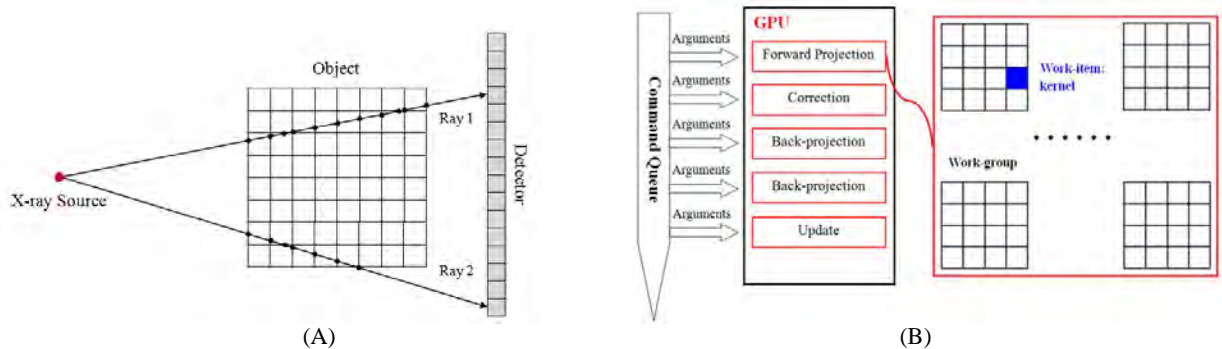
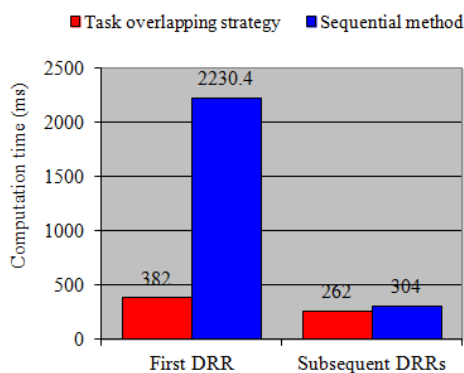


Figure 11. (A) Illustration of the ray trace method for calculating the line integral along different rays for a two-dimensional object. (B) The GPU architecture used to parallel-process the forward and backward projections in (A).

Figure 12 shows (A) the comparison of computation times for DRR generation using the task overlapping strategy and the sequential method, and (B) the speedup for DRR generation and line integral over CPU. For a phantom size of $512 \times 512 \times 223$, the time for calculating the line integrals for a 512×512 image panel was 16.2 ms on GPGPU for a monoenergetic energy source in comparison to 8.83 s on CPU. The total computation time for generating one poly-energetic projection image of 512×512 was 0.3 s (141s for CPU).

The Computation time of DRR generation on GPGPU



The speedup of DRR generation and line integral

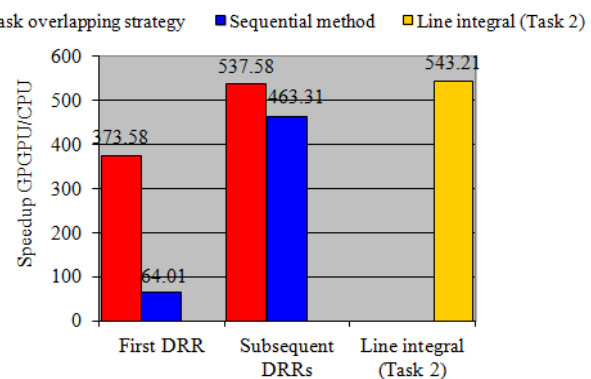
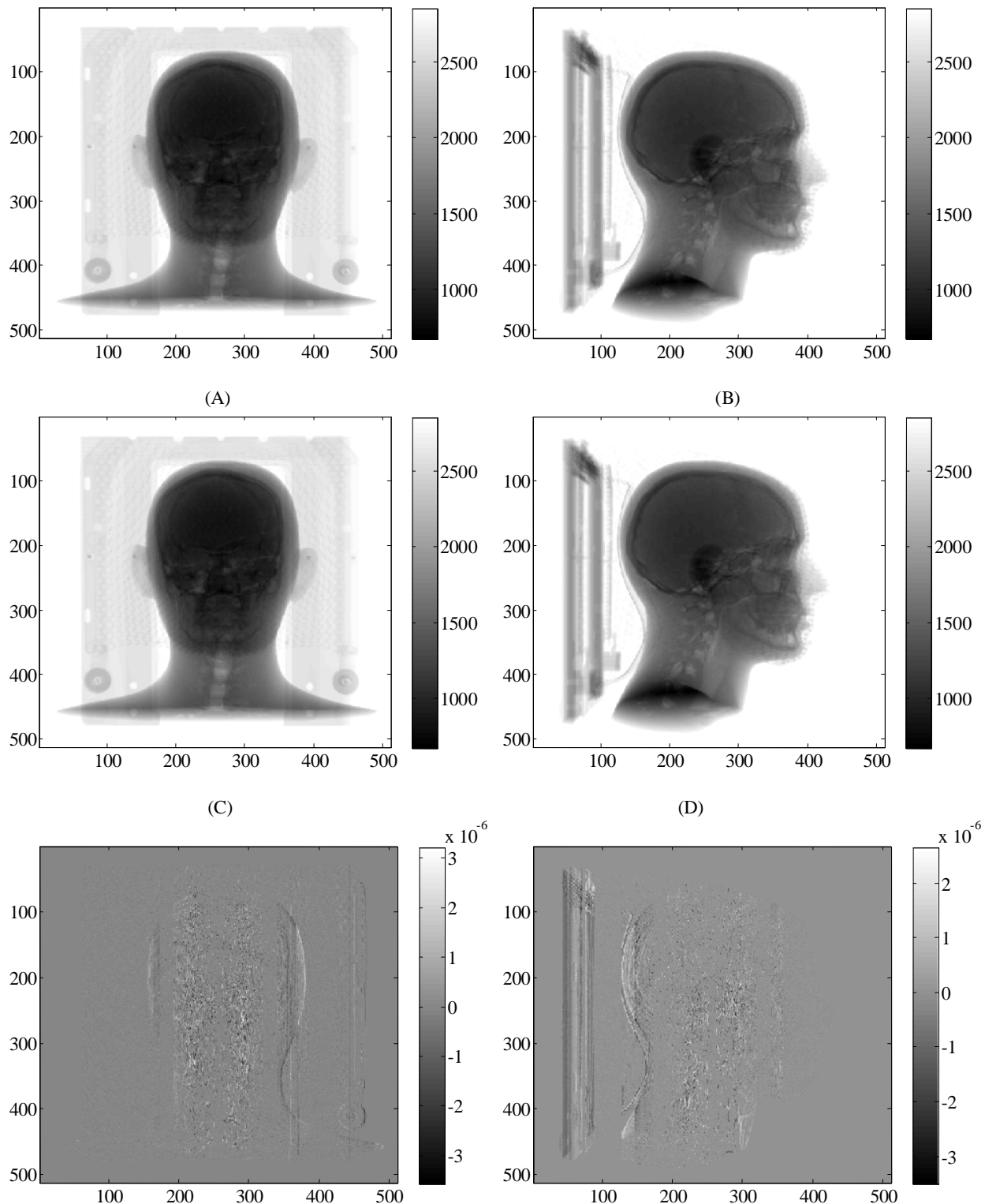


Figure 12. (A) The comparison of computation times for DRR generation using the task overlapping strategy and the sequential method. (B) The speedup for DRR generation and line integral over CPU.

Figure 13 demonstrates the projections calculated by (A) and (C) CPU-based, and (B) and (D) OpenCL-based GPU implementations. (A) and (B) at 0 degree. (C) and (D) at 90 degree. The relative difference images of (A) and (C) is shown in (E), and the relative difference of (B) and (D) in (F). The relative

difference between the projection images obtained with the CPU-based and OpenCL/GPGPU-based implementations was on the order of 10^{-6} and was virtually indistinguishable. The task overlapping strategy was 5.84 and 1.16 times faster than the sequential method for the first and the subsequent DRRs, respectively.



(E)

(F)

Figure 13. The projections calculated by (A) and (C) CPU-based, and (B) and (D) OpenCL-based GPU implementations. (A) and (B) at 0 degree. (C) and (D) at 90 degree. The relative difference images of (A) and (C) is shown in (E), and the relative difference of (B) and (D) in (F).

2.3. Construct hardware and software motions phantoms to simulation breathing motion during treatment.

2.3.A. Software Phantom

Simulated projection images of digital phantoms constructed from CT scans have been widely used for clinical and research applications but their quality are not optimal for comparison with the radiography acquired with an x-ray source of different energies. To address this issue, we propose to build digitally constructed attenuation phantoms by segmenting the anatomical CT images into different tissue types and assigning each tissue type with the attenuation coefficients for different X-ray energies.

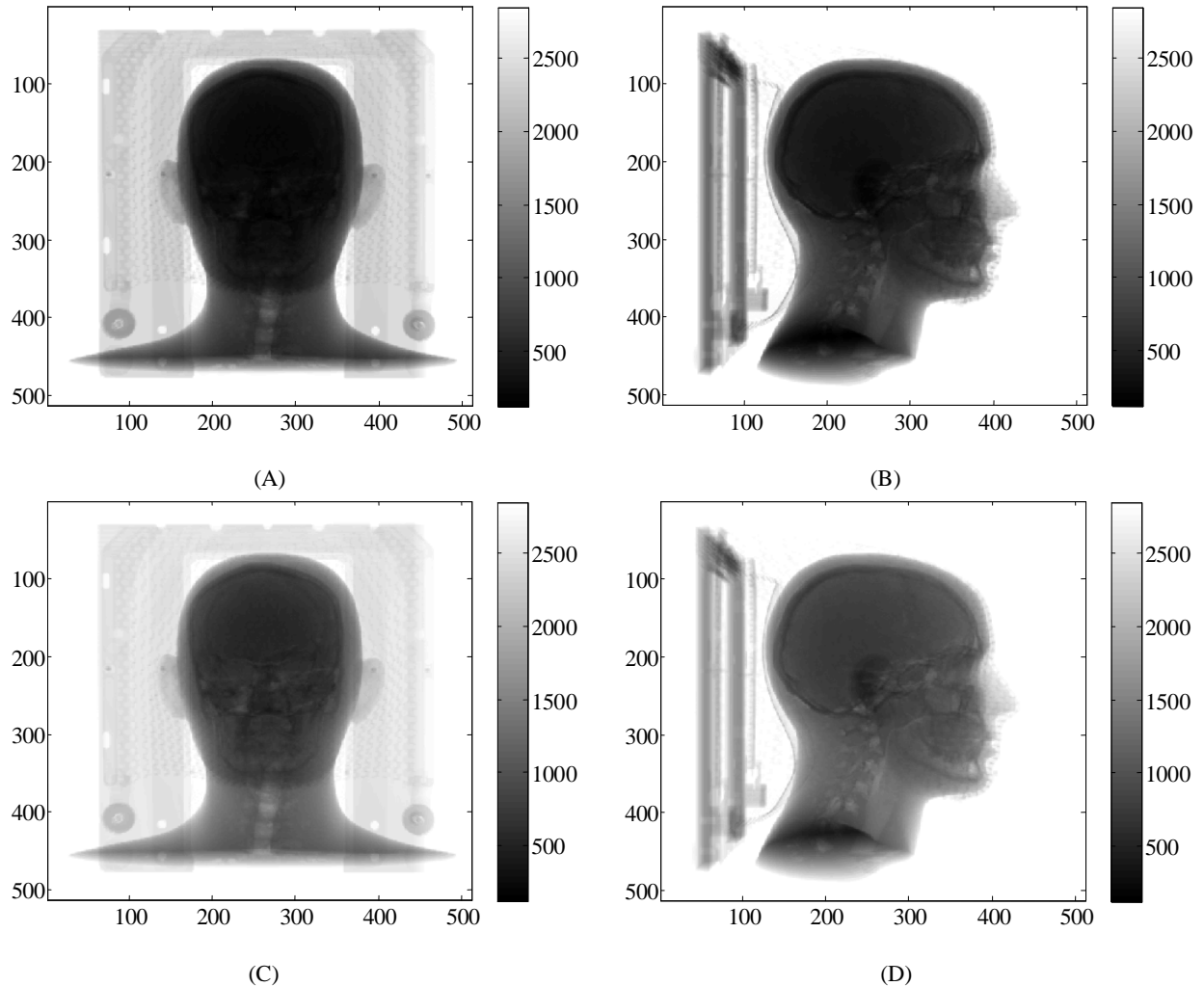
The x-ray source can be a radioisotope or an x-ray generator with a known spectrum described as weight $w(n)$ for energy bin $E(n)$. The proposed poly-energetic forward projection uses a lookup table containing the NIST published mass attenuation coefficients (μ/ρ) for different tissue types and photon energies ranging from 1keV to 20MeV. The CT images of interested sites are first segmented into different tissue types based on the CT numbers, and converted to a three-dimensional attenuation phantom by linking each voxel to the corresponding tissue type in the lookup table. The Siddon's method is used to compute the x-ray transmission line integral for $E(n)$ and the x-ray fluence is the weighted sum of the exponential of line integral for all energy bins with added Poisson noise.

To validate this method, a digital head and neck phantom constructed from the CT scan of a Rando head phantom was segmented into three (air, grey/white matter and bone) regions for calculating the poly-energetic projection images for the Mohan 4MV energy spectrum. Figure 14 shows the projection images at 0 degree (the 1st column) and 90 degree (the 2nd column) for (A) and (B) 0.25 MeV, (C) and (D) 0.75 MeV, and (E) and (F) 4.0 MeV. The projection images were generally similar to typical portal images obtained with a 4 or 6 MV x-ray source on a high-energy linear accelerator.

In addition to the home made phantom. We have also licensed the 4D NURBS-based Cardiac-Torso (XCAT) digital phantom program from the Duke University and have performed preliminary tests. The XCAT phantom was originally developed to provide a realistic and flexible model of the human anatomy and physiology for use in nuclear medicine research, specifically single-photon emission computed tomography (SPECT) and positron emission tomography (PET). The XCAT phantom was extended to four dimensions to model common patient motions such as the cardiac and respiratory motions using 4D tagged magnetic resonance imaging (MRI) data and 4D high-resolution respiratory-gated CT data respectively. Both datasets were acquired from normal patient volunteers. With its basis upon human data and the inherent flexibility of the NURBS primitives, the result is a computer-generated phantom that closely resembles the anatomical structures and cardiac and respiratory motions of a normal human subject. Combined with accurate models of the imaging process, the 4D XCAT is capable of simulating imaging data close to that of actual patients. The 4D XCAT phantom has provided an excellent tool with which to study the effects of anatomy and patient motions on SPECT and PET images. It is widely used in nuclear medicine imaging research.

The XCAT phantom is capable of simulating two physical models: a 3D distribution of attenuation coefficients for a given photon energy (attenuation phantoms) and a 3D distribution of emission radionuclide activity for the various organs (activity phantoms). It has a spherical lesion generator that will create phantoms of the user defined lesion. It also has a vector generator that will output motion vectors as determined from the phantom surfaces. Figure 15 shows the CBCT reconstruction results from projection images simulated with the XCAT digital phantom.

In conclusions, we have successfully built digital phantoms using anatomic CT images and NIST μ/ρ tables for simulating realistic poly-energetic projection images and optimized the processing speed with parallel computing using GPGPU/OpenCL-based implementation. The computation time was fast (0.3 s per projection image) enough for real time IGRT (image-guided radiotherapy) applications. We have also licensed the XCAT phantom that can simulation the projection images of the moving object inside the thorax. Both phantoms have being used to generate projection images for other studies and will be used continuously for the projects of the 3rd year.



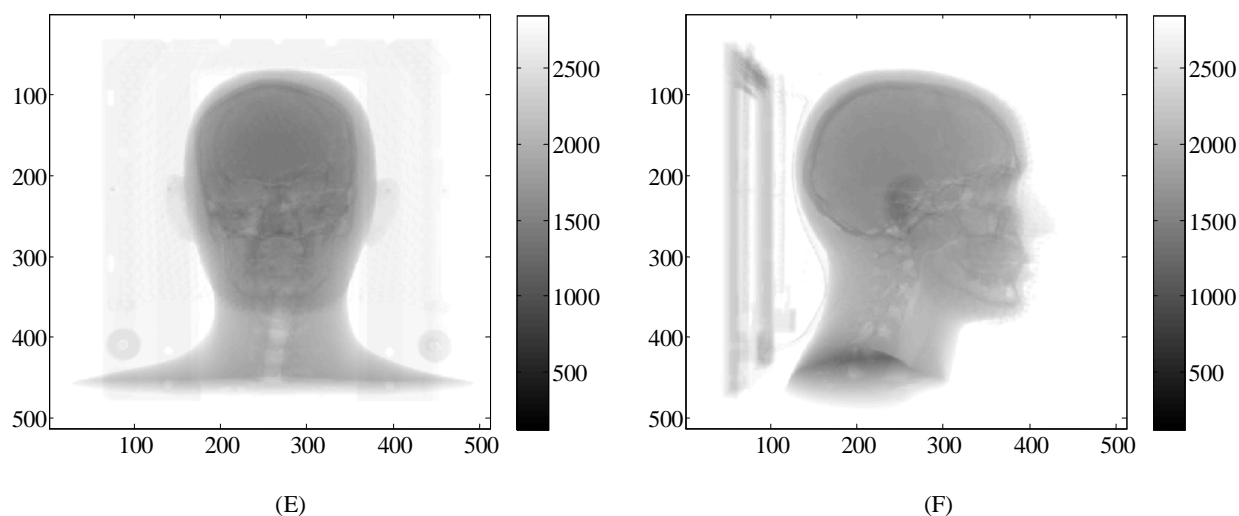


Figure 14. Projection images at 0 degree (the 1st column) and 90 degree (the 2nd column) for (A) and (B) 0.25 MeV, (C) and (D) 0.75 MeV, and (E) and (F) 4.0 MeV.

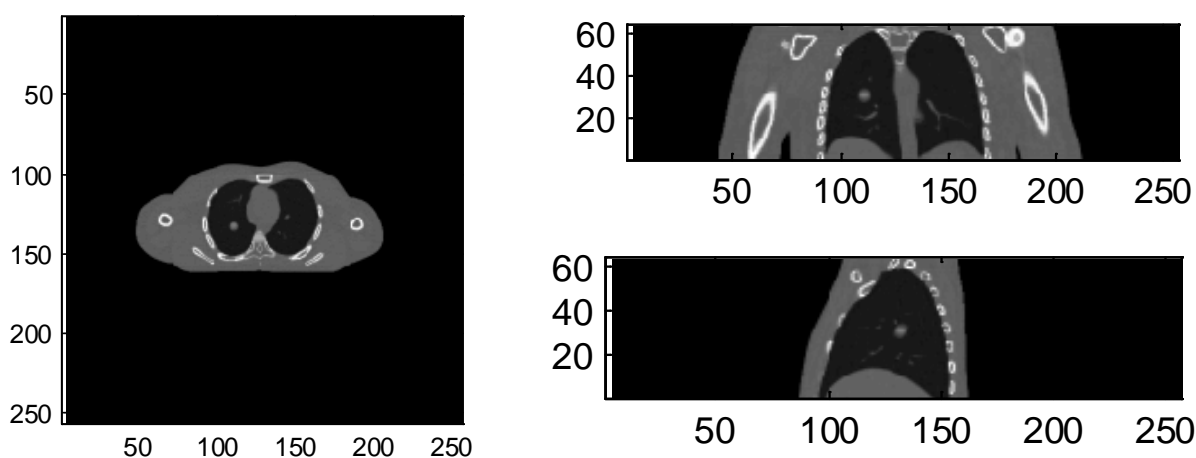


Figure 15. The CBCT reconstruction results from projection images simulated by the XCAT digital phantom.

2.3.A. Hardware Phantom - Personalized Motion Phantom for Radiotherapy

The requirements for the hardware phantom have been formulated. This project consists of hardware and software developments. For hardware development we will build a 3D moving phantom driven by DC or servo motors. For the software part we will develop codes capable of importing the 4D CT, segmenting the tumor for each breathing phase, and modeling the tumor trajectory for the full breathing cycle. The whole system need to be run on battery so that it can be positioned on a rotating platform for CBCT acquisition.

The final product should be able to

- (1) Import the 4D CT of a patient.
- (2) Identify the lung tumor position for each breathing phase.
- (3) Reconstruct the moving path of the tumor.
- (4) Control the phantom movement to emulate the tumor motion for different breathing phases.
- (5) Run on battery.
- (6) Be positioned on a rotating platform for CBCT acquisition.

We have contacted a few vendors for building a hardware motion phantom. Figure 16 show the front, right, and top views of the design of the hardware motion phantom by a vendor.

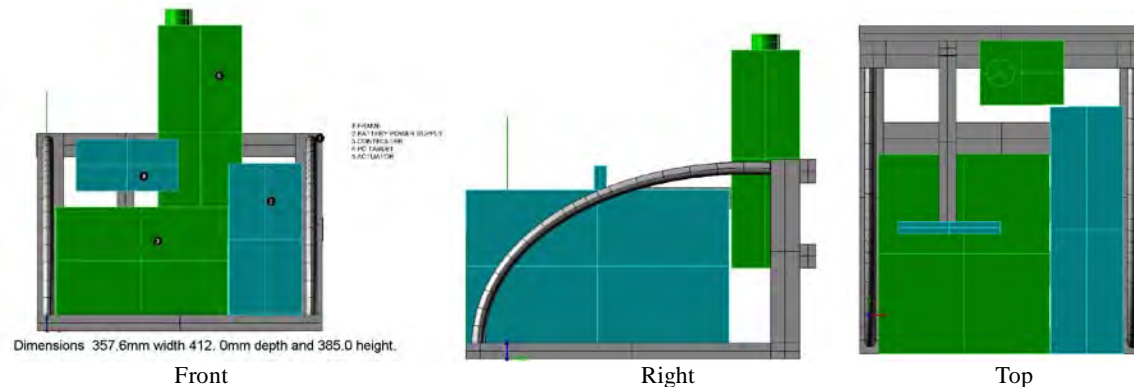


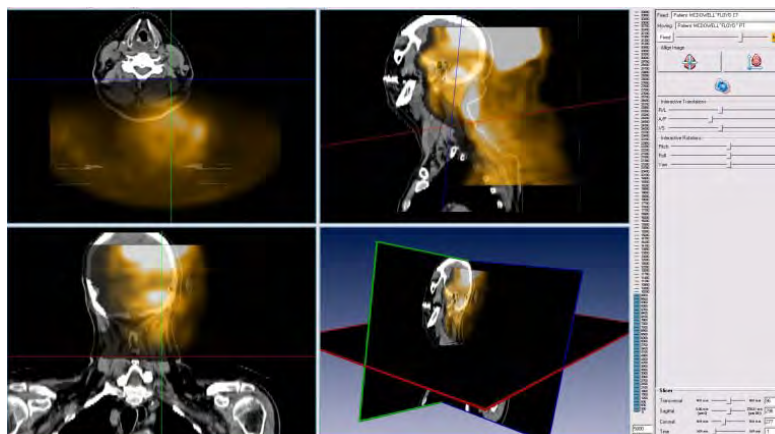
Figure 16. The front, right, and top views of the design of the hardware motion phantom by a vendor.

We are not satisfied with this design as it doesn't meet with all the above requirements. We are still looking for other vendors or potential collaborators who might build this phantom for this project. With the proposed motion phantom the accuracy of the motion management technique can be evaluated before the first treatment for each individual patient. Potential delivery errors can be identified and corrected during the planning stage. In addition, the proposed motion phantom can also be used to test new motion management techniques that are being developed.

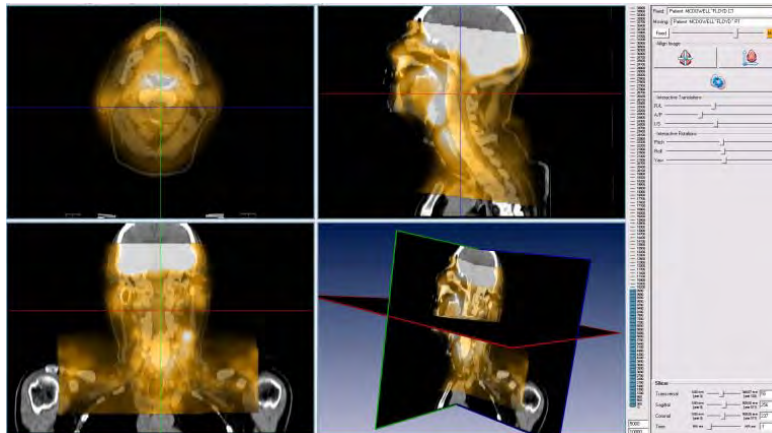
2.4. Build and test a real-time image-guided software module for patient setup and motion management.

We have formulated the first stage requirements of the real-time image-guided software module. We have also identified specific software development toolkits (e.g. ITK and VTK) for medical image processing that might be potentially suitable for our project aims. The real-time image-guided software will require four major modules: (1) interface to the on-board imaging (OBI) system, (2) automatic image registration /fusion function, (3) automatic image segmentation (contouring) function and (4) patient shift / re-localization data feedback to the treatment machine / control console.

We already looked into the first module requirement for image importing /interface to the OBI device. We have selected an open-source DICOM toolkit named DCMTK. This toolkit has the codes for importing DICOM images and DICOM RT structure sets. Our software will parse the DICOM data and store them in a designed DICOM data structure in the computer memory for further program use. Figure 17 demonstrates the image registration. The daily cone-beam CT images are processed using the deformable image registration (DIR) algorithm based on the Tx plan images and contours for tumor target and critical organs. The result of DIR is the contours automatically generated onto the daily CT images



(A) Pre-Registration: daily cone-beam CT images are off from the Tx plan images due to patient setup uncertainties



(B) Automatic Image Registration: the Tx and daily images are aligned with patient shift calculated

Figure 17. Demonstration of the image registration algorithm.

We are planning to look into the mutual information algorithm and deformable image registration algorithm in ITK to conduct some feasibility studies. A feasibility study for the integration of the development tools will be conducted and tested in the 1st quarter of the 3rd year.

3. Develop a real-time image-guided treatment planning system for the dedicated breast radiotherapy apparatus in Aim 1 and 2:

3.1. Develop an inverse planning algorithm for the proprietary delivery mechanism.

3.1.A. Forward Planning

A simple treatment planning system for the proposed APBI machine was developed using Clarkson algorithm for dose calculation and 3D mathematical functions to define patient body, treatment targets and organs at risk. A spherical coordinate system was used to represent the radiation source positions. A discrete Cartesian coordinate systems was used to represent the phantom/patient data and a continuous Cartesian coordinate systems was used for dose calculation , i.e., dose matrix. Dose to a voxel was calculated using TMR and OAR:

$$DV = MU \times OF \times TMR(d) \times OAR(OAD).$$

A mathematical phantom has been created with an elliptical cross-section of a major axis of 25 cm and a minor axis of 15 cm; superior-inferior direction has an infinite length. Dose grid contains 100×100×100 elements, with 0.2 cm spacing. This gives a volume of 20×20×20 cm³. There are four delivery cones at 50, 70, 100 and 120 degree polar angles (40, 20, -10 and -30 from the transverse iso-plane). 18, 22, 23 and 20 non-coplanar beams are placed on the above cones respectively; the arc length between neighboring sources on a cone is fixed. Iso-center is positioned at (5, 0, 0) and (-5, 0, 0) respectively.

Figure 17 shows the results of the simple TPS system. Figure 17A is the dose distributions on three orthogonal iso-planes, demonstrating that the proposed beam arrangement leads to highly conformed ellipsoid dose concentration. Figure 17B is the dose distribution on a plane 4 cm upstream the iso-center (Z plane), showing the entrance dose from the two cones at the polar angles 50 and 70 degree. Figure 17C is the central profile extracted from the iso-plane perpendicular to the central axis of the delivery cone. Dose is concentrated at the center with low entrance dose, much like a proton dose distribution.

We plan to develop inverse planning for the proposed APBI geometry using this simple TPS, followed by CT-based TPS using pencil beam algorithm.

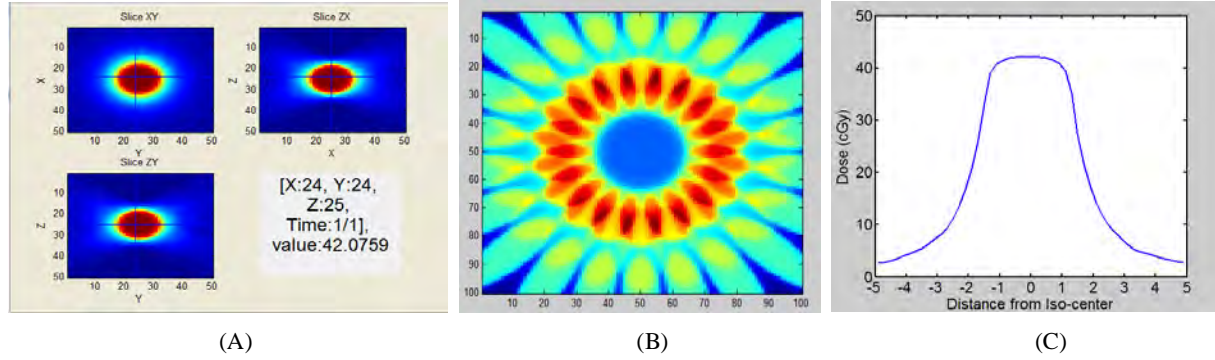


Figure 18. Results of the simple TPS system (A) Displayed are dose distributions on three orthogonal iso-planes (B) Dose distribution on a plane 4 cm upstream the iso-center (Z plane) (C) Central profile extracted from the iso-plane perpendicular to the central axis of the delivery cone.

3.1.B. Inverse Planning

The goal of this study is to develop the algorithm for multiple beam configurations to deliver a prescribed dose to the planning target volume (PTV) while sparing surrounding organs at risk (OARs). This goal can be achieved by delivering a prescribed radiation dose to the target with high conformity and by reducing the radiation doses received by OARs. Because PTV coverage and OAR sparing are generally contradictory, importance factors are usually adopted to express their relative importance. In this study, we defined the cost function $F(X, K)$ as following :

$$F(X, K) = k_0(K)(D_{\min, PTV}(X) - \overline{D_{PTV}})^2 + \sum_{i=1}^M k_i [D_{\max, OAR}(X) - \overline{D_{OAR_i}}]$$

where $D_{\min, PTV}(X)$ is the minimum dose in PTV and $D_{\max, OAR}(X)$ is the maximum dose in OARs respectively for each structure i ($i = 1, \dots, M$) as a function of beam weight (X). M is the total number of structures involved, including OAR or other healthy tissues (OHT). $\overline{D_{PTV}}$ is the desired dose for the PTV, $\overline{D_{OAR}}$ is the tolerance dose for OAR and k_i represents the relative importance of the i -th structure showing its priority for optimization as a function of K . Different sets of importance factors will have different characteristics and will result in different final plans. X represents the set of beam weights so that $D_{\min, PTV}(X)$ and $D_{\max, OAR}(X)$ can be expressed by

$$D_{\min, PTV}(X) = [\sum_{j=1}^N d_{ij} x_j]_{i=1 \dots l}^-$$

$$D_{\max, OAR}(X) = [\sum_{j=1}^N d_{ij} x_j]_{i=1 \dots l}^+$$

where d_{ij} is the dose per volume with unit beam weight from the j th beam to i th unit volume within PTV or OAR and $[x]^+([x]^-)$ is defined as maximum(minimum) dose in the unit volume among total l unit volumes. N is the total number of beams. For this study we assumed the beam weight x_j is either 0 or 1 so that we will find the best beam combination in 2^N sets of total beam configurations.

For OAR we only considered the surrounding tissues around PTV for this study and the importance factor was 1 as well as $D_{OAR} = 0$ for the simplest case. Later we will include complex OAR structures with various importance factor and possibly floating number of beam weights if we need.

In this study, the genetic algorithm mimicking the pass of randomly mutated genes from the parent to the offsprings was used to optimize the cost function. The strategy was to produce offsprings of the parent beam arrangement by randomly turning on/off certain beams and evaluate the cost function for each offspring. The offspring with the minimum cost function was identified and became the next parent for further optimization. This process is repeated until the stop condition is met.

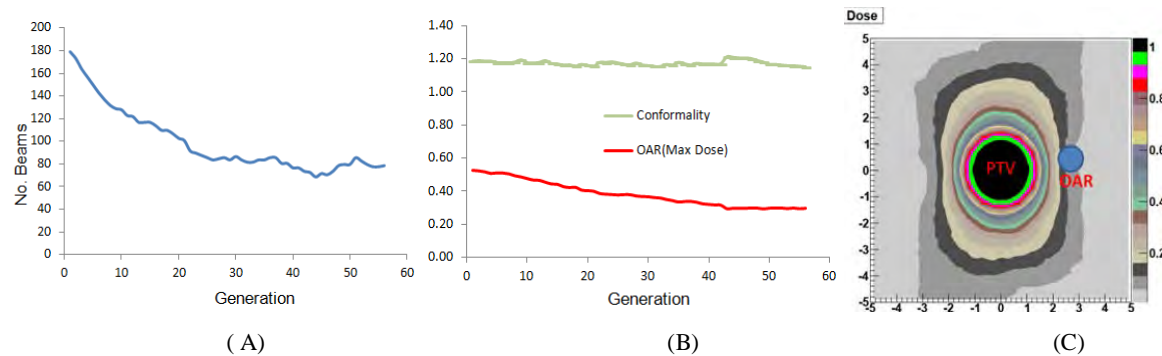


Figure 19. Illustration of the inverse planning using the genetic algorithm. (A) The change of the number of beams that remains open as a function of generation number. (B) The decrease of maximal dose to OAR as the generation increases. The conformity index remains the same instead of going lower since it has a lower priority than the dose to OAR. (C) The final optimized dose distribution showing that the dose cloud is pushed in the anterior- and posterior-direction to spare the OAR.

Figure 19 illustrates of the inverse planning results using the genetic algorithm. Initially, all 180 beams were open. Figure 19A shows the change of the number of beams that remains open as a function of generation number. As the number of generation increases, the maximal dose to OAR decreases (Figure 19B). The conformity index remains the same instead of going lower since it has a lower priority than the dose to OAR. Figure 19C is the final optimized dose distribution showing that the dose cloud is pushed in the anterior- and posterior-direction to spare the OAR.

3.2. Explore an efficient scheme for real-time re-planning of the treatment based on the tumor location and deformation.

As shown in Figures 1 and 2. There are no scheduled tasks for this subaim during Year 2. We plan to explore the real-time re-planning of the treatment based on the tumor location and deformation after the simple treatment planning system in Aim 3.1 is fully functional.

Discussion of Year 2 Project Results

We have made significant progress in the second year for this grant. Most aims are on or ahead of schedule although some aims are delayed due to slow recruiting. We believe we can make up the lost time once the reasons for the delay are fixed.

In year 2 we focus on building each sub-system of the proposed APBI apparatus - Aim 1 for the x-ray generator, Aim 2 for the imaging sub system and Aim 3 for the treatment planning. For Aim 1 we are concentrating on analyzing the shielding cost and imaging quality for different energies using Monte Carlo simulations. These results are critical to our final decision on the x-ray energy for the proposed APBI machine.

The panoramic CBCT technology is the heart of the imaging sub system as it reduces the hardware cost (smaller panel is cheaper) and construction cost (requiring less space). Good image stitching algorithms are essential to panoramic CBCT. In addition, the CBCT reconstruction must be available immediately after the scan. To these ends, we have spent a significant amount of resources on image stitching algorithms and developed parallel processing schemes using GPU for speeding up CBCT reconstructions.

Treatment planning is also critical to a successful radiotherapy system. Because the design of the proposed APBI machine is different from conventional linac, a new treatment planning system must be built. Since the main difference is the irradiation geometry, the conventional dose calculation algorithms like Clarkson or pencil beam convolution method are still applicable and the

development of the new treatment planning is focusing on how to take advantages of the proposed novel irradiation geometries.

References

- ¹ P. R. Almond, P. J. Biggs, B. M. Coursey, W. F. Hanson, M. S. Huq, R. Nath, and D. W. O. Rogers, "AAPM's TG-51 protocol for clinical reference dosimetry of high-energy photon and electron beams," *Medical Physics* **26**, 1847-1870 (1999).
- ² R. Alfonso, P. Andreo, R. Capote, M. S. Huq, W. Kilby, P. Kjall, T. R. Mackie, H. Palmans, K. Rosser, J. Seuntjens, W. Ullrich, and S. Vatnitsky, "A new formalism for reference dosimetry of small and nonstandard fields," *Medical Physics* **35**, 5179-5186 (2008).
- ³ I. A. Feldkamp, L. C. Davis, and J. W. Kress, "PRACTICAL CONE-BEAM ALGORITHM.," *Journal of the Optical Society of America A: Optics and Image Science, and Vision* **1**, 612-619 (1984).
- ⁴ K. Mueller and R. Yagel, "Rapid 3-D cone-beam reconstruction with the simultaneous algebraic reconstruction technique (SART) using 2-D texture mapping hardware," *Medical Imaging, IEEE Transactions on* **19**, 1227-1237 (2000).
- ⁵ R. L. Siddon, "Fast calculation of the exact radiological path for a three-dimensional CT array," *Medical Physics* **12**, 252-255 (1985).
- ⁶ E. Mainegra-Hing and I. Kawrakow, "Fast Monte Carlo calculation of scatter corrections for CBCT images," *Journal of Physics: Conference Series* **102**, 012017 (2008).
- ⁷ E. Mainegra-Hing and I. Kawrakow, "Variance reduction techniques for fast Monte Carlo CBCT scatter correction calculations," *Physics in Medicine and Biology* **55**, 4495 (2010).
- ⁸ P. B. Greer, "Correction of pixel sensitivity variation and off-axis response for amorphous silicon EPID dosimetry," *Medical Physics* **32**, 3558-3568 (2005).

Appendix: Year 2 Publications

1. J. Chang, L. Zhou, S. Wang, KSC. Chao, "Panoramic cone beam computed tomography," *Medical Physics* 2012;39:2930-2946.
2. L. Zhou, K. S. C. Chao, and J. Chang, "Fast Poly-energetic Forward Projection for Image Formation Using OpenCL on a Heterogeneous Parallel Computing Platform," submitted to the *Medical Physics*.
3. R. Bassalow, A. Sabbas, M. Delamerced, S. Trichter, F. Kulidzhanov, L. Nedialkova, D. Nori, K. Chao, and J. Chang, "SU-E-T-337: Monte-Carlo Study of Dose Perturbation Effects in External Beam Therapy of the Prostate Caused by the Presence of Post?Implant Brachytherapy Seeds," *Proc. AAPM 2010 Annual Meeting, Medical Physics* **38**, 3565-3565 (2011).
4. R. Bassalow, S. Trichter, A. Sabbas, B. Parashar, F. Kulidzhanov, L. Nedialkova, G. Wernicke, D. Nori, K. Chao, and J. Chang, "SU-E-T-582: Monte?Carlo Study of Dosimetric Effects of Brachytherapy Seeds Presence in Lung External Beam SBRT," *Proc. AAPM 2011 Annual Meeting, Medical Physics* **38**, 3623-3623 (2011).
5. J. Chang, L. Zhou, and K. Chao, "SU-E-J-10: Panoramic Cone Beam Computed Tomography (CBCT)," *Proc. AAPM 2011 Annual Meeting, Medical Physics* **38**, 3443-3443 (2011).
6. F. Kulidzhanov, A. Sabbas, J. Chang, S. Trichter, M. Hayes, G. Wernicke, D. Nori, and K. Chao, "SU-E-T-497: Experience in Prone Breast Setup Accuracy Improvment," *Proc. AAPM 2011 Annual Meeting, Medical Physics* **38**, 3603-3603 (2011).
7. A. Sabbas, F. Kulidzhanov, S. Trichter, R. Bassalow, B. Biritz, B. Parashar, D. Nori, K. S. Chao, and J. Chang, "SU-E-T-574: Assessment of Target Motion in SBRT Lung Patients Using the Frame? Based Stereotactic Coordinates," *Proc. AAPM 2011 Annual Meeting, Medical Physics* **38**, 3621-3621 (2011).
8. S. Trichter, S. Chiu?Tsao, M. Zaider, A. Sabbas, F. Kulidzhanov, J. Chang, G. Cohen, D. Nori, and K. Chao, "WE-A-BRB-01: Accurate Dosimetric Characterization of a Fully Loaded 20 Mm COMS I-125 Eye Plaque Using Specially Designed GAFCHROMICTM Film," *Proc. AAPM 2011 Annual Meeting, Medical Physics* **38**, 3791-3791 (2011).
9. L. Zhou and J. Chang, "SU-E-J-23: Construction of Digital Phantoms for X-Ray Image?Guided Radiotherapy (IGRT)," *Proc. AAPM 2011 Annual Meeting, Medical Physics* **38**, 3446-3447 (2011).
10. L. Nedialkova, M. Delamerced, A. Sabbas, J. Chang, and C. Chao, "Non-Vertical Co-Planar Beam Arrangement Can Improve Dose to Organs at Risk (OARs)," *International journal of radiation oncology, biology, physics* **81**, S907 (2011).
11. L. Zhou, Y. Chi, K. S. C. Chao, and J. Chang, "Feasibility Study of Panoramic Cone Beam Computed Tomography (CBCT)," *International journal of radiation oncology, biology, physics* **81**, S825 (2011).
12. P. Yan, L. Zhou, Z. Li, Y. Chi, J. Chang, and C. Chao, "SU-C-BRA-01: 4D Cone-Beam CT Acquisition Using Respiratory Phase Predication Technique," *Proc. AAPM 2012 Annual Meeting, Medical Physics* **39**, 3602-3602 (2012).
13. L. Zhou and J. Chang, "TH-C-BRA-03: Fast Iterative Cone Beam CT Reconstruction on GPGPU Using OpenCL," *Proc. AAPM 2012 Annual Meeting, Medical Physics* **39**, 4000-4000 (2012).

Panoramic cone beam computed tomography

Jenghwa Chang^{a)}

Radiation Oncology, NewYork-Presbyterian Hospital, New York, New York 10065 and Radiation Oncology, Weill Cornell Medical College, Cornell University, New York, New York 10065

Lili Zhou and Song Wang

Radiation Oncology, Weill Cornell Medical College, Cornell University, New York, New York 10065

K. S. Clifford Chao

Radiation Oncology, NewYork-Presbyterian Hospital, New York, New York 10065; Radiation Oncology, Weill Cornell Medical College, Cornell University, New York, New York 10065; and Radiation Oncology, College of Physicians and Surgeons, Columbia University, New York, New York 10032

(Received 22 June 2011; revised 30 March 2012; accepted for publication 3 April 2012; published 3 May 2012)

Purpose: Cone-beam computed tomography (CBCT) is the main imaging tool for image-guided radiotherapy but its functionality is limited by a small imaging volume and restricted image position (imaged at the central instead of the treatment position for peripheral lesions to avoid collisions). In this paper, the authors present the concept of “panoramic CBCT,” which can image patients at the treatment position with an imaging volume as large as practically needed.

Methods: In this novel panoramic CBCT technique, the target is scanned sequentially from multiple view angles. For each view angle, a half scan ($180^\circ + \theta_{\text{cone}}$ where θ_{cone} is the cone angle) is performed with the imaging panel positioned in any location along the beam path. The panoramic projection images of all views for the same gantry angle are then stitched together with the direct image stitching method (i.e., according to the reported imaging position) and full-fan, half-scan CBCT reconstruction is performed using the stitched projection images. To validate this imaging technique, the authors simulated cone-beam projection images of the Mathematical Cardiac Torso (MCAT) thorax phantom for three panoramic views. Gaps, repeated/missing columns, and different exposure levels were introduced between adjacent views to simulate imperfect image stitching due to uncertainties in imaging position or output fluctuation. A modified simultaneous algebraic reconstruction technique (modified SART) was developed to reconstruct CBCT images directly from the stitched projection images. As a gold standard, full-fan, full-scan (360° gantry rotation) CBCT reconstructions were also performed using projection images of one imaging panel large enough to encompass the target. Contrast-to-noise ratio (CNR) and geometric distortion were evaluated to quantify the quality of reconstructed images. Monte Carlo simulations were performed to evaluate the effect of scattering on the image quality and imaging dose for both standard and panoramic CBCT.

Results: Truncated images with artifacts were observed for the CBCT reconstruction using projection images of the central view only. When the image stitching was perfect, complete reconstruction was obtained for the panoramic CBCT using the modified SART with the image quality similar to the gold standard (full-scan, full-fan CBCT using one large imaging panel). Imperfect image stitching, on the other hand, lead to (streak, line, or ring) reconstruction artifacts, reduced CNR, and/or distorted geometry. Results from Monte Carlo simulations showed that, for identical imaging quality, the imaging dose was lower for the panoramic CBCT than that acquired with one large imaging panel. For the same imaging dose, the CNR of the three-view panoramic CBCT was 50% higher than that of the regular CBCT using one big panel.

Conclusions: The authors have developed a panoramic CBCT technique and demonstrated with simulation data that it can image tumors of any location for patients of any size at the treatment position with comparable or less imaging dose and time. However, the image quality of this CBCT technique is sensitive to the reconstruction artifacts caused by imperfect image stitching. Better algorithms are therefore needed to improve the accuracy of image stitching for panoramic CBCT.

© 2012 American Association of Physicists in Medicine. [<http://dx.doi.org/10.1118/1.4704640>]

Key words: panoramic CBCT, image stitching

I. INTRODUCTION

Image guided radiotherapy (IGRT) (Refs. 1–6) is a popular radiotherapy procedure that uses imaging devices to guide

treatment setup and dose delivery. Among many imaging/tracking devices used for IGRT, linear accelerator (linac) based cone-beam computed tomography (CBCT) (Refs. 7–18) is probably the most powerful tool for therapy

guidance. CBCT has been used as a three-dimensional (3D) imaging method in IGRT to provide volumetric information for real-time patient setup, dose verification, and treatment planning.

However, there are many drawbacks in the current implementation of CBCT. One major problem is the small imaging volume (due to small imager size) compromising the accuracy of target delineation. For example, the maximum size of a commercial amorphous silicon detector is 40 cm in width (or in the transverse direction). If an imaging panel of this size is positioned 150 cm from the source for full-fan CBCT acquisition (i.e., the central axis of the linac aligned with the center of the imaging panel), a half-scan gantry rotation corresponding to $180^\circ + \theta_{\text{cone}}$, where θ_{cone} is the cone angle, is needed to get a complete data set for CBCT reconstruction with an imaging volume of 26.7 cm in diameter.

This imaging volume of full-fan, half-scan CBCT acquisition is not large enough to encompass the full patient anatomy for almost all treatment sites, making it difficult to identify the treatment target and surrounding critical organs for image-guided setup. A “truncated” imaging volume also leads to incorrect CT numbers and reconstruction artifacts because the attenuation outside the imaging volume is backprojected into the imaging volume. De-truncation algorithms^{19,20} have been developed to extrapolate/approximate the measurements outside the imaging panel and, therefore, extend the imaging volume. However, the CT numbers obtained from these methods are still approximate and truncation artifacts/distortions still exist in reconstructed images.

The imaging volume can also be increased by shifting the imaging panel laterally up to 50%, which is usually referred to as the shifted/displaced detector scan (in micro-CT literatures) or half-fan acquisition (in IGRT literatures). This approach can theoretically double the imaging volume (e.g., to 53.4 cm in diameter). Although this imaging volume is still not large enough to cover the whole patient anatomy for most thoracic, abdominal, and pelvic cases, the associated problems (incorrect CT numbers and artifacts) are not as severe as those for the full-fan, half-scan acquisition. As a result, the half-fan acquisition has been successfully used for the majority of IGRT cases. However, half-fan CBCT requires full-scan (360°) gantry rotation, which is not always possible. Figure 1 illustrates the front view of a linac with an on-board kV imaging system (consisting of a source and an imaging panel) attached to the gantry using robotic arms, and the distances between the isocenter and the linac head, kV imaging panel and kV source. As shown in Fig. 1, among the linac head, kV imager, and kV source, the linac gantry head is closest to the isocenter and might cause a collision during a 360° gantry rotation, particularly if the couch is shifted laterally or inferiorly for peripheral lesions. Therefore, in order to avoid collisions, most patients with peripheral lesions have to be imaged at the central location instead of the real treatment position for CBCT acquisition. Moving the patient back and forth between the treatment and imaging positions is very uncomfortable for the patients, prolongs the treatment time significantly, and introduces additional uncertainties (e.g., patient motions) that need to be monitored. Moreover, this additional shift might

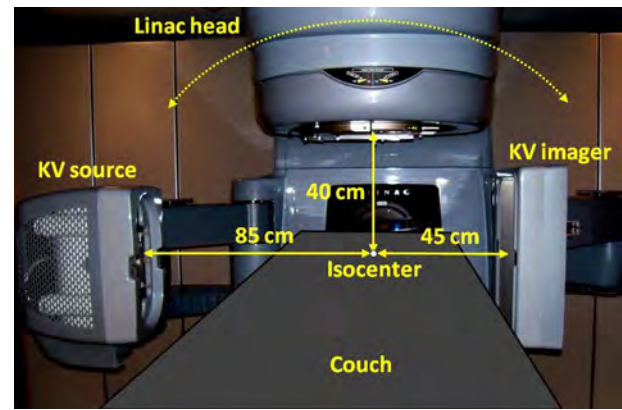


FIG. 1. The front view of a linear accelerator (linac) with an on-board kV imaging system (consisting of a source and an imaging panel) attached to the gantry using robotic arms. The distances are 40, 45, and 85 cm between the isocenter and the linac head, kV imager, and kV source, respectively; the distance between the isocenter and the kV imager can be increased (up to 85 cm) if necessary. Therefore, among the linac head, kV imager, and kV source, the linac head is most likely to collide with the couch during a 360° gantry rotation.

compromise the accuracy of image guidance because the effect of an error in measuring rotation is amplified as the point of interest (treatment isocenter) gets farther from the axis of rotation (imaging isocenter).²¹

To address these drawbacks, we developed a novel “panoramic CBCT” technique, which can image patients at the treatment position with an imaging volume as large as practically needed. It is obvious from Fig. 1 that a collision will not occur for a half-scan rotation ($180^\circ + \theta_{\text{cone}}$) if the gantry head rotates on the “far” side of the couch. So ideally, we would like to have an imaging panel large enough to encompass the whole anatomy for a full-fan, half-scan CBCT acquisition so that the linac head does not have to rotate to the “near” side of the couch. Since an imaging panel of this size does not exist, we propose to split the view of the this large imaging panel into smaller ones that can be imaged with the existing imaging panel and rotate the gantry multiple times, one half-scan rotation for each view. The projection images from multiple views can then be stitched together and reconstructed using standard reconstruction algorithms for full-fan, half-scan CBCT. The name panoramic CBCT is chosen for this CBCT technique due to its similarity to the panoramic photography.

The stitched projection images can be reconstructed using the standard FDK (Feldkamp, Davis, and Kress) algorithm,²² a type of filtered backprojection (FBP) algorithm developed for CBCT reconstruction. Data redundancy can cause artifacts for half-scan CT/CBCT reconstruction using FBP-type algorithms as some line integrals are backprojected twice while most are considered only once. Previous studies^{23–27} show that half-scan CT/CBCT reconstruction using modified weighting for FBP-type algorithms can equalize the uneven contributions for different line integrals and provide comparable image quality as the full-scan CT/CBCT reconstruction. CBCT reconstructions using the FDK algorithm are also prone to inherent shading artifacts (also referred to as

cone-beam artifacts), particularly for half-scan acquisition because the cone beam projection images acquired in a circular trajectory do not completely cover the Fourier space and do not provide complete data.^{28,29}

Another popular method for CT/CBCT reconstruction is the simultaneous algebraic reconstruction technique (SART)—an algebraic reconstruction method solving the linear system using iterative methods without direct matrix inversion. In comparison to the FBP approach, the algebraic method is generally more advantageous in CT and CBCT reconstruction using incomplete data because the algebraic method is easy to implement for different scanning geometries. In addition, it is flexible in incorporating *a priori* information about the imaging volume, is more economic in extracting tomographic information from the projection images, and does not require data weighting. For example, Mueller³⁰ demonstrated that less projections are required for the SART than for the FDK reconstruction for the same image quality. Guan and Gordan,³¹ on the other hand, showed that, for the same limited number of projections, the algebraic formulation produces better reconstructions than the FBP method. Ge *et al.*³² demonstrated that metal artifacts can be more successfully reduced with iterative reconstruction methods. Maaß *et al.* compared different CBCT reconstruction algorithms and concluded that the SART showed significantly reduced cone-beam artifacts in comparison to the FDK algorithm.³³ Finally, the study by Noo *et al.* demonstrated that variable detector sizes inside projections can be handled with SART provided that the detector geometry remains unchanged from one projection to another.³⁴

A potential source of reconstruction artifacts for panoramic CBCT is imperfect image stitching due to uncertainties in imaging position or output fluctuation. Most commercially available electronic portal imaging device (EPID) systems are attached to the linac using robotic arms, from which the location of the imaging panel is read. Grattan and McGarry³⁵ investigated the mechanical characterization of the robotic arms for commercial EPID systems and reported that the digital readout and the exact imaging position might differ by a few millimeters due to gantry sag. The exposure level of an x-ray imaging system fluctuates on the order of a few percents each time the beam is turned on for the same mAs setting. This fluctuation might cause artifacts and incorrect CT numbers in the reconstructed images because the backprojection of the projection images for each

view angle is not evenly distributed but concentrated in certain regions within the imaging volume.

In this paper, we will describe the scanning geometry for acquiring projection images for multiple panoramic views, explain the direct imaging stitching method, and present a modified SART for panoramic CBCT reconstruction. CBCT reconstructions from simulated panoramic projection images of digital phantoms will be presented and the image quality compared. Reconstruction artifacts will be studied for simulated imperfect stitching including gaps, columns missing/repeating at intersection, and exposure fluctuation between adjacent views. Results from the Monte Carlo simulations of projection images for standard and panoramic CBCT will be presented to investigate the effects of scattering on image quality and imaging dose. Finally, potential applications of this imaging technique for clinical use will be discussed.

II. METHOD AND MATERIALS

II.A. The concept of panoramic CBCT

As shown in Fig. 2(a), for panoramic CBCT, we scan the target panoramically with the source aiming at multiple view angles with a field size comparable to the size of the imaging panel, stitch together the projection images of all views for the same gantry position to form a larger projection image, and perform CBCT reconstruction using the stitched projection images. Aiming the source at multiple view angles can be achieved by either rotating the source physically or using different collimator settings as shown in Fig. 2(a). For each view angle, the imaging panel can be positioned in any location along the beam path.

Since the CBCT volume is proportional to the size of the projection data, the panoramic CBCT technique can theoretically increase the imaging volume to as large as practically needed. For most patients, two to three view angles should be sufficient to cover the whole anatomy with the commercially available EPIDs. Unlike the half-fan, full-scan CBCT scan, the panoramic CBCT can obtain complete reconstruction of any patient size using the half scan ($180^\circ + \theta_{\text{cone}}$) without having to shift the patient to the central location to avoid collisions. The panoramic CBCT also addresses the issues on reconstruction artifacts and incorrect CT numbers due to truncation.

Since the multiple panoramic views are not necessarily on the same plane, the stitched view could not be directly

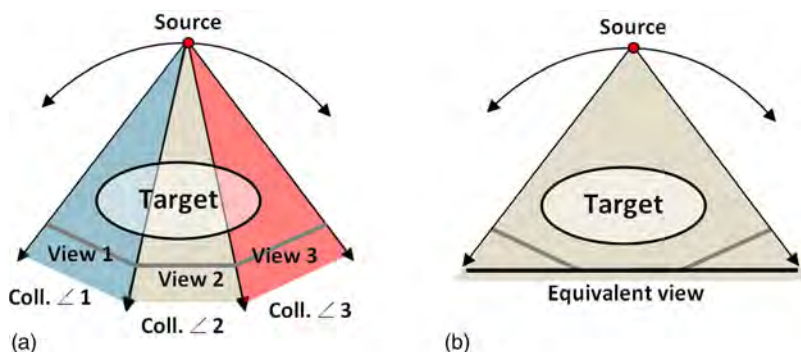


FIG. 2. Illustration of the concept of panoramic CBCT. (a) Three panoramic views achieved by sequentially collimating the source (Coll. 1, Coll. 2 or Coll. 3) to irradiate a part of the target for half scan. The field size is comparable to the size of the imaging panel positioned along the beam path for each view. (b) The “equivalent” view from the three panoramic views rebinned at a plane normal to the central axis of the source, which is equivalent to scan the target using an equivalent imaging panel large enough to encompass the whole target.

inputted into the standard FDK (Ref. 22) or SART (Ref. 36) reconstruction programs coded for cone beam geometry. Instead, as shown in Fig. 1(b), we can project and rebin the stitched projection images onto an “equivalent imaging panel” normal to the central axis by ray tracing and interpolation, considering the beam divergence to produce “equivalent projection images” for full-fan, half-scan CBCT reconstruction. Alternatively, special algorithms are required to reconstruct the CBCT directly from the stitched projection images without additional projection and rebinning.

II.B. Image stitching

Image stitching is a preprocessing of the projection data to select and group the detector readings from all panoramic views for CBCT reconstruction. Although it is not required for all CBCT reconstruction algorithms, the image stitching illustrated in Fig. 2 was performed in this study to preprocess the projection data suitable enough so that the same data set could be used to test the FBP and algebraic reconstruction algorithms and the reconstruction results could be fairly compared. Stitching of the panoramic projection images can be achieved by direct image stitching, i.e., combination of the projection images of the same gantry angle according to the imaging position reported by the controller of the robotic arms. Alternatively, image processing algorithms can be developed to stitch projection images based on the identified common features on adjacent views. If the projection images are not acquired at exactly the same gantry angles, interpolation of projection images of neighboring gantry angles is needed to produce the projection images at the desired gantry angles.

In this study, only direct image stitching based on the location of the imaging panel was used to stitch the projection images from multiple views. The imaging panel for each view was mathematically defined as a rectangle with the specified size (width \times length where width is the size in the transverse direction and length in the longitudinal direction). For direct image stitching, we first identified the intersection between two adjacent views by extending the rectangles of both imaging panels until they intersected. As shown in Fig. 3, depending on the location of the intersection, we might have (a) a match, (b) a gap, or (c) an overlap between two adjacent views if the intersection was located on the boundary, outside, or inside of an imaging panel, respectively. The stitched projection images were the union of all three projection images plus the gaps between any two adjacent views. We filled in zero intensity values for pixels in the gap region and truncated pixels in the overlap region.

The calculated gap, overlap, or match between adjacent views might not be exact because the reported imaging positions may deviate from the real ones.³⁵ In this study, we defined “perfect stitching” as an exact overlap or match and referred all other cases as “imperfect stitching.” There was no harm for perfect stitching since the data truncated from one imaging panel were acquired by the other panel. Imperfect stitching, on the other hand, might cause reconstruction artifacts as some projection data were lost, repeated, or even not

acquired. A gap [Fig. 3(b)] between two imaging panels led to missing data in the stitched view. As shown in Fig. 3(d), a few columns of pixels might potentially be repeated or missing from the stitched view if the reported imaging position was different from the true one. The potential columns missing or repeating might not materialize if the same amount of positional errors happened to other imaging panels.

II.C. Simulation of panoramic projection images using a digital phantom

The Mathematical Cardiac Torso (MCAT) phantom,³⁷ a digital anthropomorphic phantom developed for the nuclear medicine imaging research, was used to simulate the transmission projection imaging data for a 140 keV source. Two different detector geometries were simulated. The first was one large imaging panel located 150 cm from the source along the central axis. This imaging panel consists of a matrix of 516×516 detectors with a pixel size of 1.15×1.15 mm². The 59.3×59.3 cm² panel size was large enough to encompass the whole MCAT phantom. A total of 360 projection images with added Poisson noise from the primary signal were generated every degree for a 360° gantry rotation. The Siddon’s ray-trace method³⁸ was used to calculate the line integral through the phantom along the ray connecting the source to the detector pixel.

The second detector geometry included three small panoramic views with two side views tilted at 30° from the central position [Fig. 2(a)]. Different view angles were achieved by adjusting the collimator opening. Each view corresponded to a projection image with added Poisson noise from the primary signal, acquired using an imaging panel consisting of a matrix of 172×516 detectors with a pixel size of 1.15×1.15 mm². The 19.8-cm panel width was only one third of the larger panel and was not large enough to cover the whole MCAT phantom in the transverse direction. The 59.3-cm panel length for the panoramic views was the same as that for the large imaging panel. Therefore, the first detector geometry was the equivalent imaging panel for the stitched and rebinned view of the second detector geometry [Fig. 2(b)].

II.D. Simulation of reconstruction artifacts due to imperfect stitching

We also simulated different types of imperfect stitching (discussed above) that might produce reconstruction artifacts and degrade the image quality. Two experiments were performed: (1) different amounts (1, 3, and 5 mm) of gap was introduced by setting the image intensity to zero for the pixels located within half of the gap size of the intersection between two adjacent imaging panels and (2) three consecutive-columns of pixels were removed or repeated around the intersection between adjacent imaging panels. To investigate the effect of the exposure fluctuation, we also increased the pixel intensity of the projection images for the left view and the right view by 5% and 3%, respectively, and compared the CBCT reconstruction with that without the exposure fluctuation.

Note that the reconstruction artifacts studied here were not introduced during the image stitching step but were caused by detector positions that were improperly chosen (for gaps) or inaccurately reported (for missing or repeating columns). Therefore, these artifacts could not be removed using reconstruction algorithms that do not require image stitching (e.g., algebraic reconstruction algorithms) although the artifacts might appear differently for reconstructions with and without image stitching.

II.E. Image reconstructions

In this study, we programmed the standard SART for CBCT reconstruction using one single large panel or the equivalent view as shown in Fig. 2(b). We also modified the SART for direct reconstruction without rebinning. In standard SART, the correction terms are simultaneously applied for all the rays in one projection, and the linear attenuation coefficient of each voxel is updated after all rays passing through this voxel at one projection view are processed; the value update of each voxel is performed after all rays at one projection view are processed. The number of updates in one full iteration is equal to the number of projection images K and also is called the number of subiterations. Let $\hat{\mu}_j^{n,k}$ denote the estimated linear attenuation coefficient of the j th voxel at the end of the k th subiteration of the n th iteration. The initial and final update values at one iteration are assigned as follows:

$$\hat{\mu}_j^{n,1} = \hat{\mu}_j^{n-1}, \quad \hat{\mu}_j^n = \hat{\mu}_j^{n,K},$$

where $\hat{\mu}_j^n$ is the estimate at the end of the n th iteration, which is equal to the estimate after all K projection images are processed. Let \mathcal{G}_j^k denote the set of the measured line integrals passing through the j th voxel at the k th projection angle. The update of the linear attenuation coefficient at the j th voxel is defined as follows:

$$\hat{\mu}_j^{n,k+1} = \hat{\mu}_j^{n,k} + \lambda \frac{\sum_{g_i \in \mathcal{G}_j^k} \left(\frac{g_i - \sum_{j=1}^M a_{ij} \hat{\mu}_j^{n,k}}{\sum_{j=1}^M a_{ij}} \right)}{\sum_{g_i \in \mathcal{G}_j^k} a_{ij}},$$

where λ is a relaxation factor ranged over $(0, 1]$, g_i is the line integral computed from the measured projection data at the i th detector pixel, and a_{ij} the chord length of the i th ray passing through the j th voxel. The relaxation factor is used to reduce the noise during reconstruction. In some cases, this parameter is chosen as a function of the iteration number. That is, λ decreases as the number of iterations increases.

Since there are no filtering operations between detector readings, the application of the SART algorithm is not limited to the cone beam geometry [i.e., one single large panel or the equivalent imaging panel in Fig. 2(b)] if the location of each individual detector can be passed to the algorithm. Therefore, for the cone beam geometry, we used the standard SART that received the pixel size and center location of the imaging panel and calculated the location of each detector accordingly. For multiple panoramic views, this interface was modified to receive the pixel size and center location of each imaging panel separately so that the detector location for each panel

could be determined independently without rebinning. The main difference between the standard SART and the modified SART was therefore that, for the modified SART, the geometry for forward and backprojections was different for each imaging panel and was handled separately, while the cone beam geometry was assumed for the standard SART. Since no special weightings are needed and the forward/backprojections are similar for imaging planes of different positions, the code change for the modified SART was minimal.

For both standard SART and modified SART, the linear system governing the relation between the linear attenuation coefficient of each voxel and the measured line integrals is solved iteratively without direct matrix inversion. The reconstruction is generated by iteratively performing projections of intermediate estimates and backprojection of correction terms. Both processing time and image quality (the contrast and the noise) increase with the number of iterations so that a compromise is usually made considering these two factors. In this study, we used a uniform initial guess and terminated the reconstruction after the fourth iteration. Although projection images for the full-scan acquisition were simulated, reconstructions were performed mainly for the half-scan data, which can be achieved for most treatment positions without having to shift the treatment couch to the central location to avoid collisions. The reconstruction volume was a matrix of $256 \times 256 \times 256$ voxels with a voxel size of 1 mm^3 . No additional corrections and image processing were used before reconstruction.

II.F. Quantitative analysis

Contrast-to-noise (CNR) and geometric accuracy of the reconstructed images were calculated to evaluate the quality of reconstructed images. CNR for a simulated lung tumor in the MCAT phantom was computed as: $\text{CNR} = |S1 - S2|/\sigma$, where $S1$ and $S2$ were the average pixel values inside a region of interest and a background region, respectively, and σ was the standard deviation in the background region. Distances were also calculated to quantify geometric distortion: one was the distance between the centers of two selected ribs in the coronal view and the other was the distance between the centers of two selected ribs in the transverse view. The center location of each selected rib was determined by measuring and averaging the coordinates (in pixels) of the right, left, top, and bottom border of the rectangle encompassing the selected rib using the cursor function in the MATLAB Image Tool.

II.G. Analysis of scattering vs field size using Monte Carlo simulation

Monte Carlo simulations were also performed with the “egs_cbct” code^{39,40} to analyze the scattering as a function of field size for an on-board imaging panel. A 40 kV point source was simulated to irradiate a $60 \times 60 \times 30 \text{ cm}^3$ water phantom with one embedded bone insert of 20 cm length and $2 \times 2 \text{ cm}^2$ cross section. The source was placed 100 cm upstream of the isocenter and the water phantom centered at the isocenter.

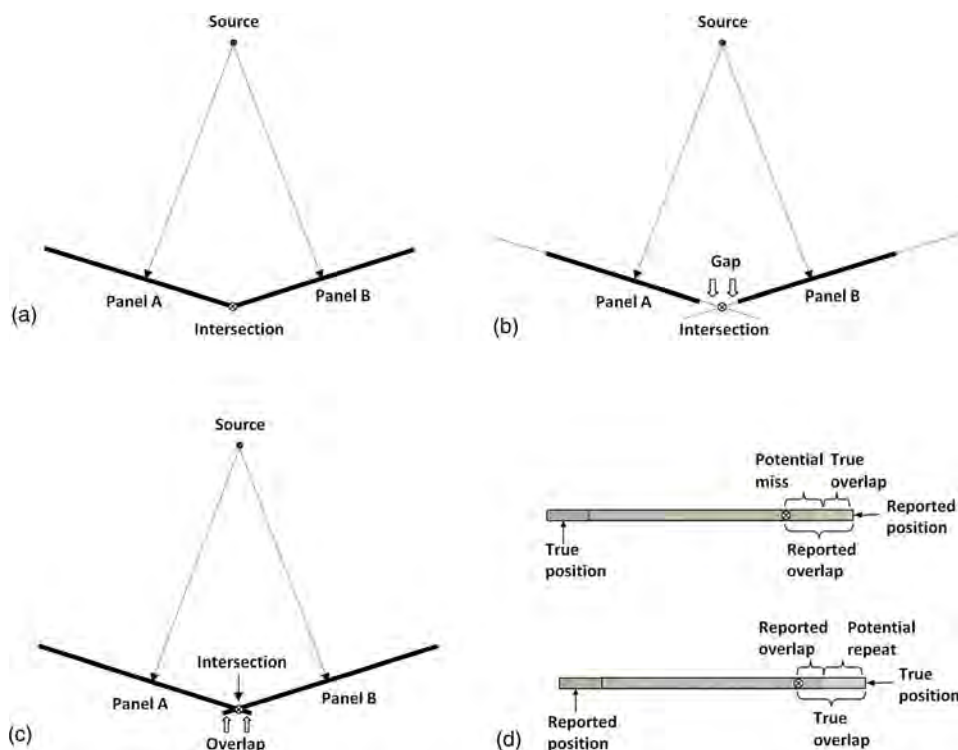




FIG. 3. Illustration of three scenarios between two adjacent views (a) a match, (b) a gap, and (c) an overlap. In this paper, we used the direct stitching method to stitch multiple views into one large view. Pixels were set to zero in the gap region and truncated in the overlap region. Panel (d) demonstrates potential columns repeating and missing if the overlap region is truncated during image stitching; : true imaging position; : reported imaging position.

The imaging panel was positioned 50 cm downstream of the isocenter and comprised 200×200 pixels with 0.2 cm pixel pitch. The projection images were simulated along the longest dimension of the bone insert. Therefore, the bones appeared as low-intensity rectangular regions in the projection images. Simulations were conducted for field sizes ranging from 5×20 to 45×20 cm² defined at the isocentric

plane (or 7.5×30 to 67.5×30 cm² at the imaging plane) while the source fluence was kept constant for all simulations. Air kerma was scored as the detector response.

The CNR was calculated for each simulated projection image as $CNR = \frac{S_{bone} - S_{water}}{\sigma_{water}}$, where S_{bone} was the mean signal of the bone projection evaluated in the central 2.4×2.4 cm² square, S_{water} was the mean signal of the water projection

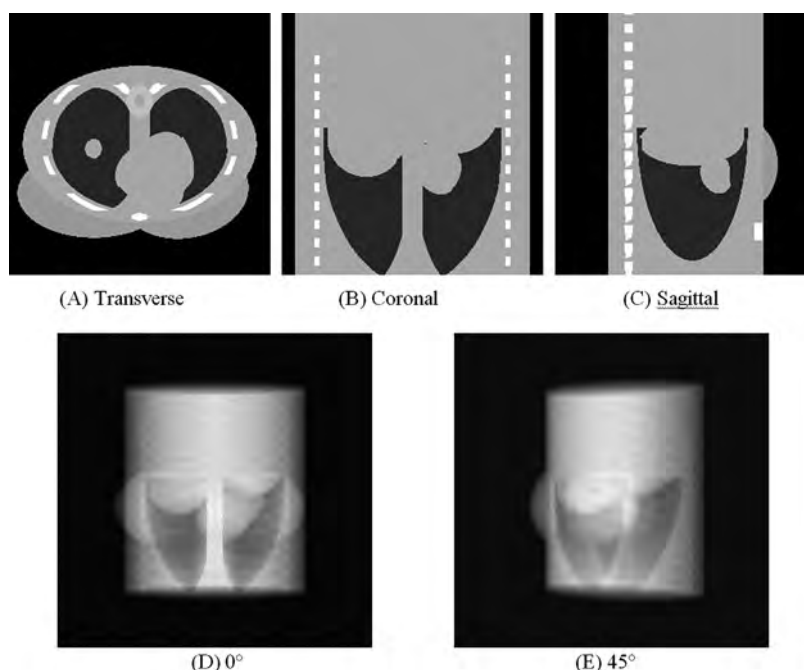


FIG. 4. (a) Transverse, (b) coronal, and (c) sagittal views of the MCAT phantom used for this study. The equivalent projection images of the three panoramic views are also shown for gantry angles (d) 0° and (e) 45°.

evaluated in the region of the central $6.8 \times 6.8 \text{ cm}^2$ square minus the central $3.6 \times 3.6 \text{ cm}^2$ square, and σ_{water} was the standard deviation in that region.

The effect of the scattering on the CBCT reconstruction for a different scanning geometry was also demonstrated by including the scattering noise in the projection images of the MCAT phantom. Since the scattering signal is a slow varying function (as will be shown later in Fig. 13), the Monte Carlo simulation was not performed for each projection image to save computation time. Instead, the scatter-to-primary ratio of the anterior-posterior view (i.e., 0° gantry angle) was calculated using the Monte Carlo simulation for the big panel and for the small panel used for the three-view panoramic CBCT, from which a constant scattering signal was added to each projection image accordingly.

For each scanning geometry, we first generated noiseless projection data every 1° for 200 gantry angles. The average pixel intensity of each noiseless projection image was

calculated, multiplied by the corresponding scatter-to-primary ratio, and added to each pixel. Poisson noise was then added based on the combined (primary and scatter photons) image intensity of each pixel to obtain the noisy projection data for CBCT reconstruction. CNRs were calculated to compare the quality of reconstructed images for one big panel and for three-view panoramic CBCT.

III. RESULTS

Figure 4 shows the (a) transverse, (b) coronal, and (c) sagittal views of the MCAT phantom, as well as the equivalent projection images of the three panoramic views for gantry angles (d) 0° and (e) 45° . Figure 5 is the comparison of the CBCT reconstruction from (a) one big panel/full scan (the standard for comparison), (b) one big panel/half scan, and (c) three panoramic views/half-scan. The standard SART was used for the CBCT reconstruction in Figs. 5(a)

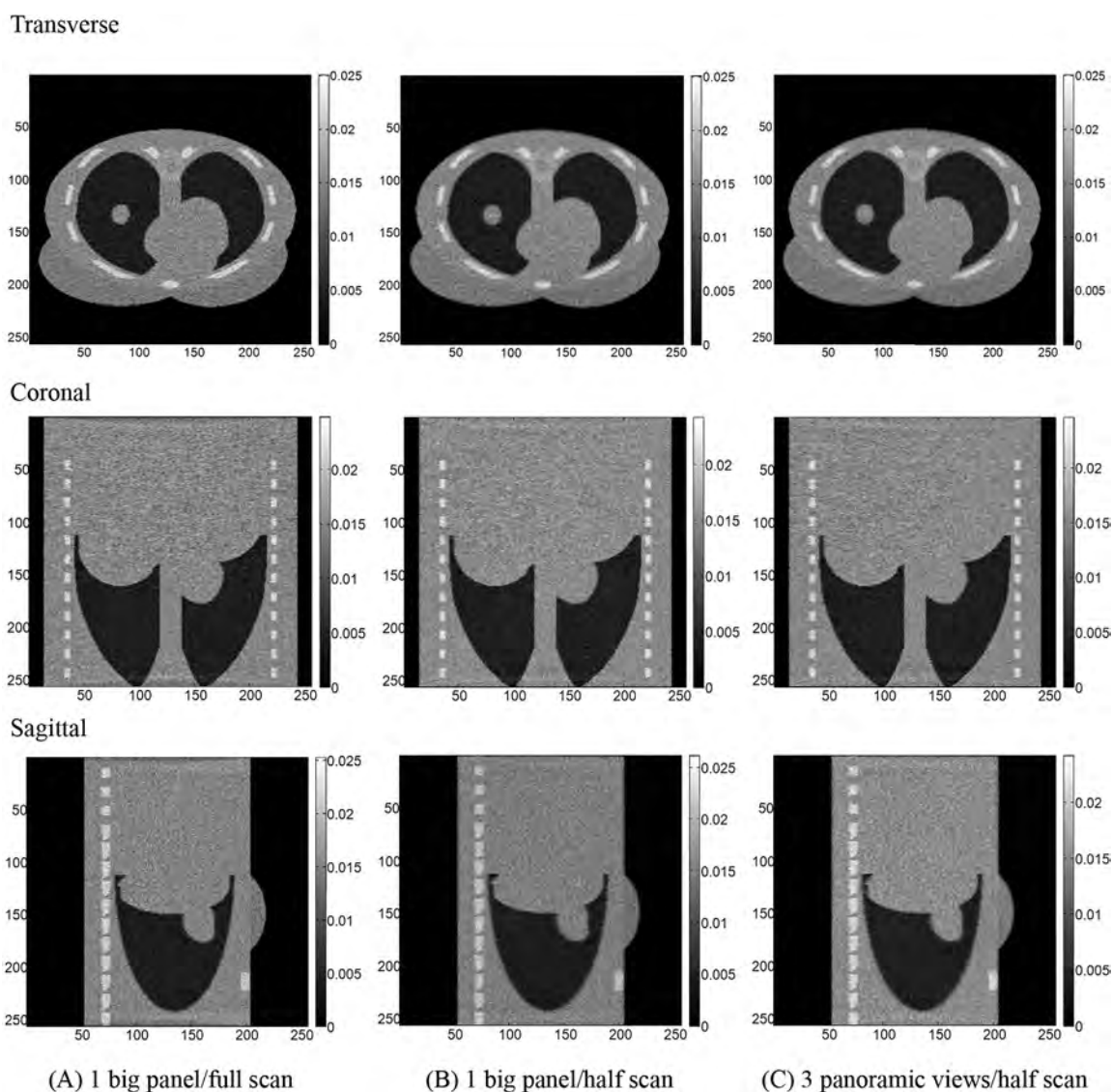


FIG. 5. Comparison of transverse, coronal, and sagittal slices for CBCT reconstructions using projection images from (a) one big panel/full scan (the standard for comparison), (b) one big panel/half scan, and (c) three panoramic views/half-scan. Standard SART was used for CBCT reconstructions of (a) and (b) while “modified SART” was used for (c). Full scan: 360° gantry rotation. Half scan: 200° gantry rotation.

and 5(b), while the modified SART was used in Fig. 5(c). Figure 6 compares the central profiles of the transverse view between the MCAT phantom and the reconstructed images for one big panel/full scan, one big panel/half scan, and three panoramic views/half scan in Fig. 5. The good agreements (other than the noise) for all comparisons in Fig. 6 validated our implementation of the standard SART and the modified SART. Figure 7 illustrates the difference images (a) between one big panel/full scan [Fig. 5(a)] and one big panel/half scan [Fig. 5(b)] and (b) between one big panel/full scans [Fig. 5(a)] and three panoramic views/half scan [Fig. 5(c)]. It is observed from Fig. 7 that the full-fan, half-scan CBCT using the standard SART and the panoramic CBCT using the modified SART were as good as the gold standard since the differences between them were mainly noise.

Figure 8 shows the transverse, coronal, and sagittal slices of the half-scan (200° gantry rotation) CBCT reconstructions using the standard SART and the projection images of the central view only. Artifacts appeared in both reconstructions. Image intensity near the boundary was significantly enhanced due to the contribution of the attenuation outside the imaging volume.

The half-scan CBCT reconstructions using three panoramic views with simulated imperfect image stitching are shown in Figs. 9–11. Figure 9 demonstrates the transverse, coronal, and sagittal slices of three-view panoramic CBCT with introduced (a) 5 mm, (b) 3 mm, and (c) 1 mm gaps between adjacent views. Streak (transverse view) and line (coronal and sagittal views) artifacts were observed in all three reconstructions. Figures 10(a) and 10(b) display the equivalent projection images of the three panoramic views for (a) 0° and (b) 45° gantry angles with three consecutive columns of pixels removed at the intersection between two adjacent views. The half-scan CBCT reconstruction is also illustrated for one (c) transverse, (d) coronal, and (e) sagittal slides with observed streak (transverse view) and line (coronal and sagittal views) artifacts. Figure 11 shows similar results and artifacts with three consecutive columns of pixels repeated at the intersection between two adjacent views.

Figure 12 demonstrates the equivalent projection images of the three panoramic views for (a) 0° and (b) 45° gantry angles with the image intensity of the left and right views increases by 5% and 3%, respectively, and the half-fan CBCT reconstruction for one (c) transverse, (d) coronal and

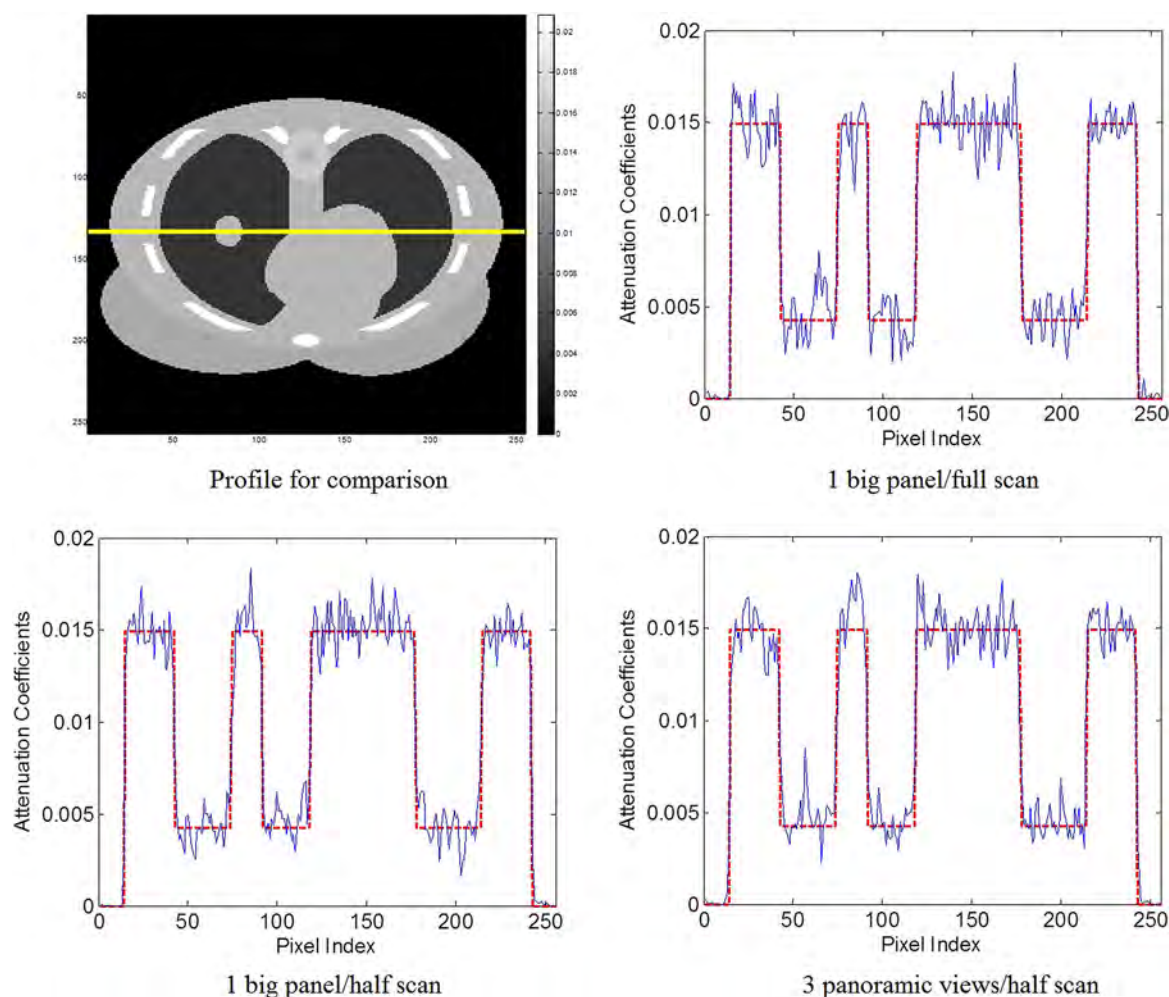


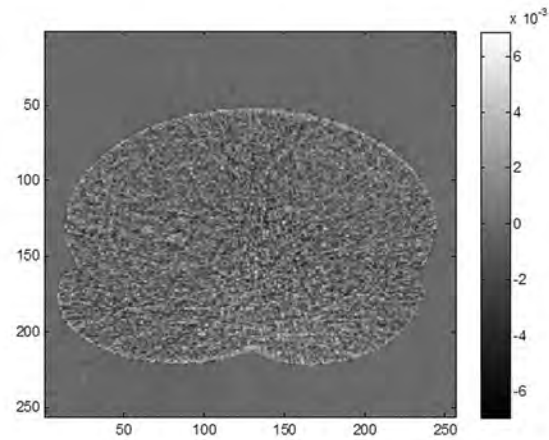
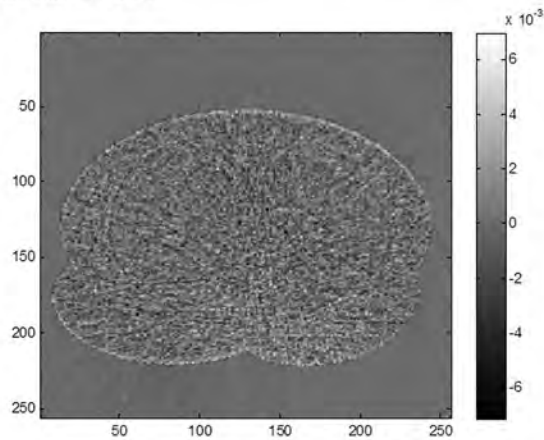
FIG. 6. Comparison of the central profiles of the transverse view between the MCAT phantom and the reconstructed images for one big panel/full scan, one big panel/half scan, and three panoramic views/half scan in Fig. 5. Dashed line: profile for MCAT phantom. Solid line: reconstructed profile.

(e) sagittal slices. Ring (transverse view) and line (coronal and sagittal views) artifacts were observed due to the introduced exposure fluctuations.

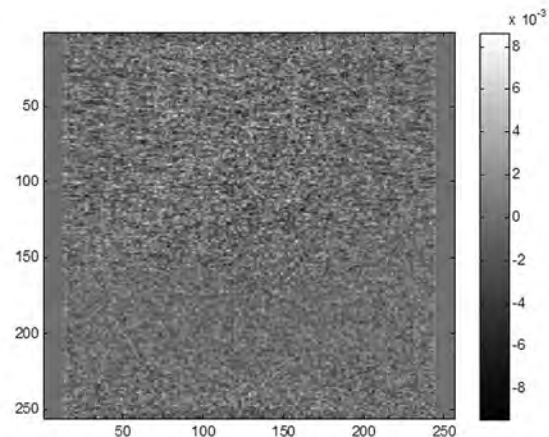
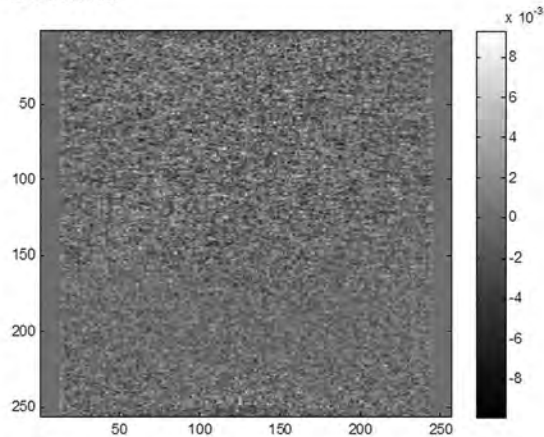
Table I shows the CNR and geometric accuracy for the reconstructed images in Figs. 5 and 8–12. CNR ranges from 6.4 to 11.5 for the simulated lung tumor (circled in the dotted

line in the upper right panel). Geometric distance between two selected ribs was also shown for one coronal view (“D1” in the upper left panel) and one transverse view (“D2” in the upper right panel). Most reconstructions have the same geometric accuracy as that in Fig. 5(a) (the gold standard) except for Figs. 10 and 11.

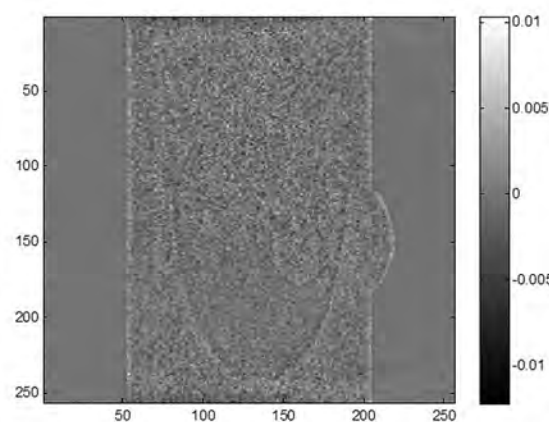
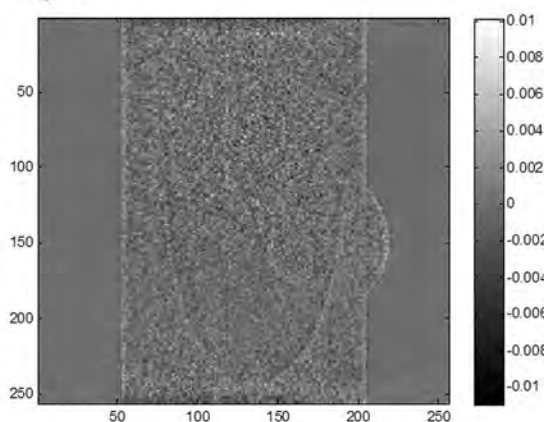
Transverse



Coronal



Sagittal



(A)

(B)

FIG. 7. The difference images (a) between one big panel/full scan [Fig. 5(a)] and one big panel/half scan [Fig. 5(b)] and (b) between one big panel/full scan [Fig. 5(a)] and three panoramic views/half scan [Fig. 5(c)].

Figure 13 illustrates the Monte Carlo simulation results for (a) the $5 \times 20 \text{ cm}^2$ field size, (b) the $45 \times 20 \text{ cm}^2$ field size, (c) the central profiles of the primary signal and total (primary + scatter) signal of both fields, and (d) the CNR vs the field size ranging from $5 \times 20 \text{ cm}^2$ to $45 \times 20 \text{ cm}^2$. In general, the contrast between the central rod and the background is similar (within 1.4%) for all field sizes but the CNR decreases with the field size.

Figure 14 shows the half-scan CBCT reconstructions using projection images of (a) one big panel and (b) three panoramic views with added Poisson noise from both primary and scatter signals. The scatter-to-primary ratios used to determine the amount of added Poisson noise were 0.99

for (a) and 0.58 for (b), calculated using the Monte Carlo simulations. The CNR was 4.1 for (a) and 6.25 for (b) in comparison to 11.5 [Fig. 5(b)] and 11.0 [Fig. 5(c)], respectively, when Poisson noise from the scattering event was not included.

IV. DISCUSSION

It is well known that the full-fan, half-scan CBCT using the FDK algorithm suffers more severe cone-beam artifacts than the full-fan, full-scan CBCT for slices away from the central slice due to increased missing data.²⁹ This phenomenon (reduced images quality for the half-scan CBCT), however, was not observed in this study. As shown in Fig. 5 and Table I, CBCT reconstructions are virtually identical for one big panel/full scan [Fig. 5(a)] and one big panel/half [Fig. 5(b)] and the image quality is similar, which we believe is due to the use of the SART instead of the FDK algorithm for reconstruction. These results are also consistent with the earlier report by Maaß *et al.*, who demonstrated that the SART has less cone-beam artifacts than the FDK algorithm.³³

The fact that the half-scan panoramic CBCT can produce virtually equivalent image quality as the full-fan, full-scan CBCT using one large imaging panel (Fig. 5 and Table I) has very significant clinical implications. First, since the half scan can be performed for most tumor locations and patient sizes without a gantry collision with the couch, patients with peripheral lesions can be imaged at the treatment position instead of being shifted to the central couch position to avoid collisions. Second, because the reconstruction volume of panoramic CBCT can be as large as practically needed, the reconstruction artifacts due to truncation are eliminated, leading to more accurate CT numbers. Finally, the accuracy of IGRT is expected to improve with the panoramic CBCT as a larger imaging volume can encompass more anatomic landmarks/critical organs to provide more accurate anatomic information for image guidance.

Results in Figs. 5–7 also demonstrate that the modified SART is as effective as the standard SART for CBCT reconstruction. The modified SART is essentially the standard SART except that it directly processes the projection data of each view for reconstruction. Data rebinning is necessary for reconstruction using the standard SART for cone beam geometry. Although such operation is mathematically simple, it poses a challenge for digital images as real image data do not exist between pixels and complex image processing is required to interpolate the existing image data. Imperfect rebinning also results in blurred images and degrades the geometric accuracy. The modified SART eliminates these reconstruction artifacts and saves the time for rebinning.

As demonstrated in Figs. 9–11 and Table I, imperfect image stitching is a major source of reconstruction artifacts for the panoramic CBCT, which lead to degraded CNR and/or geometric distortion. A gap between adjacent views can occur when the projection images are not properly captured at the edge of the imaging panel or when there are no detectors at the intersection between two adjacent views. Although the existence of gaps between adjacent views does

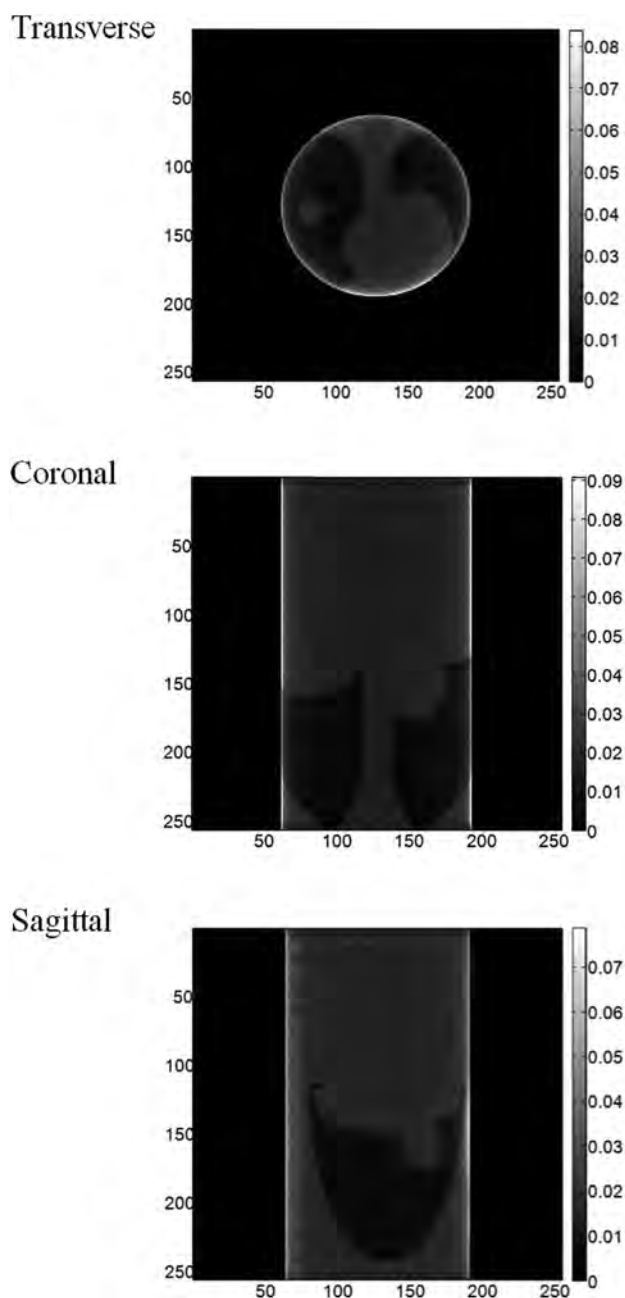


FIG. 8. The transverse, coronal, and sagittal slices for full-fan, half-scan (200° gantry rotation) CBCT reconstructions using the projection images of the central view only. Standard SART was used for the reconstruction.

not affect the geometric accuracy (Table I), it produces streak and line artifacts (Fig. 9) and degrades CNR with increasing gap size (Table I). These artifacts can be avoided by overlapping the imaging areas of adjacent views so that image intensity around the intersection can be properly interpolated.

Columns missing or repeating might occur in direct image stitching when the reported imaging position differs from the exact one due to sagging. As shown in Figs. 10 and 11 and Table I, in addition to streak and line artifacts, this type of imperfect stitching also degrades CNR and introduces geometric distortions. Columns missing or repeating can be corrected using a lookup table if the sagging of the imaging panel is reproducible. Alternatively, software correction can be used. For example, we are investigating the image stitching algorithms already developed in computer vision for panoramic photography, which uses rotational motion modeling and feature-based methods to calculate the overlap between a

pair of images.^{41,42} Algorithms can also be developed to correct the ring and line artifacts due to exposure fluctuations (Fig. 12). We plan to address the exposure fluctuations with a dynamic programming formulation⁴³ or more robustly using the Markov random field (MRF) approach.^{44,45}

With the large stitched projection data set, we are also limited by the computational burden of the iterative nature of SART reconstruction algorithm. The use of CBCT for image-guided radiotherapy requires real-time reconstruction so that, prior to the radiation treatment, patient positioning can be verified by comparing daily CBCT with the reference CT from treatment planning and simulation. However, a typical SART reconstruction for the test cases in this study takes ~ 8 h to complete using the conventional single-thread CPU-based processing. Since the CBCT reconstruction algorithms involve multiple forward projections of the intermediate estimates and backprojections of the projection image data, most of the time-consuming part of SART reconstruction

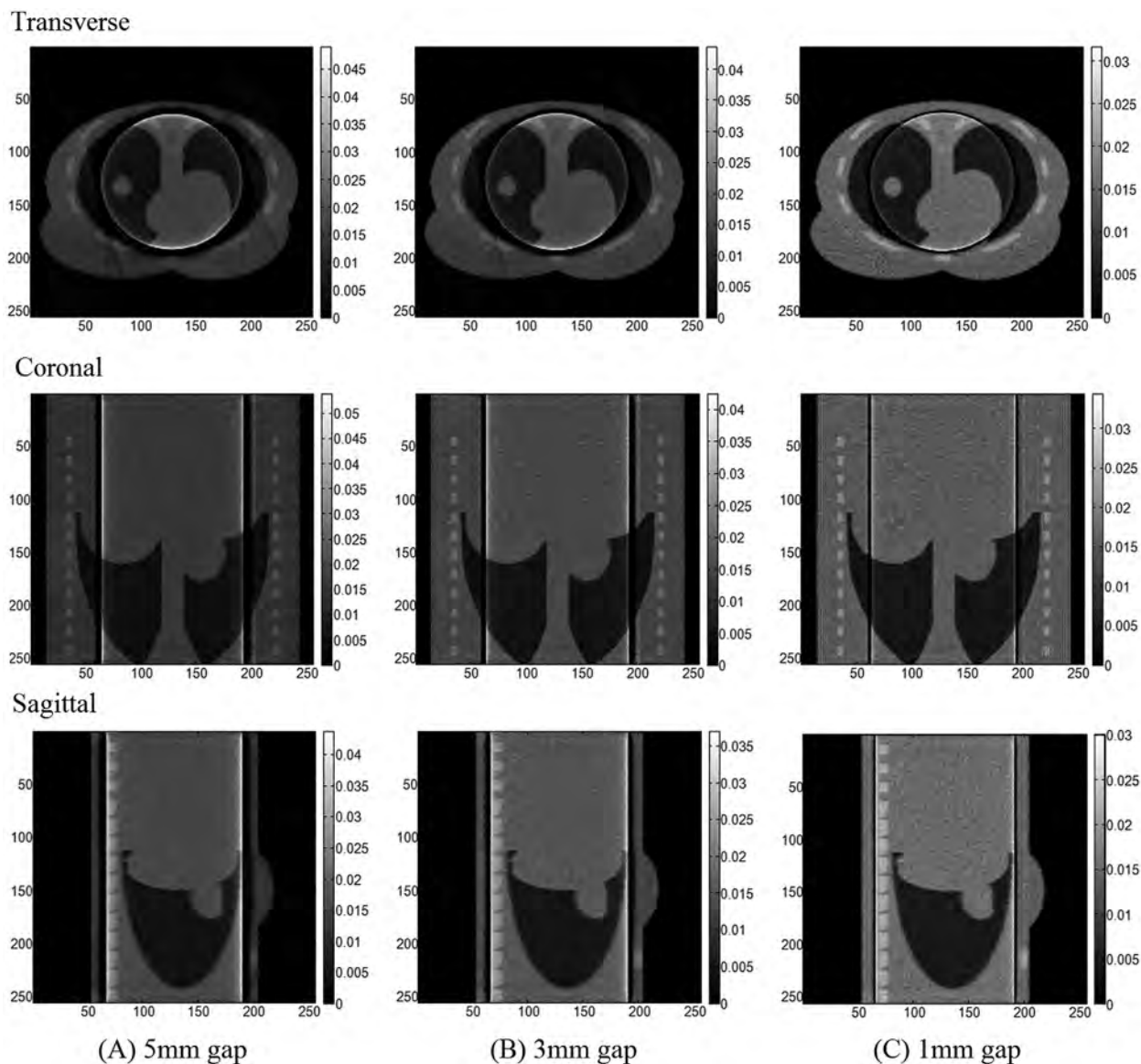


FIG. 9. Transverse, coronal, and sagittal slices of half-scan 3-view panoramic CBCT showing reconstruction artifacts due to imperfect stitching simulated by introducing (a) 5 mm, (b) 3 mm, and (c) 1 mm gaps between adjacent views.

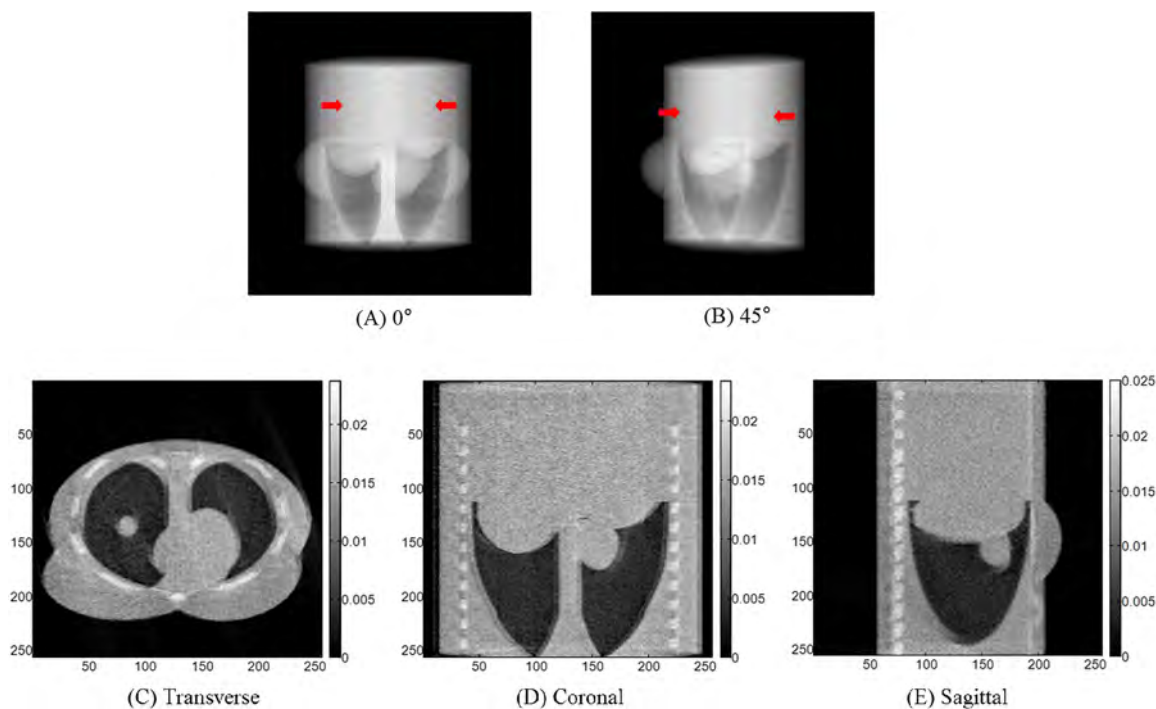


FIG. 10. Equivalent projection images of the three panoramic views for (a) 0° and (b) 45° gantry angles with three consecutive columns of pixels removed at the intersection between two adjacent (arrows) views. Half-scan panoramic CBCT reconstruction is also shown for one (c) transverse, (d) coronal, and (e) sagittal slices.

can be processed in parallel. We are currently investigating the acceleration of the modified SART using OpenCL (Open Computing Language) and general-purpose graphics processing unit (GPU) board. Our preliminary test shows that the GPU implementation of the forward-projection operation is

about 100 times faster than the CPU implementation. We will further improve the reconstruction speed by enhancing the algorithm to exhibit data locality and are confident that the reconstruction speed will eventually be comparable to that of the current CBCT in clinical use.

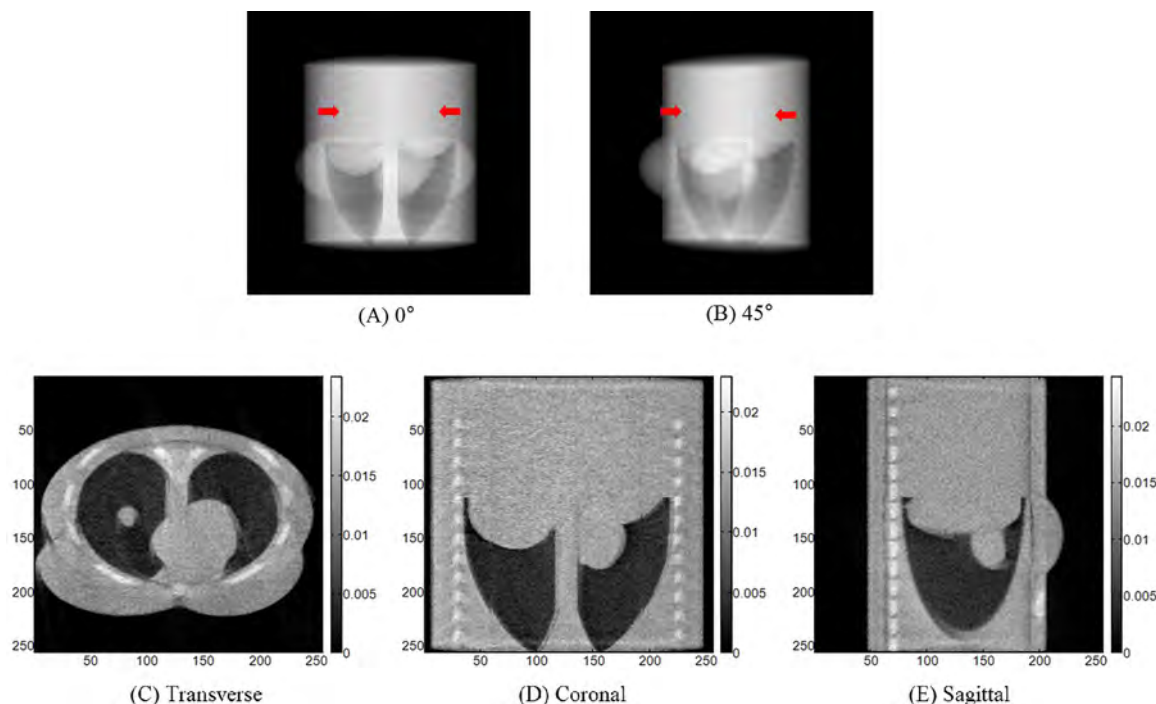


FIG. 11. Equivalent projection images of the three panoramic views for (a) 0° and (b) 45° gantry angles with three consecutive columns of pixels repeated at the intersection between two adjacent views (arrows). Half-scan panoramic CBCT reconstruction is also shown for one (c) transverse, (d) coronal and (e) sagittal slices.

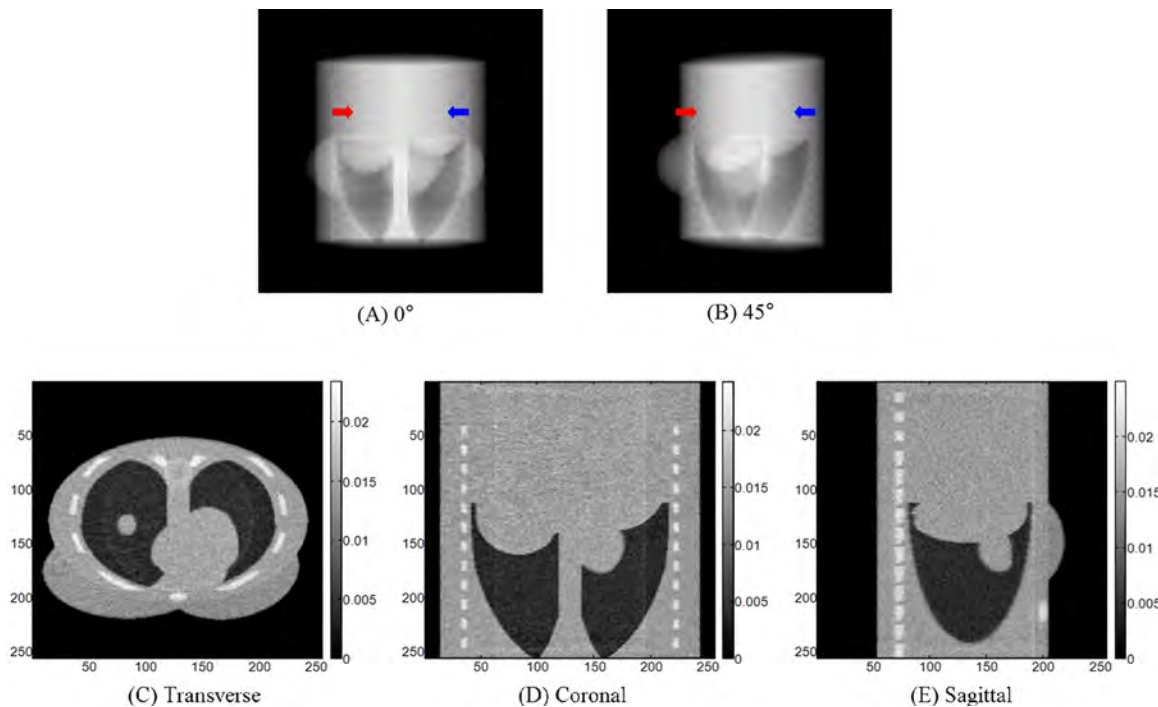


FIG. 12. Equivalent projection images of the three panoramic views for (a) 0° and (b) 45° gantry angles with the image intensity of the left and right views increases by 5% and 3%, respectively. Arrows indicate the intersection between two adjacent views. Half-scan panoramic CBCT reconstruction is also shown for one (c) transverse, (d) coronal, and (e) sagittal slices.

TABLE I. CNR and geometry accuracy for the reconstructed images in Figs. 5 and 8–12. CNR is calculated for the simulated lung tumor (circled in dotted line) in the upper right panel. Two distances were calculated. “D1” is the distance of two selected ribs in the corona view (upper left panel) and “D2” in the transverse view (upper right panel).

| | CNR | D1 (voxels) | D2 (voxels) |
|--|------|-------------|-------------|
| Full scan [Fig. 5(a)] | 11.2 | 188 | 186 |
| Half scan [One big panel, Fig. 5(b)] | 11.5 | 188 | 186 |
| Half scan [Three panoramic views, Fig. 5(c)] | 11.0 | 188 | 186 |
| 1 mm gap [Fig. 9(c)] | 11.0 | 188 | 186 |
| 3 mm gap [Fig. 9(b)] | 10.4 | 188 | 186 |
| 5 mm gap [Fig. 9(a)] | 9.4 | 188 | 186 |
| Exposure fluctuations (Fig. 12) | 11.3 | 188 | 186 |
| Removed three columns (Fig. 10) | 9.9 | 185 | 183 |
| Repeated three columns (Fig. 11) | 9.9 | 197 | 195 |
| Central panel only (Fig. 8) | 6.4 | N/A | N/A |

By visual inspection of Figs. 13(a) and 13(b), the projection image for the $45 \times 20 \text{ cm}^2$ field size is noisier than that for the $5 \times 20 \text{ cm}^2$ field size. This difference can be explained by the fact that the primary signals of both profiles in Fig. 13(c) are comparable but the total signal of the $45 \times 20 \text{ cm}^2$ field is much larger than that of the $5 \times 20 \text{ cm}^2$ field, indicating a much higher scattering signal for the $45 \times 20 \text{ cm}^2$ field. Since the scattering signal only increases the noise but contrast, the CNR is therefore lower for the $45 \times 20 \text{ cm}^2$ field. The same explanation applies to the results in Fig. 13(d) that the CNR decreases with the field size. Since the same number of photons was used in the Monte Carlo simulation for each field size, results in Fig. 13(d) indicates that, for the same mAs, the image quality is better for the smaller field size. Better image quality for projection images also leads to better image quality for CBCT reconstruction of the MCAT phantom. As shown in Fig. 14, for the same imaging volume and dose, there is a 50% improvement when using three panoramic views ($\text{CNR} = 6.25$) over using one big panel ($\text{CNR} = 4.1$). Therefore, the image quality of the panoramic CBCT is better than that acquired with an equivalent imaging panel for the same imaging volume and same mAs. On the other hand, if the same image quality is required, the panoramic CBCT requires a lower mAs than using the equivalent imaging panel.

In addition to image quality, imaging dose and imaging time are two other major concerns for IGRT using CBCT. In theory, for the same mAs, the imaging dose of panoramic CBCT is the same as using the equivalent imaging panel, assuming the leakage dose is negligible and there are no overlaps between the adjacent views. As discussed earlier,

overlap between adjacent views is necessary to minimize the artifacts due to discontinuity or a gap around the intersection. Assuming the percent increase in the imaging dose is the fraction of imaging width overlapped with the adjacent imaging panel, a two-view panoramic CBCT with an imaging width of 20 cm and an overlap of 0.5 cm increases the imaging dose by $\sim 5\%$ ($2 \times 0.5/20$). From Fig. 13(d), the CNR for $20 \times 20 \text{ cm}^2$ is ~ 3.4 while the CNR for a $40 \times 20 \text{ cm}^2$ is ~ 2.8 , indicating that the two-view panoramic CBCT can achieve the same image quality with $\sim 32\%$ less mAs or a reduction of the imaging dose by $\sim 32\%$. Therefore, the increased imaging dose due to overlap can be easily offset by the gain in image quality.

The leakage limitation for a kV x-ray source is 1 mGy/h (or 0.017 mGy/min) at 1 m from the source. The sources typically operate in pulsed mode at 100 to 125 kV and up to 90 mA and 25 ms per pulse depending on the anatomical position of the treatment site. Therefore, most CBCT scans are acquired with a beam-on-time on the order of 15 s (assuming 600 projections and 25 ms/projection) or less and the leakage dose is less than 0.1% of the imaging dose (on the order of

10–20 mGy per scan) of a typical CBCT scan. The additional leakage dose due to the panoramic CBCT is therefore negligible since, in most cases, three-view panoramic CBCT is clinically sufficient, which will increase the imaging dose by no more than 0.2%. Consequently, for the same image quality, the imaging dose of panoramic CBCT is lower than the standard CBCT using an equivalent imaging panel for the same imaging volume.

In comparison to the standard half-fan, full-scan CBCT, a two-view panoramic CBCT pays a slight price in imaging dose ($\sim 11\%$ higher, 400° vs 360° rotation assuming the same overlap) to avoid a collision. A three-view CBCT gives additional imaging dose to the region outside the imaging volume of the standard CBCT, which is irradiated but not imaged, not to save the imaging dose but due to the limited size of the imaging panel. The additional dose for panoramic CBCT is therefore necessary to fulfill what is intended but not achieved by the half-fan, full-scan CBCT.

Although the panoramic CBCT has better image quality and comparable imaging dose, its use might not be justified unless the imaging time is similar to or less than that of

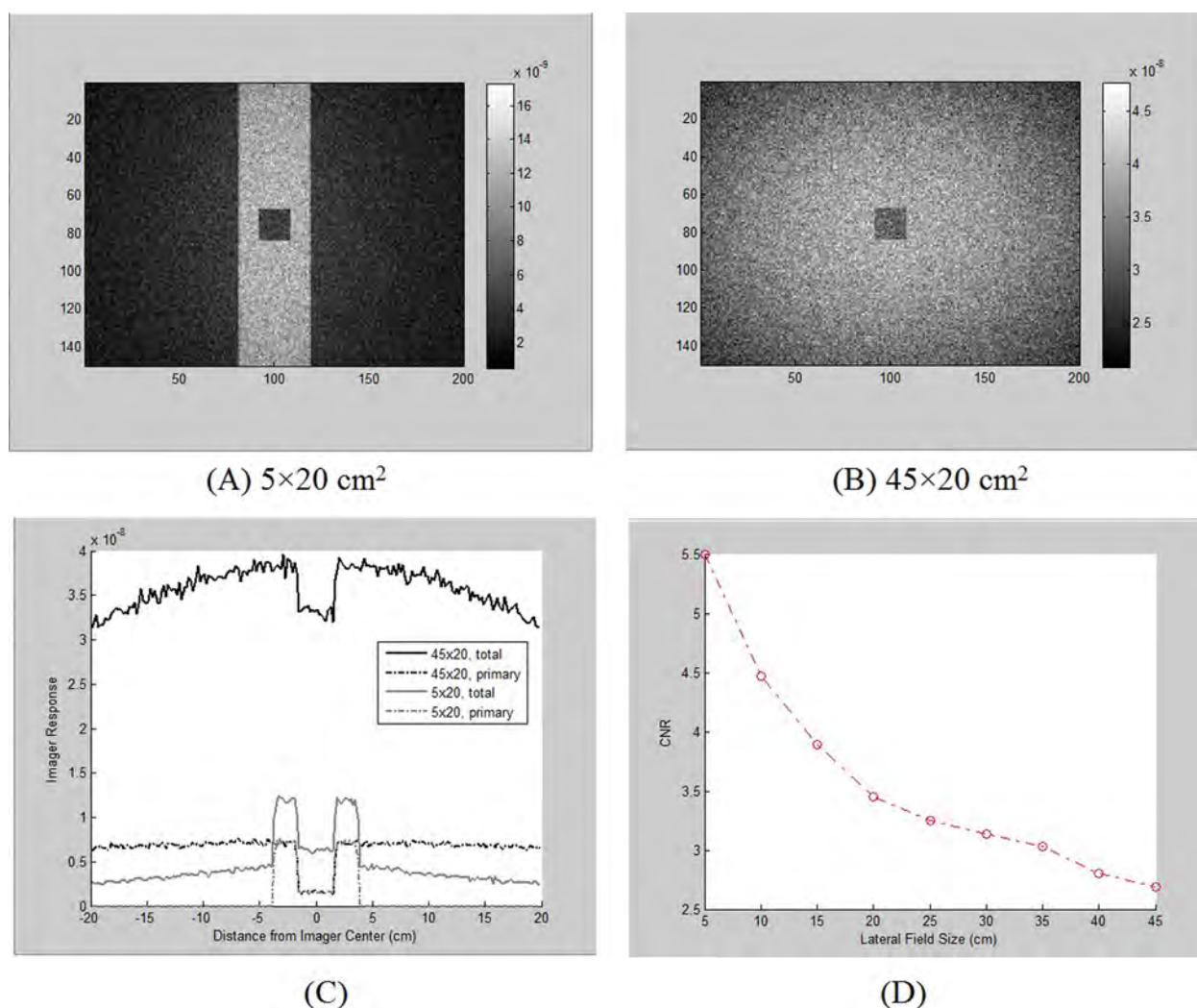


FIG. 13. Simulated projection images for (a) 5×20 and (b) $45 \times 20 \text{ cm}^2$ fields, respectively. Panel (c) shows the central profiles of the total signal and primary signal of both fields and panel (d) is the contrast-to-noise ratio vs the field size.

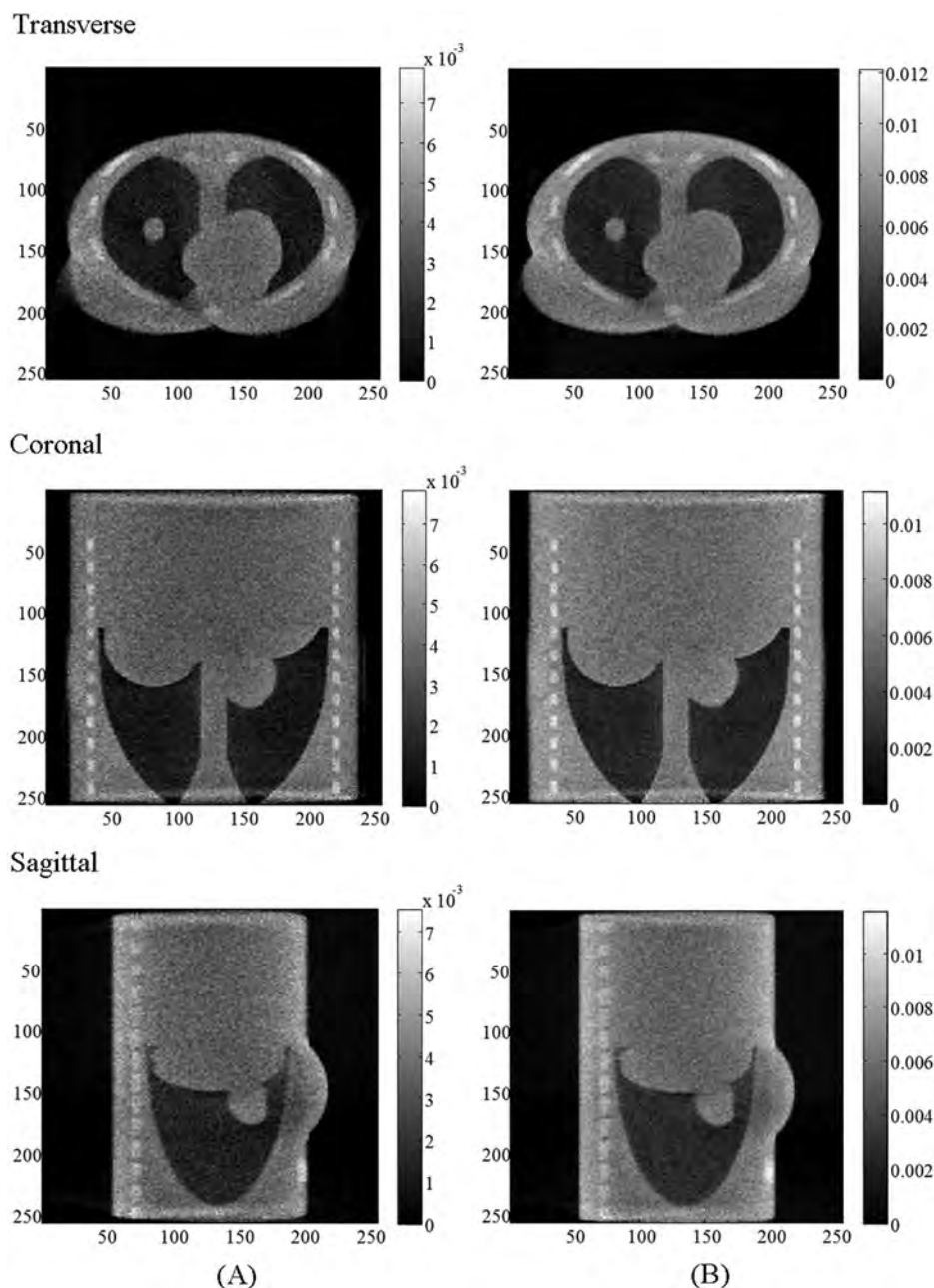


FIG. 14. Half-scan CBCT reconstructions of the MCAT phantom using projection images for (a) one big panel and (b) three panoramic views with added Poisson noise from both primary and scattering signals. The amount of added Poisson noise was determined according to the scatter-to-primary ratio of each scanning geometry calculated using the Monte Carlo simulations. The CNR for the simulated lung tumor is 4.1 for (a) and 6.25 for (b).

standard CBCT. Since the panoramic CBCT requires at least two repeated half rotations, it will not replace the full-fan, half-scan CBCT for small targets as well as the half-fan, full-scan CBCT for larger targets that does not cause collisions. However, the panoramic CBCT has an advantage in scanning time over the standard CBCT for peripheral lesions that require couch shift so that the half-fan, full-scan CBCT can be performed without collision. Assuming one full scan takes a minute, two half scans (400° rotation) takes about an additional 7 s for image acquisition than one full scan (360° rotation). However, the half-fan, full scan CBCT needs an additional 20–30 s to rotate the gantry to the starting position (180°) than the panoramic CBCT (starting between 270° and

90°). The half-fan, full scan CBCT also needs additional time to shift the couch to the central position before imaging (to avoid a collision) and back to the treatment position after the CBCT acquisition. The additional time for couch shift might take a few minutes if done manually and can be reduced to less than a half minute if performed automatically. However, an automatic couch movement on the order of 5 cm or more within a short time might cause some patient discomfort. Acceleration and deceleration of the couch movement might also produce unexpected patient motions that are difficult to detect. As a result, in either (manual or automatic movement) case, additional QA is needed after CBCT acquisition to confirm that the couch and

patient are returned to the original position so that the corrections from the CBCT can be properly applied. All these additional uncertainties and QA can be eliminated with the panoramic CBCT that can image the patient at the treatment position.

The panoramic CBCT is definitely a better option if the target is too large to be fully covered by the half-fan, full-scan CBCT. Although truncated images are still useful, important anatomic features might be lost or be compromised by reconstruction artifacts. With the panoramic CBCT, we can acquire the tomographic images of the whole target in the transverse direction, which contains more accurate anatomic information for image guidance and possibly for real-time re-planning.

V. CONCLUSIONS

Although the half-fan, full-scan CBCT addresses the need for the majority of the IGRT cases, there is always room for improvement. In this study, we developed a novel panoramic CBCT technique to complement the half-fan, full-scan CBCT and improve the efficiency and image quality of CBCT for certain IGRT applications. We demonstrated that the panoramic CBCT technique can significantly increase the imaging volumes by stitching together the projection images of multiple half scans, each with a different view angle. Since the half scan can be achieved for most treatment positions without couch collisions, the panoramic CBCT can image tumors at any location for a patient of any size at the treatment position without having to move the patient to the central location. The capability to include the whole patient anatomy in the scan also allows for the real-time dose calculation and replanning. The panoramic CBCT also has less scattering noise and therefore better image quality than the half-fan, full-scan CBCT. However, the image quality of panoramic CBCT might be compromised by imperfect image stitching that is difficult to detect and correct with the direct image stitching method. Better image stitching algorithms are therefore needed to improve the accuracy of image stitching.

ACKNOWLEDGMENTS

Part of this work was presented at the 2011 Joint AAPM/COMP Annual Meeting, July 31–August 4, Vancouver, Canada. This work was partially supported by a DOD Grant No. DOD W81XWH1010862.

^{a)}Author to whom correspondence should be addressed. Electronic mail: jec2046@med.cornell.edu; Telephone: (212) 746-6305; Fax: (212) 746-8850.

¹R. I. Berbeco, S. B. Jiang, G. C. Sharp, G. T. Y. Chen, H. Mostafavi, and H. Shirato, "Integrated radiotherapy imaging system (IRIS): Design considerations of tumour tracking with linac gantry-mounted diagnostic x-ray systems with flat-panel detectors," *Phys. Med. Biol.* **49**, 243–255 (2004).

²G. X. Ding, D. M. Duggan, C. W. Coffey, M. Deeley, D. E. Hallahan, A. Cmelak, and A. Malcolm, "A study on adaptive IMRT treatment planning using kV cone-beam CT," *Radiother. Oncol.* **85**, 116–125 (2007).

³M. Leordeanu and M. Hebert, "A spectral technique for correspondence problems using pairwise constraints," in *Tenth IEEE International Conference on Computer Vision, 2005, ICCV* (IEEE, New York, 2005), Vol. 2, pp. 1482–1489.

- ⁴T. R. Mackie, J. Kapatoes, K. Ruchala, W. Lu, C. Wu, G. Olivera, L. Forrest, W. Tome, J. Welsh, R. Jeraj, P. Harari, P. Reckwerdt, B. Paliwal, M. Ritter, H. Keller, J. Fowler, and M. Mehta, "Image guidance for precise conformal radiotherapy," *Int. J. Radiat. Oncol., Biol., Phys.* **56**, 89–105 (2003).
- ⁵R. Mohan, X. Zhang, H. Wang, Y. Kang, X. Wang, H. Liu, K. K. Ang, D. Kuban, and L. Dong, "Use of deformed intensity distributions for on-line modification of image-guided IMRT to account for interfractional anatomic changes," *Int. J. Radiat. Oncol., Biol., Phys.* **61**, 1258–1266 (2005).
- ⁶L. Xing, B. Thorndyke, E. Schreiber, Y. Yang, T.-F. Li, G.-Y. Kim, G. Luxton, and A. Koong, "Overview of image-guided radiation therapy," *Med. Dosim.* **31**, 91–112 (2006).
- ⁷Y. Cho, D. J. Moseley, J. H. Siewerdsen, and D. A. Jaffray, "Accurate technique for complete geometric calibration of cone-beam computed tomography systems," *Med. Phys.* **32**, 968–983 (2005).
- ⁸B. A. Groh, J. H. Siewerdsen, D. G. Drake, J. W. Wong, and D. A. Jaffray, "A performance comparison of flat-panel imager-based MV and kV cone-beam CT," *Med. Phys.* **29**, 967–975 (2002).
- ⁹D. A. Jaffray and J. H. Siewerdsen, "Cone-beam computed tomography with a flat-panel imager: Initial performance characterization," *Med. Phys.* **27**, 1311–1323 (2000).
- ¹⁰D. A. Jaffray, J. H. Siewerdsen, J. W. Wong, and A. A. Martinez, "Flat-panel cone-beam computed tomography for image-guided radiation therapy," *Int. J. Radiat. Oncol., Biol., Phys.* **53**, 1337–1349 (2002).
- ¹¹D. Létourneau, J. W. Wong, M. Oldham, M. Gulam, L. Watt, D. A. Jaffray, J. H. Siewerdsen, and A. A. Martinez, "Cone-beam-CT guided radiation therapy: Technical implementation," *Radiother. Oncol.* **75**, 279–286 (2005).
- ¹²M. Oldham, D. Létourneau, L. Watt, G. Hugo, D. Yan, D. Lockman, L. H. Kim, P. Y. Chen, A. Martinez, and J. W. Wong, "Cone-beam-CT guided radiation therapy: A model for on-line application," *Radiother. Oncol.* **75**, 271.E271–271.E278 (2005).
- ¹³M. B. Sharpe, D. J. Moseley, T. G. Purdie, M. Islam, J. H. Siewerdsen, and D. A. Jaffray, "The stability of mechanical calibration for a kV cone beam computed tomography system integrated with linear accelerator," *Med. Phys.* **33**, 136–144 (2006).
- ¹⁴J. H. Siewerdsen and D. A. Jaffray, "Cone-beam computed tomography with a flat-panel imager: Effects of image lag," *Med. Phys.* **26**, 2635–2647 (1999).
- ¹⁵J. H. Siewerdsen and D. A. Jaffray, "Optimization of x-ray imaging geometry (with specific application to flat-panel cone-beam computed tomography)," *Med. Phys.* **27**, 1903–1914 (2000).
- ¹⁶J. H. Siewerdsen, D. J. Moseley, B. Bakhtiar, S. Richard, and D. A. Jaffray, "The influence of antiscatter grids on soft-tissue detectability in cone-beam computed tomography with flat-panel detectors," *Med. Phys.* **31**, 3506–3520 (2004).
- ¹⁷M. H. P. Smitsmans, J. de Bois, J.-J. Sonke, A. Betgen, L. J. Zijp, D. A. Jaffray, J. V. Lebesque, and M. van Herk, "Automatic prostate localization on cone-beam CT scans for high precision image-guided radiotherapy," *Int. J. Radiat. Oncol., Biol., Phys.* **63**, 975–984 (2005).
- ¹⁸J. R. Sykes, A. Amer, J. Czajka, and C. J. Moore, "A feasibility study for image guided radiotherapy using low dose, high speed, cone beam X-ray volumetric imaging," *Radiother. Oncol.* **77**, 45–52 (2005).
- ¹⁹J. Hsieh, E. Chao, J. Thibault, B. Grekowitz, A. Horst, S. McOlash, and T. J. Myers, "Algorithm to extend reconstruction field-of-view," in *IEEE International Symposium on Biomedical Imaging: Nano to Macro, 2004* (IEEE, New York, 2004), Vol. 1402, pp. 1404–1407.
- ²⁰A. A. Zamyatin and S. Nakanishi, "Extension of the reconstruction field of view and truncation correction using sinogram decomposition," *Med. Phys.* **34**, 1593–1604 (2007).
- ²¹M. J. Murphy, "The importance of computed tomography slice thickness in radiographic patient positioning for radiosurgery," *Med. Phys.* **26**, 171–175 (1999).
- ²²L. A. Feldkamp, L. C. Davis, and J. W. Kress, "Practical cone-beam algorithm," *J. Opt. Soc. Am. A* **1**, 612–619 (1984).
- ²³C. Maaß, M. Knaup, R. Lapp, M. Karolczak, W. A. Kalender, and M. Kachelrieß, "A new weighting function to achieve high temporal resolution in circular cone-beam CT with shifted detectors," *Med. Phys.* **35**, 5898–5909 (2008).
- ²⁴G. Wang, "X-ray micro-CT with a displaced detector array," *Med. Phys.* **29**, 1634–1636 (2002).
- ²⁵D. L. Parker, "Optimal short scan convolution reconstruction for fan beam CT," *Med. Phys.* **9**, 254–257 (1982).

- ²⁶L. Chen, C. C. Shaw, C.-J. Lai, M. C. Altunbas, T. Wang, S.-J. Tu, and X. Liu, "Comparison of full-scan and half-scan for cone beam breast CT imaging," in *Proceedings of SPIE 6124 Medical Imaging 2006: Physics of Medical Imaging Vol. 6142*, edited by M. J. Flynn and J. Hsieh (SPIE, San Diego, CA, 2006), pp. 61424M.
- ²⁷Y. Liu, H. Liu, Y. Wang, and G. Wang, "Half-scan cone-beam CT fluoroscopy with multiple x-ray sources," *Med. Phys.* **28**, 1466–1471 (2001).
- ²⁸H. K. Tuy, "Inversion formula for cone-beam reconstruction," *SIAM J. Appl. Math.* **43**, 546–552 (1983).
- ²⁹K. Taguchi, "Temporal resolution and the evaluation of candidate algorithms for four-dimensional CT," *Med. Phys.* **30**, 640–650 (2003).
- ³⁰K. Mueller, *Fast and Accurate Three-Dimensional Reconstruction From Cone-Beam Projection Data Using Algebraic Methods* (The Ohio State University, Ohio, 1998).
- ³¹H. Guan and R. Gordon, "Computed tomography using algebraic reconstruction techniques (ARTs) with different projection access schemes: A comparison study under practical situations," *Phys. Med. Biol.* **41**, 1727–1743 (1996).
- ³²W. Ge, G. Schweiger and M. W. Vannier, "An iterative algorithm for X-ray CT fluoroscopy," *IEEE Trans. Med. Imaging* **17**, 853–856 (1998).
- ³³C. Maaß, F. Dennerlein, F. Noo, and M. Kachelrieß, Presented at the Nuclear Science Symposium Conference Record (NSS/MIC), 2010 IEEE, 2010 (unpublished).
- ³⁴F. Noo, C. Bernard, F. X. Litt, and P. Marchot, "A comparison between filtered backprojection algorithm and direct algebraic method in fan beam CT," *Signal Process.* **51**, 191–199 (1996).
- ³⁵M. W. D. Grattan and C. K. McGarry, "Mechanical characterization of the Varian Exact-arm and R-arm support systems for eight aS500 electronic portal imaging devices," *Med. Phys.* **37**, 1707–1713 (2010).
- ³⁶K. Mueller and R. Yagel, "Rapid 3-D cone-beam reconstruction with the simultaneous algebraic reconstruction technique (SART) using 2-D texture mapping hardware," *IEEE Trans. Med. Imaging* **19**, 1227–1237 (2000).
- ³⁷W. P. Segars, D. S. Lalush, and B. M. W. Tsui, "Modeling respiratory mechanics in the MCAT and spline-based MCAT phantoms," *IEEE Trans. Nucl. Sci.* **48**, 89–97 (2001).
- ³⁸R. L. Siddon, "Fast calculation of the exact radiological path for a three-dimensional CT array," *Med. Phys.* **12**, 252–255 (1985).
- ³⁹E. Mainegra-Hing and I. Kawrakow, "Variance reduction techniques for fast Monte Carlo CBCT scatter correction calculations," *Phys. Med. Biol.* **55**, 4495–4507 (2010).
- ⁴⁰E. Mainegra-Hing and I. Kawrakow, "Fast Monte Carlo calculation of scatter corrections for CBCT images," *J. Phys.: Conf. Ser.* **102**, 012017 (2008).
- ⁴¹M. Brown and D. Lowe, "Automatic panoramic image stitching using invariant features," *Int. J. Comput. Vis.* **74**, 59–73 (2007).
- ⁴²H.-Y. Shum and R. Szeliski, "Systems and experiment paper: Construction of panoramic image mosaics with global and local alignment," *Int. J. Comput. Vis.* **36**, 101–130 (2000).
- ⁴³A. A. Efros and W. T. Freeman, "Image quilting for texture synthesis and transfer," in *Proceedings of the 28th Annual Conference on Computer Graphics and Interactive Techniques* (ACM, Los Angeles, CA, 2001), pp. 341–346.
- ⁴⁴Y. Boykov, O. Veksler, and R. Zabih, "Fast approximate energy minimization via graph cuts," *IEEE Trans. Pattern Anal. Mach. Intell.* **23**, 1222–1239 (2001).
- ⁴⁵R. Szeliski, R. Zabih, D. Scharstein, O. Veksler, V. Kolmogorov, A. Agarwala, M. Tappen, and C. Rother, "A comparative study of energy minimization methods for Markov random fields with smoothness-based priors," *IEEE Trans. Pattern Anal. Mach. Intell.* **30**, 1068–1080 (2008).

Fast Poly-energetic Forward Projection for Image Formation Using OpenCL on a Heterogeneous Parallel Computing Platform

Lili Zhou, Ph.D.¹, K. S. Clifford Chao, M.D.^{1,2,3} and Jenghwa Chang, Ph.D.^{1,2}

5 ¹Radiation Oncology, Weill Cornell Medical College, Cornell University, New York, NY

² Radiation Oncology, NewYork-Presbyterian Hospital, New York, NY

³ Radiation Oncology, College of Physicians and Surgeons, Columbia University, New York, NY

Abstract

Purpose: Simulated projection images of digital phantoms constructed from CT scans have been widely used for clinical and research applications but their quality and computation speed are not optimal for real-time comparison with the radiography acquired with an x-ray source of different energies. In this paper, we performed poly-energetic forward projections using Open Computing Language (OpenCL) in a parallel computing ecosystem consisting of CPU and GPGPU (general purpose graphics processing unit) for fast and realistic image formation.

Methods: The proposed poly-energetic forward projection uses a lookup table containing the NIST published mass attenuation coefficients (μ/ρ) for different tissue types and photon energies ranging from 1keV to 20MeV. The CT images of interested sites are first segmented into different tissue types based on the CT numbers, and converted to a three-dimensional attenuation phantom by linking each voxel to the corresponding tissue type in the lookup table. The x-ray source can be a radioisotope or an x-ray generator with a known spectrum described as weight $w(n)$ for energy bin $E(n)$. The Siddon's method is used to compute the x-ray transmission line integral for $E(n)$ and the x-ray fluence is the weighted sum of the exponential of line integral for all energy bins with added Poisson noise. To validate this method, a digital head and neck phantom constructed from the CT scan of a Rando head phantom was segmented into three (air, grey/white matter and bone) regions for calculating the poly-energetic projection images for the Mohan 4MV energy spectrum. To accelerate the calculation we partitioned the workloads using the task parallelism (TP) and data parallelism (DP) and scheduled them in a parallel computing ecosystem consisting of CPU and GPGPU (NVIDIA Tesla C2050) using OpenCL *only*. We explored the task overlapping strategy and the sequential method for generating the first and subsequent DRRs. A dispatcher was designed to drive the high-degree parallelism of the task

overlapping strategy. Numerical experiments were conducted to compare the performance of the

35 OpenCL/GPGPU-based implementation with the CPU-based implementation.

Results: The projection images were similar to typical portal images obtained with **a** 4 or 6 MV x-ray source. For a phantom size of $512 \times 512 \times 223$, the time for calculating the line integrals for a 512×512 image panel was 16.2 ms on GPGPU for one energy bin in comparison to 8.83 s on CPU. The total computation time for generating one poly-energetic projection image of $512 \times$
40 512 was 0.3 s (141s for CPU). The relative difference between the projection images obtained with the CPU-based and OpenCL/GPGPU-based implementations was on the order of 10^{-6} and **was** virtually indistinguishable. **The task overlapping strategy was 5.84 and 1.16 times faster than the sequential method for the first and the subsequent DRRs, respectively.**

Conclusions: We have successfully built digital phantoms using anatomic CT images and NIST
45 μ/ρ tables **s** for simulating realistic poly-energetic projection images and optimized the processing speed with parallel computing using GPGPU/OpenCL-based implementation. The computation time was fast (0.3 s per projection image) enough for real time IGRT (image-guided radiotherapy) applications.

1 Introduction

50 The phantom study is an essential step before applying a new imaging technology for clinical use in diagnostic radiology and radiation therapy. Both physical and digital phantoms have been used for developing and testing imaging software/systems. Building a physical phantom and acquiring the test data are usually expensive and time consuming. A digital phantom, on the other hand, is flexible in adjusting the phantom and imaging parameters, does not require a physical presence
55 in the imaging/treatment room and is cost effective.

Several digital phantoms mimicking the internal organs of the human body [1-10] have been developed over decades in order to estimate the dose distribution in human organs from internal or external radioactive sources or to evaluate the performance of imaging devices, reconstruction methods and registration techniques. These phantoms can be mathematically created from
60 analytical equations, e.g., the Shepp-Logan phantom for CT/CBCT (Cone-Beam CT) reconstruction. Analytically defined phantoms allow for variable anatomical properties (e.g. surface information and volume) and different resolutions but lack the ability to simulate complex anatomical structures and realistic organ shapes. Alternatively, a digital phantom can be numerically reconstructed by deriving the desired tissue properties of each voxel in the phantom
65 from the image intensity of corresponding voxels in volumetric CT images. The advantage of the digitally reconstructed phantom is that it originates from true patient data and is therefore more realistic than the analytic and physical phantoms. However, construction of a phantom of this type requires interpolations of digital data from CT/MR images with different resolutions [10], which is prone to truncation and round off errors.

70 One major application of the digital phantom is to produce digitally reconstruction radiographies (DRR) for research/development purposes or clinical use. For example, projection images for a

gantry rotation of 360 degree or 180 + cone angle can be generated from a digital phantom to test CBCT reconstruction algorithms. DRR has also been generated from patient simulation CT scans to guide radiotherapy setup. Both 2D (two dimensional)/2D and 3D (three dimensional)/3D

75 image registrations have been used for IGRT. The 2D/2D matching registers pre-calculated DRRs with radiographs acquired in the treatment position. The 2D/3D matching, on the other hand, requires real-time iterative production and comparison of DRRs from the 3D simulation CT with radiograph until the best matching is achieved.

The success of these applications depends on (1) how close the digitally reconstructed projection
80 images are to the true images and (2) how fast they can be calculated. Both conditions are difficult to meet for a digitally reconstructed phantom from the CT images. First, tissue attenuation coefficient varies significantly with the x-ray energy so the projection images for a different x-ray source cannot be faithfully predicted using the reconstructed attenuation coefficients for the imaging source. In addition, rendering DRR images from 3D CT data set is
85 computationally expensive because a small voxel size (on the order of a few millimeters) is needed to approximate the true patient anatomy and ray tracing through the digital phantom might take a significant amount of time. As a result, DRR generation is considered a bottleneck for 2D/3D image registration and becomes prohibitive for some IGRT (Image Guided Radiation Therapy) techniques that require the calculation of the projection images in real time.

90 To address these limitations, we proposed to perform poly-energetic forward projection for the energy spectrum of the interested x-ray source (instead of the CT source) on digital phantoms constructed by segmenting the anatomical CT images into different tissue types and assigning each tissue type with the attenuation coefficients (μ/ρ) for different x-ray energies from the NIST μ/ρ table [11]. Although more realistic DRR can be obtained with this approach, inclusion of

multiple energy bins in the forward projection will increase the processing time in proportion, making it impractical for real-time 2D/3D image registration. Therefore, we also parallelized the image projection operations using a general purpose graphics processing unit (GPGPU) so that the projection images can be generated in real time for IGRT applications.

Parallel processing using different combinations of hardware and software has been explored by many groups [12-16] to accelerate the calculation of mono-energetic DRRs. GPGPU is a highly parallel computing graphic architecture with a high bandwidth memory bus, which is ideal for parallel processing of image projection using a poly-energetic source. In general, current GPU-accelerated applications for medical imaging employ two approaches: graphics-based and non-graphics based. The graphics-based approaches have been explored by many researchers [17-23] who used texture mapping and shading language with the aid of graphics libraries such as OpenGL or C for graphics (Cg). The introduction of NVIDIA's Compute Unified Device Architecture (CUDA) simplifies the programming GPU for general-purpose computing tasks. The CUDA-based method for accelerating image reconstruction was used in many prior studies [24-32]. It is still an open question whether the CUDA-based approach outperforms the graphics-based approach.

GPGPU programming originally required users to possess intimate knowledge of graphics APIs (*OpenGL* or *DirectX*) and GPU architecture and to make their non-graphics applications look like graphics ones by mapping them into problems that drew triangles and polygons. This placed a great constraint for non-graphics domain users.

Recently OpenCL (Open Computing Language) has emerged as a competitive interface for programming GPUs. OpenCL is an open industry standard for general purpose parallel programming across CPU, GPGPU, and other processors from different vendors, while CUDA is specific to NVIDIA GPUs. Although

OpenCL offers the portability across GPU hardware, **operation system** software and multicore processors, it may cause a performance penalty [33]. A review article for GPU computing in
120 medical physics was presented by Pratz et al [34].

In this paper, we shall first present the mathematical derivation of poly-energetic projection, followed by its implementation in a GPGPU/OpenCL-based parallel computing ecosystem. We shall describe how to use the OpenCL to (1) partition the workloads across CPU and GPGPU, (2) decompose them using task parallelism (TP) and data parallelism (DP), and (3) schedule
125 them to all available heterogeneous processors. The results of poly-energetic projections for a digital head and neck phantom from the CT scan of a Rando head phantom will be presented to demonstrate the feasibility of the proposed method. Finally, the overall performance and the clinical applications will be discussed.

2 Digital Phantom Construction and Poly-Energetic Image Projection

2.1 Index Phantom and Attenuation Phantom Formation

130

The 3D distribution of attenuation property **as a function of x-ray energy is required** for calculating the transmission attenuation along the path from the source to the detectors. To simplify the data structure, instead of assigning the attenuation property to each voxel, a **3D index** phantom that indexes each voxel to a tissue type was first constructed by segmenting the
135 CT images of the interested object (physical phantom or patient) into different tissue types based on the CT numbers. **A** 3D attenuation phantom was then formed by linking each tissue index to the **corresponding entry of the** lookup table **constructed from the NIST published data [11]** containing μ/ρ of different tissues for x-ray energies ranging from 1 keV to 20 MeV. When

simulating the photon attenuation, the linear attenuation coefficient was calculated as the product
140 of the interpolated μ/ρ and tissue density (ρ).

2.2 Projection Image Generation

We used the Siddon's ray-trace method [35] to calculate the x-ray transmission line integral through the attenuation phantom along the path from the x-ray source to the detector pixel m , $m = 1, \dots, M$, where M is the total number of the detector pixels. A line connecting the x-ray source
145 and the center of each detector pixel defines a ray that traverses voxels of the phantom. Without loss of generality, a 2D object as shown in Figure 1 is used to illustrate this ray-driven method. In Figure 1, the distance between two neighboring solid dots along a ray defines the chord length of the intersecting pixels (or voxels in 3D). Note that the number of intersecting pixels (or voxels) along each ray varies.

150 The x-ray source can be a radioisotope or an x-ray generator with known spectrum data consisting of the weight w_n for each energy bin E_n , $n = 1, \dots, N$, where N is the total number of energy bins. Table 1 illustrates one example of the energy spectrum table – Mohan4 energy spectrum for a 4MV linear accelerator. The line integral $g_m(E_n)$ at detector m for x-ray energy bin E_n can be expressed as

$$155 \quad g_m(E_n) = \sum_j \mu(j, E_n) a_m(j) \quad (1)$$

where $\mu(j, E_n)$ is the linear attenuation coefficient at voxel j for energy bin E_n and $a_m(j)$ is the chord length of the m th ray passing through the j th voxel calculated by Siddon's ray-trace method, and $j = 1, \dots, J$, J is the total number of voxels in the 3D attenuation phantom. The x-ray fluence $b_m(E_n)$ at detector m for energy bin E_n is given by

$$b_m(E_n) = b_0(E_n)e^{-g_m(E_n)} \quad (2)$$

where $b_0(E_n)$ is the x-ray fluence incident on the detector without the attenuation phantom present for energy bin E_n . The total fluence on detector m is then the weighted sum of $b_m(E_n)$ with added Poisson noise:

$$y_m = Poisson\left\{\sum_{n=1}^N w_n b_m(E_n)\right\} \quad (3)$$

165 For simplicity, we ignore the focal spot blur, detector noise and scatter events in this study.

Image blur due to the finite focal spot size can be modeled by convolving y_m in Eq. (3) with a Gaussian function with a standard deviation of the focal spot size. Modeling detector noise is extremely complex and beyond the scope of this paper. The scatter events can be modeled by

adding the scatter signal to $\sum_{n=1}^N w_n b_m(E_n)$ in Eq. (3) to account for the increased signal and noise.

170 2.3 Construction of a Digital Head Phantom

We constructed a head digital phantom using the CT (512×512 matrix, 0.68×0.68 mm² pixel size, 1.25 mm slice thickness) scan of a Rando head phantom. The CT images in DICOM format were first read in our in-house software. We then segmented the CT images into three tissue types: air, brain (grey/white matter) and bone according to the intensity (HU number) of each pixel and assigned indexes 1, 2 and 3, respectively, to each tissue type. All 223 slice index images were combined to form one 3D head index phantom stored in a byte format file. Figure 2 shows the index phantom in axial, coronal and sagittal views.

The Mohan 4 MV energy spectrum as illustrated in Table 1 was employed to simulate multi-energetic projection data. For each energy bin, the index phantom was converted into an

180 attenuation phantom by linking each voxel to μ/ρ and ρ of the corresponding tissue in the NIST

lookup table. To facilitate this process, we used a map container to store the elements formed by a key value (energy bin E_n) and a mapped value (μ/ρ) for each tissue type. Interpolation was performed to obtain the μ/ρ if E_n was not in the NIST table.

3 Parallel Processing

185 3.1 GPGPU and OpenCL

We conducted the poly-energetic forward projection on a Dell Precision T7500 Tower Workstation [36]. It features two Intel Xeon quad-core E5507 CPUs, and one Nvidia Tesla C2050 GPGPU. Two commonly used *Thread-Level Parallelism* (TLP) models [37] were used to parallelize the application algorithms. One is *Data Parallelism* (DP) that decomposes data sets
190 into multiple independent data elements to which a single stream of instructions are concurrently applied. DP is often used at a fine-grained level and is supported by a processor's single instruction multiple data (SIMD) function [38]. The other is *Task Parallelism* (TP) that decomposes applications into many independent tasks that can be concurrently executed across different cores. TP is often used at a coarse-grained level and is supported by a processor's
195 multiple instruction multiple data (MIMD) function [39]. .

Because the T7500 computer system has a heterogeneous parallel computing ecosystem with CPUs and GPGPUs, it is critical to partition the workloads properly and assign them to appropriate processors to take full advantage of all (serial and parallel) computing power. GPGPU is suited to process large data sets while CPU is better for serial operations such as disk
200 and network I/Os and other hard-to-parallelized programs. Large data sets spawn a large number of threads which can be efficiently processed with GPGPU's massive parallel structure. Data transfer between CPU and GPGPU should be minimized due to the slowness of PCIe buses.

High spatial memory locality in GPGPU is also preferred because it reduces the memory transaction, increases the cache hit rates and minimizes the waste of bandwidth.

205 An OpenCL program consists of two parts [40]: *kernels* that execute on one or more devices and *a host program* that executes on the host. OpenCL defines an index space called *NDRange* (the grid on CUDA) on devices. Each point in the index space is called a *work-item*. When the host program submits a kernel to a device, an instance of the kernel (a thread) executes for each work-item. Work-items are organized into *work-groups* at coarse-grained level, each of which is
210 scheduled to one multiprocessor independently. Because C2050's smallest execution unit is a warp, the work-group size should be a multiple of 32 for the best performance. Work-groups often work with local memory to eliminate redundant stride access on global memory if the program has spatial locality.

DP is supported by mapping each work-item to one or more data element(s). TP is supported by
215 submitting multiple task kernels across CPU cores or GPU multiprocessors. Each of these kernels equivalently has only one work-item, indicating that the other 31 cores on each multiprocessor of C2050 will be wasted. As a result, TP is usually explored on CPU cores: one task kernel for each core.

Figure 3 shows a schematic architecture of C2050 GPGPU memory model. Both memory access
220 pattern and register usage have a significant impact on the system performance. Please refer to [40] for more details.

3.2 Implementation of the Poly-Energetic Projection

The poly-energetic projection application described in section 2 was first implemented as a single-threaded C/C++ application and it took about 8.83 seconds to finish one projection for
225 each energy bin. To improve the speed, we partitioned the workloads of the projection operation

and scheduled them to all available processors (CPU cores and GPGPU) in the T7500 ecosystem. We decomposed the low-degree parallel and serial workloads into multiple tasks on the CPU using TP and partitioned the high-degree parallel workloads on the GPGPU using DP. For the C2050 GPGPU, we used the OpenCL 1.1 driver from Nvidia's GPU Computing SDK v4 while the OpenCL 1.1 driver from Intel's OpenCL SDK 1.1 was used for Xeon E5507 CPU.

As illustrated in Figure 4, the processing of each energy bin consists of a sequence of three tasks: (1) phantom conversion, (2) line integral calculation and (3) exponential and weighting of the projection. Task 1 only needs to be performed once (for the first angle) while Tasks 2 and 3 are executed for each gantry angle. Therefore, the processing time for the first DRR is higher than that for the subsequent images.

We investigated the processing speed for the first and subsequent polyenergetic DRR(s) for two different scenarios. In the first scenario (Figure 5A and 6A), the number of DRRs are not known in advance and the gantry angle of the next DRR depends on the processing results of the previous DRRs. One example of this scenario is IGRT using the 2D-3D matching. The calculation of all energy bins for the current DRR must be completed before the calculation for next DRR can start. In the second scenario (Figure 7A), the number and angle of all projection images are predetermined, for example, the calculation of projection images for CBCT reconstruction. In this case, it is more efficient to process each energy bin for all imaging angles first and sum polyenergetic images from all energy bins at the end to reduce the data transfer to/from the GPU.

For each scenario, we investigated the task overlapping strategy and the sequential method. The sequential method (Figures 5B, 6B and 7B) processes each energy bin serially, i.e., the calculation of the next energy bin cannot start until all tasks for the current energy bin are

completed. The task overlapping strategy (Figures 5A, 6A and 7A), as explained in the next
250 section, relies on the dispatcher to allow tasks of different energy bins to execute concurrently.

3.3 Task overlapping strategy

The task overlapping strategy (Figures 5A, 6A and 7A) takes advantage of the fact that no data
dependency exists between different energy bins so that all energy bins can be scheduled to run
concurrently if there are enough hardware processors. We first partitioned the application into
255 concurrent processing of all the energy bins. The tasks of each energy bin were scheduled to run
on CPU (Tasks 1 and 3 handled by TP) or GPGPU (Task 2 handled by DP) using a dispatcher
(Section 3.4). Because the tasks for different energy bins could overlap, the parallelism was
achieved through coarse-grained level TP.

For each energy bin Task 1 converts the index phantom into the attenuation phantom on a one-
260 dimensional array and provides the attenuation array to Task 2. Though the initializations on
array elements are independent, decomposing it using DP on either CPU or GPGPU is
unnecessary due to low parallelism and the small number (~ 5) of operations. Therefore, we
scheduled the Task 1 kernel on the CPU using TP to maximize the number of kernels (one for
each energy bin) that could run in parallel. Because two Intel Xeon quad-core E5507 CPUs in
265 the T7500 computer system have a total of eight cores, the maximal number of overlapping
energy bins for Task 1 on the CPU is eight. Note that for each energy bin, the phantom
conversion in Task 1 is performed only once for the first angle production (Figure 5A). The
converted attenuation phantoms are used for the subsequent angles where only Task 2 and Task
3 are required (Figure 6A).

270 Task 2 (Figures 5A and 6A) calculates the line integrals in Eq. (1) for all detector pixels for a
single angle. Because there is no data dependency for the ray-driven calculation, the line integral

can be processed independently and it is natural to use each GPU work-item to compute the line integral along each ray in parallel (we refer to as single-work-item-for-single-ray). Since Task 2 has many operations, we scheduled its kernels on GPGPU using DP so that all C2050's

275 multiprocessors could run some of the 4096 ($=512 \times 512/64$) work-groups in parallel.

Task 3 post-processes the line integrals of Task 2 by performing the exponential and weighting operations in Eqs. (2) and (3). Although these two operations can be included in Task 2, we scheduled them in Task 3 on the CPU using TP because the 8-core CPUs were under-utilized in comparison to the single C2050 GPGPU. Running Task 3 on the CPU also mitigated the register
280 spilling [40] pressure on the C2050 GPGPU.

We also employed both task-overlapping (Figure 7A) and sequential (Figure 7B) methods to generate a set of polyenergetic projection images over 360 angles and compared the performance with others [32]. Here Task 1 in Figures 7A and 7B is the same as that in Figures 5A and 5B but Task 2 (computing the line integrals) and Task 3 (post-processing Task 2's output) are different
285 from the ones in Figures 5A and 5B.

3.4 Single-Threaded Dispatcher

A dispatcher algorithm was implemented as part of the host program to drive the parallelism in Figures 5A, 6A and 7A using the regular single-threaded host program. Figure 8 displays the flow chart of the dispatcher algorithm. Since scheduling more energy bins means more

290 parallelism, the workflow first asynchronously schedules as many energy bins as possible until it fails (if Task 1 invocation is synchronous, it will block the dispatcher workflow and reduce parallelism). The failure is due to out of memory on either the host or the GPGPU. If the scheduling attempt fails, or all energy bins are scheduled and there are still pending tasks running on either CPU or GPGPU, the dispatcher will call "Advance Tasks" that iterates all tasks for

295 each of the scheduled energies and advances to the next task asynchronously if the current one has been done. Since memory will be released as long as it is no longer needed by tasks during the advancement, the scheduling of the next energy bin will most likely succeed. If all scheduled tasks are still running, there will be no task advancement for **this** polling iteration and the dispatcher will sleep for a heuristic period of time to avoid wasting **too many** CPU cycles.

300 The high-level parallelism of the dispatcher depends on the overlapping degree, which is in turn determined by available hardware processors (here eight CPU cores and one GPGPU), number of tasks, task running time and the scheduling algorithm itself. The parallelism scheme of the first DRR generation in Figure 5A is slightly different from the subsequent ones in Figure 6A due to the number of tasks. Task 1 is the bottleneck for the task overlapping scheme in Figure 5A because both Task 2 and Task 3 run much faster. Figure 7A shows the overlapping scheme for generating a set of polyenergetic projection images, where Task 2 is clearly the hurdle. Although Figures 5A, 6A and 7A demonstrate that tasks from different energies can overlap at some moment of time, the degree of the overlap varies.

3.5 Performance Tuning

310 The performance tuning plays an important role for parallel processing. The following remarks highlight some of memory access and work-group patterns related to this study.

CPU as OpenCL Device: In order to take advantage of the SIMD parallelism in the CPU core, tasks should pack data properly and use simple or no flow control. Our forward projection host program allocated **a** buffer directly from the host memory to avoid unnecessary data copy so that 315 more tasks can be executed under a very limited host memory constraint.

Work-Group Size: The work-group and global work-item sizes were optimized to maintain a high “occupancy” (the ratio of the number of active warps per **multiprocessor** to the maximum

number of possible active warps) [40] for maximizing CPU, GPGPU and hardware **utilizations**.

We tuned the work-group size to 64 for Task 2 **and** created 4096 ($=512 \times 512 / 64$) work-groups so
320 that every **multiprocessor** had at least one work-group to execute. The large work-group size also
made the latency hiding easier and guaranteed the scalability for future devices with more
multiprocessors.

Register Spilling vs. Private Memory: The performance of Task 2 was improved significantly by
tuning the usages of registers and private memory. Task 2 used up the maximum number of
325 registers allowed by a work-item (63 for C2050). We tried to lower the number of registers to get
a higher occupancy but the performance actually degraded. Even with all **63** registers, Task 2
still suffered register spilling due to the large amount of operations. This was another reason why
Task 3 was off-loaded to **the** CPU.

3.6 Experiments

330 Numerical experiments were conducted to test our OpenCL-based implementation of ray-driven
poly-energetic forward projection, **and to compare the performance between the task overlapping
strategy and the sequential method.** A set of 2D polyenergetic projection images of 512×512
matrix with a pixel size of $1.06 \times 1.06 \text{ mm}^2$ were generated for different gantry angles **for the
constructed digital head phantom described in Section 2.3.** The distance from the source to the
335 center of rotation was 100 cm and the distance from the source to the detector was 150 cm.
Because there is no data dependency for the ray-driven line integral, we allocated each work-
item to compute the line integral of each ray in parallel.

4 Results

**Task 1 took ~ 120.4 ms to prepare the index phantom and to convert it to the attenuation
340 phantom for each energy bin. We used Nvidia's Excel occupancy calculator for performance**

tuning of Task 2 and achieved a 16.2 ms optimal running time with a workgroup size of 64 using all registers and no local memory. Since the single-threaded CPU implementation needed ~8.8 s for task 2, we achieved a $(8.8 \text{ s} / 16.2 \text{ ms}) = 543$ -time performance improvement using the OpenCL/GPGPU-based implementation. Task 3 took ~2.8 ms on CPU.

345 The total computation time for generating the first poly-energetic projection image is 2230.4 ms $= (120.4 + 16.2 + 2.8) \times 16$ for the sequential method (Figure 5B), while the task overlapping strategy (Figure 5A) requires ~382 ms $(= 120.4 \times 2 + 8.8 + 16.2 \times 8 + 2.8)$, a 5.84x performance improvement; the computation time on CPU is $(120.4 \text{ ms} + 8.8 \text{ s} + 2.8 \text{ ms}) \times 16 = 142.8 \text{ s}$. For subsequent images, the total processing time for the task overlapping strategy (Figure 6A) is 262 ms $= (16.2 \times 16 + 2.8)$, or 1.16 x faster than $(16.2 + 2.8) \times 16 = 304 \text{ ms}$ for the serial calculation (Figure 6B), while the computation time on CPU is $(8.8 \text{ s} + 2.8 \text{ ms}) \times 16 = 141 \text{ s}$. The total processing time for calculating poly-energetic projection images over 360 angles is $(120.4 + 5832 \times 16 + 1008) = 94,440.4 \text{ ms}$ with the overlapping strategy (Figure 7A) in contrast to $(120.4 + 5832 + 1008) \times 16 = 111,366.4 \text{ ms}$ for the sequential process method (Figure 7B), leading to a 1.18 x speedup. The computation time for generating 360 projection images for a single energy is $(16.2 \text{ ms} + 2.8 \text{ ms}) \times 360 = 6.8 \text{ s}$. The images generated by the task overlapping scheme are identical to those by the sequential one. Figures 9A and 9B illustrate the processing times of DRR generation and their speedup over CPU, respectively.

Figure 10 compares the polyenergetic projection images of the Rando head phantom for the Mohan 4 energy spectrum (Table 1) calculated via the CPU-based and OpenCL/GPGPU-based approaches. Figure 10 (A) is the image for the 0-degree gantry angle using the CPU-based approach and Figure 10 (C) the OpenCL/GPGPU-based approaches while Figure 10 (E) is the relative difference of these two images. Similarly, Figures 10 (B), (D) and (F) show the images

for the 90-degree gantry angle. The difference between these two approaches is on the order of 10^{-6} for both gantry angles, which is too small to distinguish visually.

Figure 11 illustrates the projection images calculated for different x-ray energies: (A) and (B) 0.25 MeV, (C) and (D) 0.75 MeV, and (E) and (F) 4 MeV for 0-degree and 90-degree gantry angles. As the energy increases, the projection images become lighter due to less attenuation.

5 Discussion

Due to the uniform and scalable programming model, OpenCL has a unique advantage over other languages for programming GPU for parallel processing. The uniform programming model allows the development and debugging of the host and kernel codes on CPU with Intel's OpenCL SDK first. The codes can later be ported to a GPGPU environment with slight modifications and optimizations. This capability is particularly useful for projects with a tight budget constraint. For example, the two E5507 CPUs used in this study cost about \$550 and the C2050 GPGPU costs about \$2,499. It turned out to be very economical and convenient for this project to develop kernel codes on multi-core CPU and delay the implementation of parallel processing until the GPGPU was available. The scalable model, on the other hand, makes it easy to scale the code developed for single-core GPGPU to multi-core GPGPU with minor modifications and re-optimization.

One major critique for OpenCL is that it achieves uniform and portable programmability across heterogeneous platforms at the cost of performance compared to vendor specific models such as Nvidia's CUDA and AMD's APP. It is generally true that the performance of OpenCL is inferior to other models for programming GPGPU as evidenced by a few published comparisons. For example, Danalis et al [41] compared the performance of OpenCL and CUDA on C1060 for several kernels using a benchmark suite they developed for heterogeneous parallel computing

platforms, and reported that OpenCL was trailing CUDA for all kernels (ranging from 2.6% to 14.2%). Karimi et al [33] compared the performance of CUDA and OpenCL on GeForce GTX 260 including data transfer time to and from GPU, kernel execution times, and end-to-end application execution times. For kernel execution times, OpenCL was trailing CUDA on all quantum bits. Du et al. [42] also compared CUDA and OpenCL on Tesla C2050 and found that with proper tuning, OpenCL implementation nearly matched the CUDA implementation in speed. Therefore, the differences between OpenCL and other modality were marginal and the slight degradation in performance is worthwhile considering the advantages of uniform and portable programmability.

For the same parallelization strategy, our OpenCL implementation performed slightly better than the CUDA implementation by Chou et al [32]. In their study, projection images for a mono-energetic ray source were generated using the CUDA-based ray-driven forward projection on an NVIDIA Tesla C1060 GPU to generate 360 512×512 projection images of a digital phantom.

The single-thread-for-single-ray strategy employed in their study is equivalent to our single-work-item-for-single-ray in OpenCL and it took ~38.56 s to produce a set of 360 projection images. In comparison, our OpenCL-based forward projection took $(16.2 \text{ ms} + 2.8 \text{ ms}) \times 360 = 6.8 \text{ s}$ to acquire 360 projection images of the same size for one energy bin. Although the NVIDIA Tesla C2050 is a more powerful GPU than the NVIDIA Tesla C1060 in terms of GFLOPs, the average number (486) of sampling voxels along each ray in our experiment was almost 4 times of that (128) in the study by Chou et al. Note that in the same publication Chou et al [32] also developed more efficient multithreads-for-single-ray and multithreads-for-multiray strategies for CUDA. We plan to investigate whether similar approaches can be implemented using OpenCL.

410 Comparison of the task overlapping strategies (Figures 5A, 6A and 7A) with the sequential
methods (Figures 5B, 6B and 7B) indicates that more tasks leads to higher degree of
overlapping, hence better performance for the task overlapping strategy. Even though this study
has only three tasks, significant performance improvements (5.84x, 1.16x and 1.18x) were
achieved with the task overlapping strategies. As the number of tasks grows, the performance
415 improvement is expected to be more prominent. The design of our dispatcher was not generic
and was not intended to be an optimal scheduling algorithm. Instead, we focused on the
OpenCL's uniform capability to schedule different workloads across different parallel computing
processors.

Comparison of DRR with KV or MV radiography acquired in the treatment position is an
420 important IGRT technique for patient setup and tracking. The proposed poly-energetic forward
projection for image formation allows production of more truthful DRR using the x-ray energy
spectrum of the imaging source on the treatment machine, not the CT simulator. More realistic
DRR will lead to more accurate 2D/2D and 2D/3D image matching as the variation in image
quality due to different x-ray energy spectrum is minimized. However, the more realistic image
425 quality is obtained at the cost of additional processing time in proportion to the number of energy
bins and might not be feasible for the 2D/3D image matching that requires real-time rendering of
DRR from the simulation CT. This obstacle was addressed with our OpenCL/GPGPU-based
implementation of the proposed poly-energetic forward projection which is 543-time faster than
the CPU-based implementation. With an image formation rate of a few tenths second per DRR
430 (depending on the number of energy bins), it is possible to perform the 2D/3D image registration
in real time and track the patient motion with 6 degrees of freedom.

The poly-energetic projection can also be used to generate fast and realistic projection images for medical imaging research and development. For example, although the Monte Carlo simulation is the most accurate method for generating projection images for CBCT research, producing a few hundred projection images is very time-consuming. With the developed poly-energetic projection technique, realistic projection images can be obtained within a few minutes for CBCT reconstruction. Note that unlike the Monte Carlo simulation, the scatter events are not considered in the forward projection operations. As mentioned earlier, the scatter events can be included as an additive term in Eq. (3) prior to adding the Poisson noise and the increased noise due to the scattering is included in the Poisson noise term in Eq. (3).

6 Conclusions

We have constructed digital attenuation phantoms by segmenting the anatomical CT images into different tissue types and assigning each tissue type with the attenuation coefficients for different X-ray energies. The Siddon's ray-trace method [35] was used to calculate the transmission line integral through the attenuation phantom for an x-ray source with known energy spectrum. Calculation of the multi-energetic projection data was accelerated using OpenCL to program parallel processing on GPGPU. We decomposed the low-degree parallel and serial workloads into multiple tasks on the CPU using TP and partitioned the high-degree parallel workloads on the GPGPU using DP. A 543-time performance improvement was achieved using the OpenCL/GPGPU-based implementation in comparison to the single-threaded line integral on the CPU and the difference between the CPU-based and OpenCL/GPGPU-based approaches was negligible.

References

1. Wang, H., R.J. Jaszczak, and R.E. Coleman, *Solid geometry-based object model for Monte Carlo simulated emission and transmission tomographic imaging systems*. Medical Imaging, IEEE Transactions on, 1992. **11**(3): p. 361-372.
2. Zubal, L.G., C.R. Harrell, and P.D. Esser, *Monte Carlo determination of emerging energy spectra for diagnostically realistic radiopharmaceutical distributions*. Nuclear Instruments and Methods in Physics Research Section A: Accelerators, Spectrometers, Detectors and Associated Equipment, 1990. **299**(1-3): p. 544-547.
3. Zubal, I.G. and C.R. Harrell, *Voxel based Monte Carlo calculations of nuclear medicine images and applied variance reduction techniques*. Image and Vision Computing, 1992. **10**(6): p. 342-348.
4. Zubal, I.G., Harrell, C. R., Smith, E. O., and Smith, A. L. . *Two dedicated software, voxel-based, anthropomorphic (torso and head) phantoms*. in the *International Workshop, National Radiological Protection Board*. 1995. Chilton, UK.
5. Zubal, I.G., et al., *Computerized three-dimensional segmented human anatomy*. Medical Physics, 1994. **21**(2): p. 299-302.
6. Zubal, I.G., et al. *High resolution, MRI-based, segmented, computerized head phantom*. 1999. United States.
7. Xu, X.G., T.C. Chao, and A. Bozkurt, *Vip-Man: An Image-Based Whole-Body Adult Male Model Constructed From Color Photographs of the Visible Human Project for Multi-Particle Monte Carlo Calculations*. Health Physics, 2000. **78**(5): p. 476-486.
8. Hoffman, E.J., et al., *3-D phantom to simulate cerebral blood flow and metabolic images for PET*. Nuclear Science, IEEE Transactions on, 1990. **37**(2): p. 616-620.
9. Collins, D.L., et al., *Design and construction of a realistic digital brain phantom*. Medical Imaging, IEEE Transactions on, 1998. **17**(3): p. 463-468.
10. Segars, W.P., D.S. Lalush, and B.M.W. Tsui, *Modeling respiratory mechanics in the MCAT and spline-based MCAT phantoms*. Nuclear Science, IEEE Transactions on, 2001. **48**(1): p. 89-97.
11. Seltzer, J.H.H.a.S.M., *Tables of X-Ray Mass Attenuation Coefficients and Mass Energy-Absorption Coefficients from 1 keV to 20 MeV for Elements Z = 1 to 92 and 48 Additional Substances of Dosimetric Interest*.
12. Russakoff, D.B., et al. *Fast calculation of digitally reconstructed radiographs using light fields*. 2003. San Diego, CA, USA: SPIE.
13. Russakoff, D.B., et al., *Fast generation of digitally reconstructed radiographs using attenuation fields with application to 2D-3D image registration*. Medical Imaging, IEEE Transactions on, 2005. **24**(11): p. 1441-1454.
14. Laycock, M.F.O.D.a.S. *Accelerated generation of digitally reconstructed radiographs using parallel processing*. in *Proc. Medical Image Understanding and Analysis 2009*. 2008.
15. Ruijters, D., B.M.t. Haar-Romeny, and P. Suetens, *GPU-accelerated digitally reconstructed radiographs*, in *Proceedings of the Sixth IASTED International Conference on Biomedical Engineering 2008*, ACTA Press: Innsbruck, Austria. p. 431-435.
16. C Gendrin, C.W., M Figl, D Georg, H Bergmann, W Birkfellner. *Implementation of real-time 2D/3D image registration in radiation oncology*. in *World Congress on Medical Physics and Biomedical Engineering September 712 2009*. 2009. Munich Germany: Springer.
17. Xu, F. and M. K., *Accelerating popular tomographic reconstruction algorithms on commodity PC graphics hardware*. Nuclear Science, IEEE Transactions on, 2005. **52**(3): p. 654-663.
18. Xu, F. and K. Mueller, *Real-time 3D computed tomographic reconstruction using commodity graphics hardware*. Physics in Medicine and Biology, 2007. **52**(12): p. 3405.

- 500 19. Zhao, X., J.-J. Hu, and P. Zhang, *GPU-based 3D cone-beam CT image reconstruction for large data volume*. Journal of Biomedical Imaging, 2009. **2009**: p. 1-8.
20. D. Riabkov, X.X., D. Tubbs, A. Cheryauka. *Accelerated cone-beam backprojection using GPU-CPU hardware*. in *Proc. 9th Int'l Meeting Fully Three-Dimensional Image Reconstruction in Radiology and Nuclear Medicine (Fully 3D '07)*. 2007.
- 505 21. Ino, F., S. Yoshida, and K. Hagihara, *RGBA packing for fast cone beam reconstruction on the GPU*. Vol. 7258. 2009: SPIE. 725858.
22. Cabral, B., N. Cam, and J. Foran. *Accelerated volume rendering and tomographic reconstruction using texture mapping hardware*. in *VVS '94: Proceedings of the 1994 symposium on Volume visualization*. 1994. ACM Press.
- 510 23. Xu, F., et al., *On the efficiency of iterative ordered subset reconstruction algorithms for acceleration on GPUs*. Comput. Methods Prog. Biomed., 2010. **98**(3): p. 261-270.
24. Scherl, H., et al. *Fast GPU-Based CT Reconstruction using the Common Unified Device Architecture (CUDA)*. in *Nuclear Science Symposium Conference Record, 2007. NSS '07. IEEE*. 2007.
- 515 25. Andreas Weinlich, B.K., Holger Scherl, Markus Kowarschik and Joachim Hornegger. *Comparison of High-Speed Ray Casting on GPU using CUDA and OpenGL*. in *High-performance and Hardware-aware Computing (HipHaC 2008)*. 2008. Como (Italy).
26. Knaup, M., S. Steckmann, and M. Kachelriess. *GPU-based parallel-beam and cone-beam forward- and backprojection using CUDA*. in *Nuclear Science Symposium Conference Record, 2008. NSS '08. IEEE*. 2008.
- 520 27. Byunghyun Jang, D.K., Synho Do, Homer Pien. *Multi GPU implementation of iterative tomographic reconstruction algorithms*. in *Biomedical Imaging: From Nano to Macro, 2009. ISBI '09. IEEE International Symposium on*. 2009.
28. Keck, B., et al., *GPU-accelerated SART reconstruction using the CUDA programming environment*. Vol. 7258. 2009: SPIE. 72582B.
- 525 29. B. Keck, H.H., H. Scherl, M. Kowarschick and J. Hornegger, *High resolution iterative ct reconstruction using graphics hardware*, in *Nuclear Science Symposium Conference Record (NSS/MIC), 2009 IEEE2009*. p. 4035-4040.
30. Noël, P.B., et al., *GPU-based cone beam computed tomography*. Computer Methods and Programs in Biomedicine, 2010. **98**(3): p. 271-277.
- 530 31. Okitsu, Y., F. Ino, and K. Hagihara, *High-performance cone beam reconstruction using CUDA compatible GPUs*. Parallel Computing, 2010. **36**(2-3): p. 129-141.
32. Chou, C.-Y., et al., *A fast forward projection using multithreads for multirays on GPUs in medical image reconstruction*. Med. Phys., 2011. **38**(7): p. 4052-4065.
- 535 33. Karimi, K., N. Dickson, and F. Hamze, *A Performance Comparison of CUDA and OpenCL*. 2010.
34. Pratx, G. and L. Xing, *GPU computing in medical physics: A review*. Medical Physics, 2011. **38**(5): p. 2685-2697.
35. Siddon, R.L., *Fast calculation of the exact radiological path for a three-dimensional CT array*. Medical Physics, 1985. **12**(2): p. 252-255.
- 540 36. *Dell Precision™ T5500/T7500 Tower Workstations Technical Guide*.
37. Wikipedia, *Task Parallelism and Data parallelism*.
38. Wikipedia, *SIMD*.
39. Wikipedia, *MIMD*.
40. Khronos, *The OpenCL Specification*, A. Munshi, Editor 2009.
- 545 41. Danalis, A., et al. *The Scalable Heterogeneous Computing (SHOC) benchmark suite*. in *Proceedings of the 3rd Workshop on General-Purpose Computation on Graphics Processing Units*. 2010. Pittsburgh, Pennsylvania: ACM.

42. Peng Du, R.W., Piotr Luszczek, Stanimire Tomov, Gregory Peterson, Jack Dongarra, *From CUDA to OpenCL: Towards a Performance-portable Solution for Multi-platform GPU Programming*, 2011, University of Tennessee.
- 550

Table 1. Mohan4 energy spectrum. The first column lists energy bins and the second column lists the counts for each energy bin from which we can calculate weight w_n in Eq. 3.

| Energy (MeV) | Counts/bin |
|-----------------|------------|
| 0.25 | 0.0111 |
| 0.50 | 18.11 |
| 0.75 | 72.09 |
| 1.00 | 54.08 |
| 1.25 | 53.57 |
| 1.50 | 56.33 |
| 1.75 | 34.69 |
| 2.00 | 26.21 |
| 2.25 | 24.91 |
| 2.50 | 16.97 |
| 2.75 | 13.99 |
| 3.00 | 7.035 |
| 3.25 | 8.833 |
| 3.50 | 8.809 |
| 3.75 | 8.838 |
| 4.00 | 0.9982 |

Figure Legends

Figure 1. Illustration of the ray trace method for calculating the line integral along different rays for a two-dimensional object. The solid dots indicate the boundaries of intersecting pixels and the interval between two neighboring dots defines the chord length of intersection. Note that the numbers of intersecting pixels along ray 1 and ray 2 are different.

Figure 2. Index phantom. (A) transverse slice (B) coronal slice (C) sagittal slice.

Figure 3. Memory Model for the NVIDIA C2050 GPGPU.

Figure 4. The sequence of tasks for each energy bin.

Figure 5A. The task overlapping strategy for generating the first polyenergetic ($E_1, E_2 \dots E_{16}$) projection image. Tasks 1 of the first eight energy bins (E_1 - E_8) start simultaneously at t_0 on eight CPU cores and finish at t_1 . At t_1 , Tasks 1 of the last eight energy bins (E_9 - E_{16}) initiate and Task 2 of the E_1 begins on GPGPU. At t_2 , Task 2 of E_1 ends and Task 2 of E_2 starts. At t_4 , Tasks 1 of E_9 - E_{16} complete and Task 3 of E_1 commences on CPU cores. At t_5 , Task 2 of E_8 ends on GPU and Task 3 starts immediately on CPU; in the meanwhile Task 2 of E_9 initiates on GPU. Tasks 2 and Tasks 3 of the rest energy bins follow the same pattern.

Figure 5B. The sequential method for generating the first polyenergetic ($E_1, E_2 \dots E_{16}$) projection image. Tasks 1 of the first energy bin E_1 start at t_0 on a CPU core and finish at t_1 . At t_1 , Task 2 of the E_1 begins on GPGPU. At t_2 , Task 2 of E_1 ends and Task 3 of E_1 starts. At t_3 , all three tasks of the E_1 finish and the second energy bin E_2 initiates. The rest energy bins follow the same pattern.

Figure 6A. The task overlapping strategy for generating the subsequent polyenergetic projection images. Task 2 of E_1 starts at t_0 and ends at t_1 on GPU. At t_1 , both Task 3 of E_1 and Task 2 of E_2 initiate on CPU and GPU, respectively. The rest energy bins follow the same running pattern.

580 **Figure 6B.** The sequential method for generating the subsequent polyenergetic projection images. Task 2 of E_1 starts at t_0 and ends at t_1 on GPU. Task 3 of E_1 initiates on CPU at t_1 and finishes at t_2 . At t_2 Task 2 of E_2 commences on GPU. The rest energy bins follow the same running pattern.

Figure 7A. The task overlapping strategy for generating polyenergetic projection images over 360 angles. Tasks 1 of the E_1 - E_8 initiate on eight CPU cores concurrently at t_0 and finish at t_1 when Tasks 1 of E_9 - E_{16} start on CPU and Task 2 of E_1 initiates on GPU. At t_2 , Tasks 1 of E_9 - E_{16} end on CPU. At t_3 , Task 2 of E_1 finishes on GPU, Task 3 of E_1 starts on CPU and Task 2 of E_2 initiates on GPU. Tasks 2 and 3 of the rest energies follow the same pattern.

Figure 7B. The sequential method for generating a set of polyenergetic projection images over 360 angles. Task 1 of the E_1 initiates on a CPU core at t_0 and finishes at t_1 when Task 2 of E_1 initiates on GPU. At t_2 , Task 2 of E_1 ends and its Task 3 begins. At t_3 , Task 3 of E_1 finishes and Task 1 of E_2 starts on CPU. The rest energies follow the same pattern.

Figure 8: The dispatcher workflow chart.

Figure 9A. The comparison of computation times for DRR generation using the task overlapping strategy and the sequential method.

Figure 9B. The speedup for DRR generation and line integral over CPU.

Figure 10. The projections calculated by (A) and (C) CPU-based, and (B) and (D) OpenCL-based GPU implementations. (A) and (B) at 0 degree. (C) and (D) at 90 degree. The relative difference images of (A) and (C) is shown in (E), and the relative difference of (B) and (D) in (F).

Figure 11. Projection images at 0 degree (the 1st column) and 90 degree (the 2nd column) for (A) and (B) 0.25 MeV, (C) and (D) 0.75 MeV, and (E) and (F) 4.0 MeV.

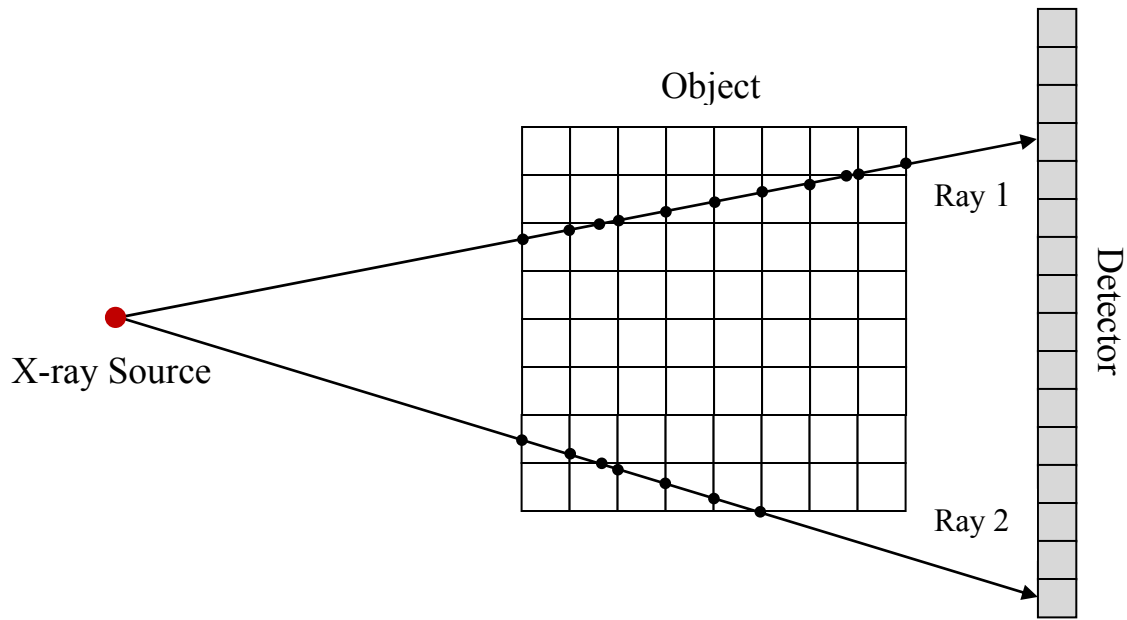
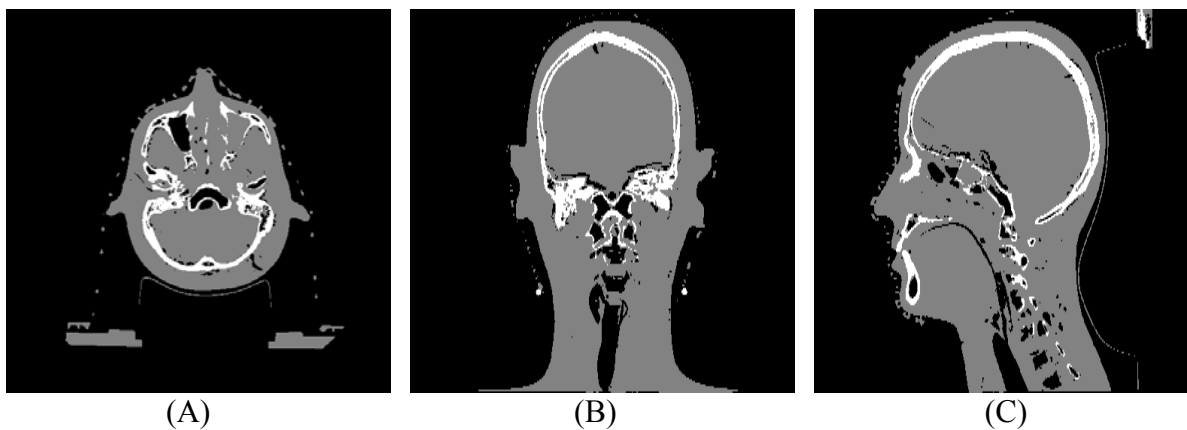
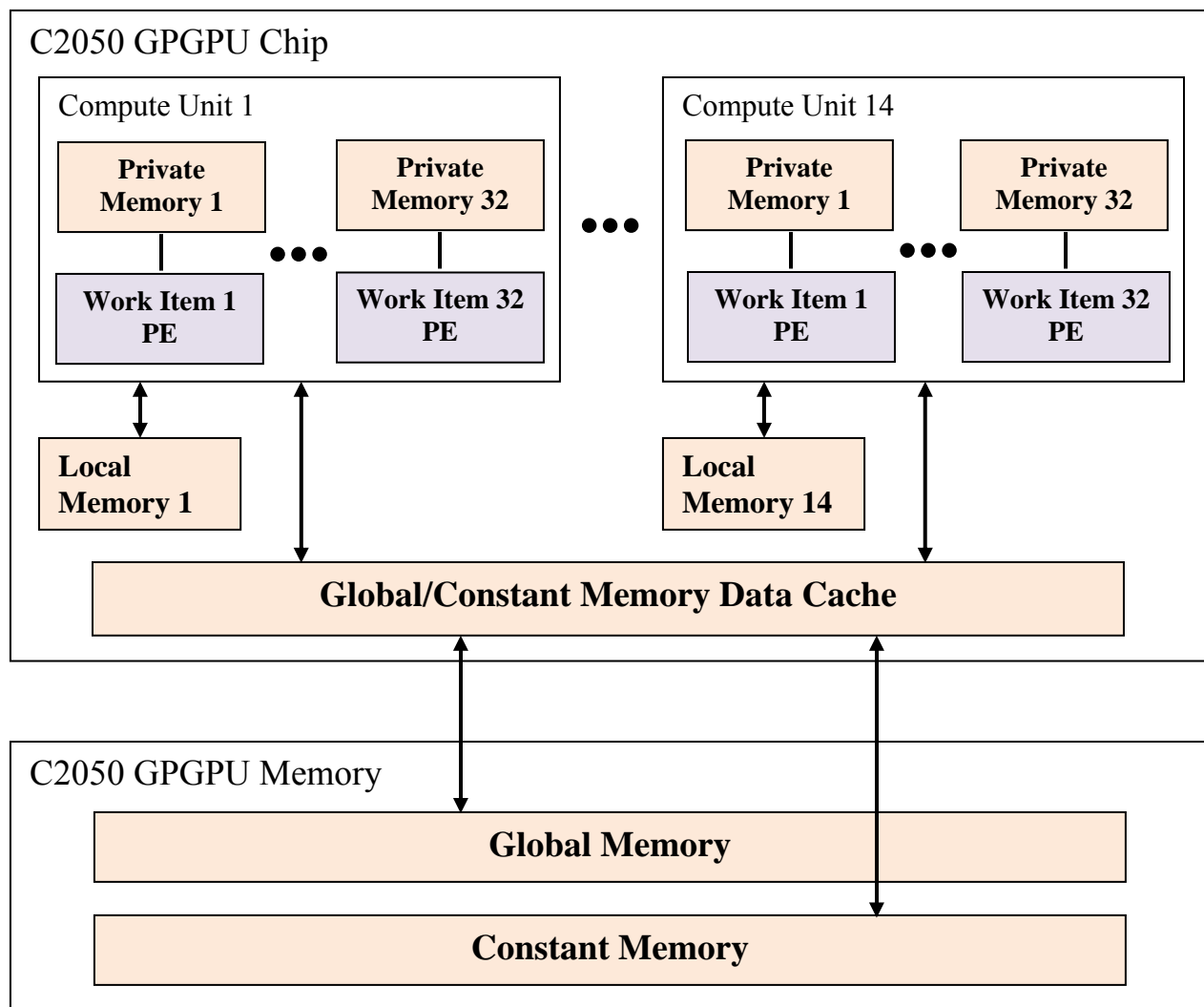


Figure 1. Illustration of the ray trace method for calculating the line integral along different rays for a two-dimensional object. The solid dots indicate the boundaries of intersecting pixels and the interval between two neighboring dots defines the chord length of intersection. The numbers of intersecting pixels along ray 1 and ray 2 are different.

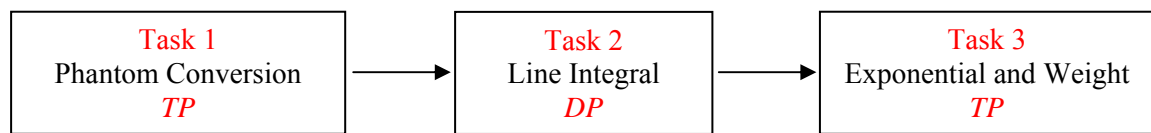


635 **Figure 2.** Index phantom using the CT (512×512 matrix, 0.68×0.68 mm² pixel size, 1.25 mm slice thickness) scan of a Rando head phantom: (A) transverse slice (B) coronal slice (C) sagittal slice.



640

Figure 3: Memory Model for the NVIDIA C2050 GPGPU.



645 Figure 4. The sequence of tasks for each energy bin.

650

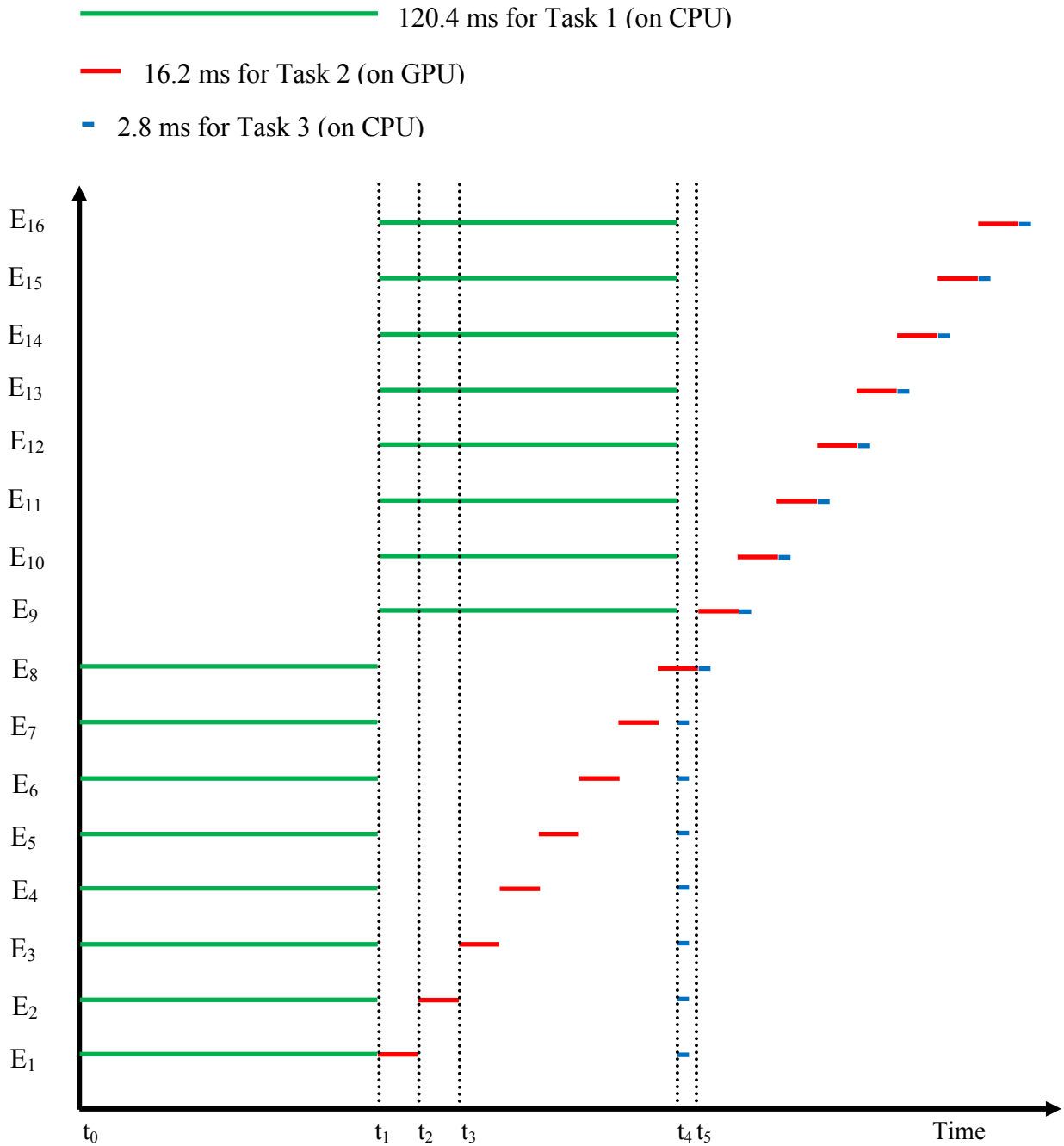


Figure 5A. The task overlapping scheme for generating the first polyenergetic (E₁, E₂...E₁₆) projection image. Tasks 1 of the first eight energy bins (E₁-E₈) start simultaneously at t₀ on eight CPU cores and finish at t₁. At t₁, Tasks 1 of the last eight energy bins (E₉-E₁₆) initiate and Task 2 of the E₁ begins on GPGPU. At t₂, Task 2 of E₁ ends and Task 2 of E₂ starts. At t₄, Tasks 1 of E₉-E₁₆ complete and Task 3 of E₁ commences on CPU cores. At t₅, Task 2 of E₈ ends on GPU and Task 3 starts immediately on CPU; in the meanwhile Task 2 of E₉ initiates on GPU. Tasks 2 and Task 3 of the rest energy bins follow the same pattern.

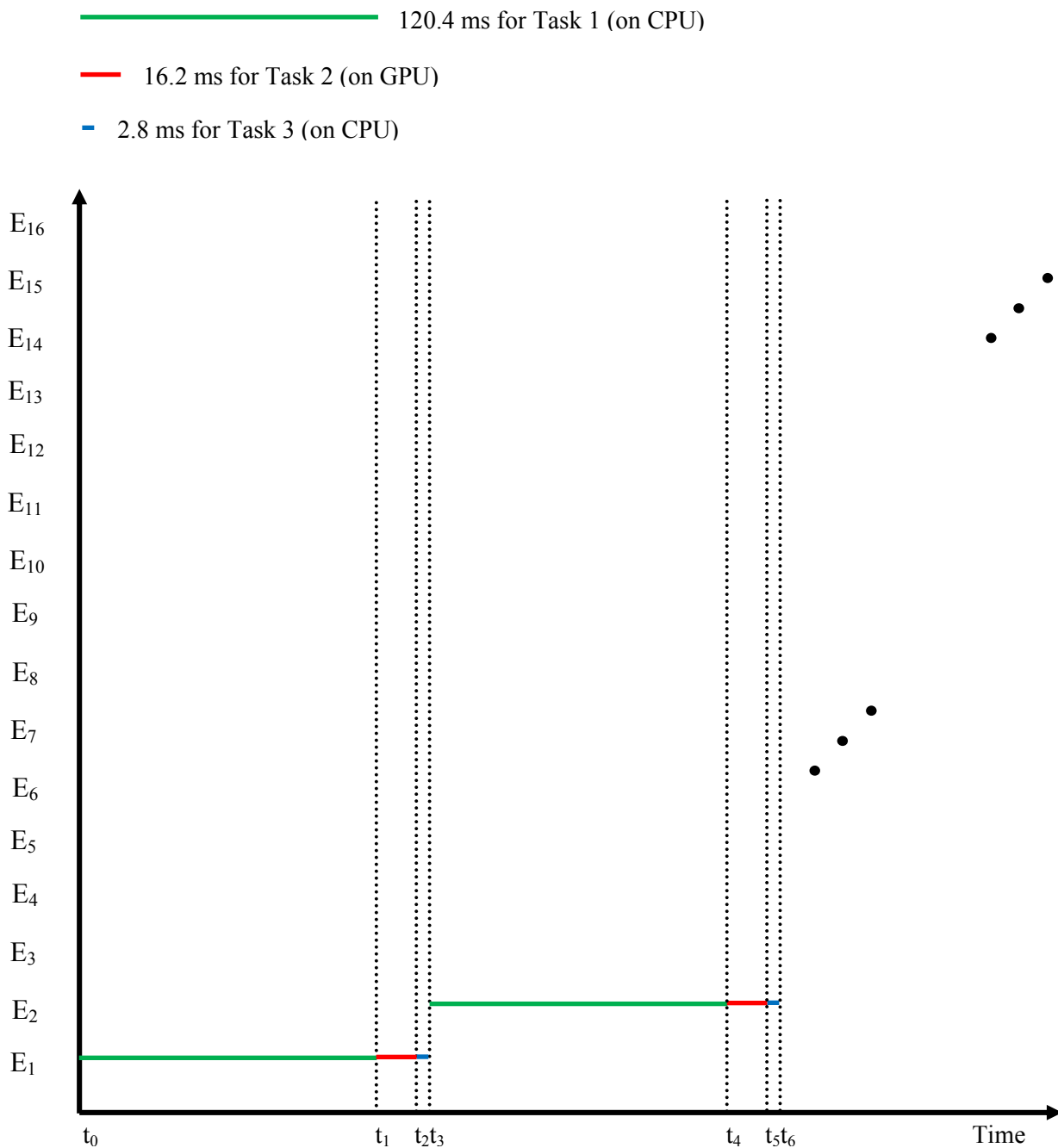


Figure 5B. The sequential scheme for generating the first polyenergetic ($E_1, E_2 \dots E_{16}$) projection image. Tasks 1 of the first energy bin E_1 start at t_0 on a CPU core and finish at t_1 . At t_1 , Task 2 of the E_1 begins on GPGPU. At t_2 , Task 2 of E_1 ends and Task 3 of E_1 starts. At t_3 , all three tasks of the E_1 finish and the second energy bin E_2 initiates. The rest energy bins follow the same pattern.

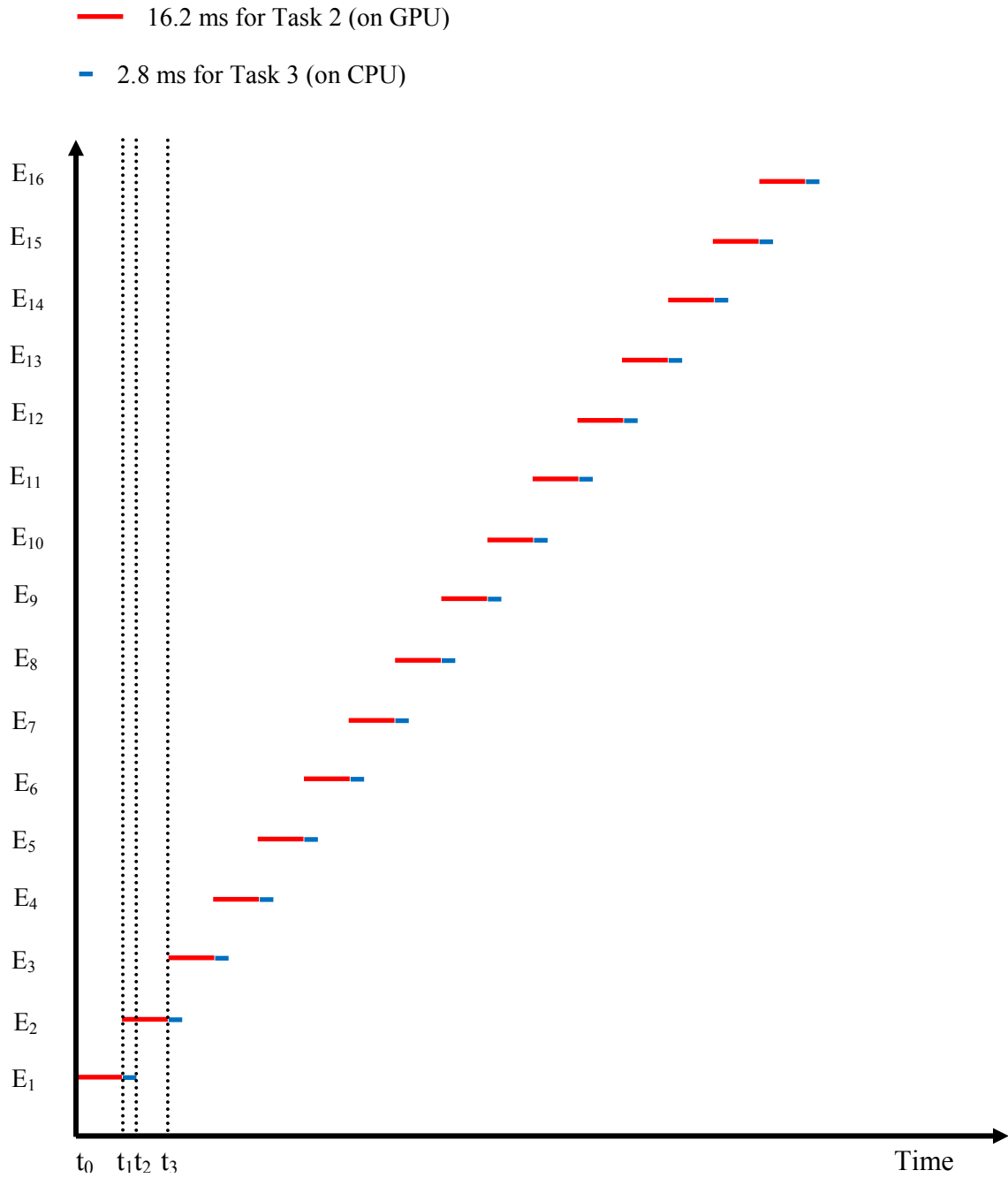


Figure 6A. The task overlapping scheme for generating the subsequent polyenergetic projection images. Task 2 of E_1 starts at t_0 and ends at t_1 on GPU. At t_1 , both Task 3 of E_1 and Task 2 of E_2 initiate on CPU and GPU, respectively. The rest energy bins follow the same running pattern.

— 16.2 ms for Task 2 (on GPU)

— 2.8 ms for Task 3 (on CPU)

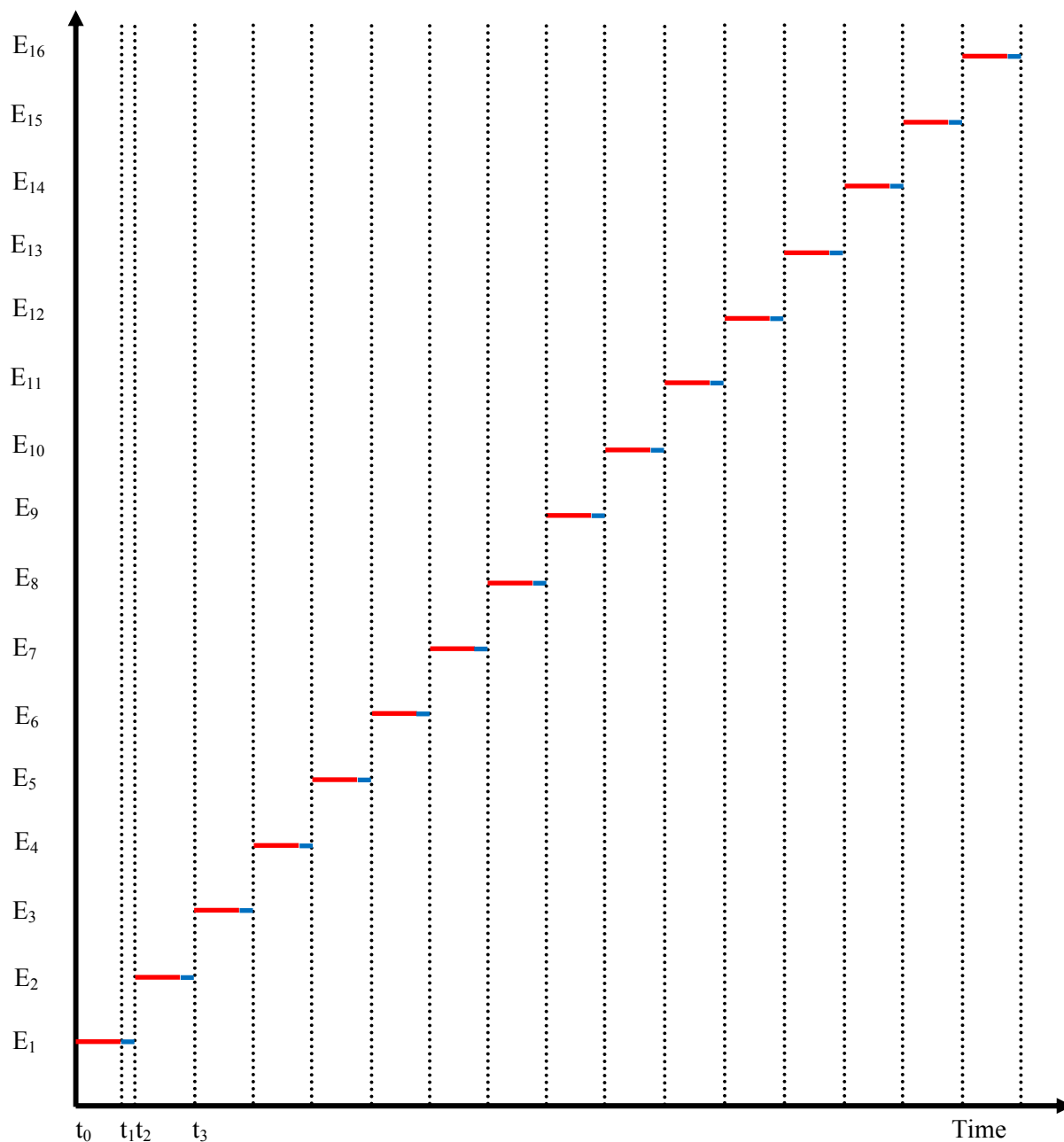


Figure 6B. The sequential scheme for generating the subsequent polyenergetic projection images. Task 2 of E_1 starts at t_0 and ends at t_1 on GPU. Task 3 of E_1 initiate on CPU at t_1 and finishes at t_2 . At t_2 Task 2 of E_2 commences on GPU. The rest energy bins follow the same running pattern.

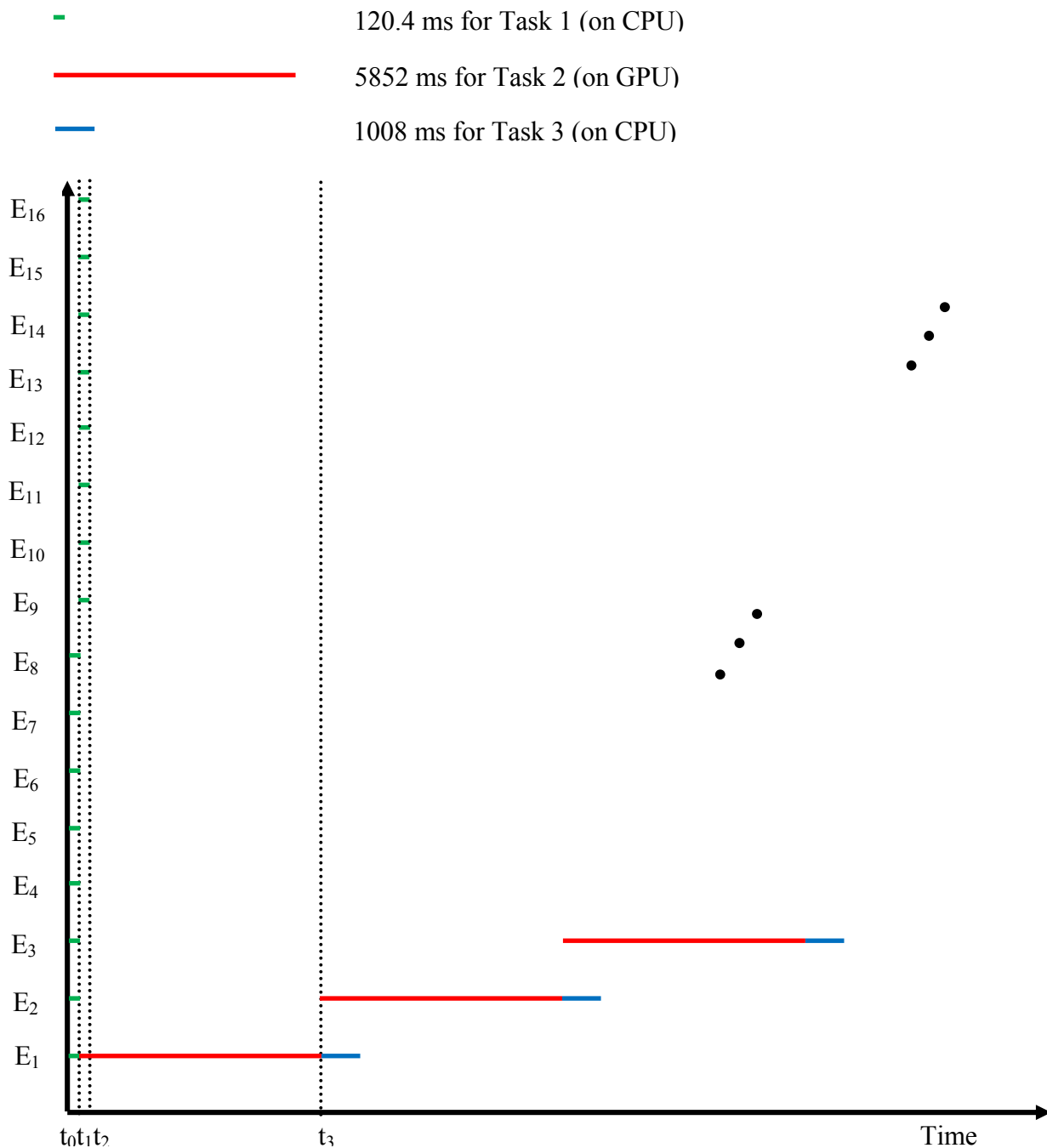


Figure 7A. The task overlapping strategy for generating polyenergetic projection images over 360 angles. Tasks 1 of the E₁-E₈ initiate on eight CPU cores concurrently at t₀ and finish at t₁ when Tasks 1 of E₉-E₁₆ start on CPU and Task 2 of E₁ initiates on GPU. At t₂, Tasks 1 of E₉-E₁₆ end on CPU. At t₃, Task 2 of E₁ finishes on GPU, Task 3 of E₁ starts on CPU and Task 2 of E₂ initiates on GPU. Tasks 2 and 3 of the rest energies follow the same pattern.

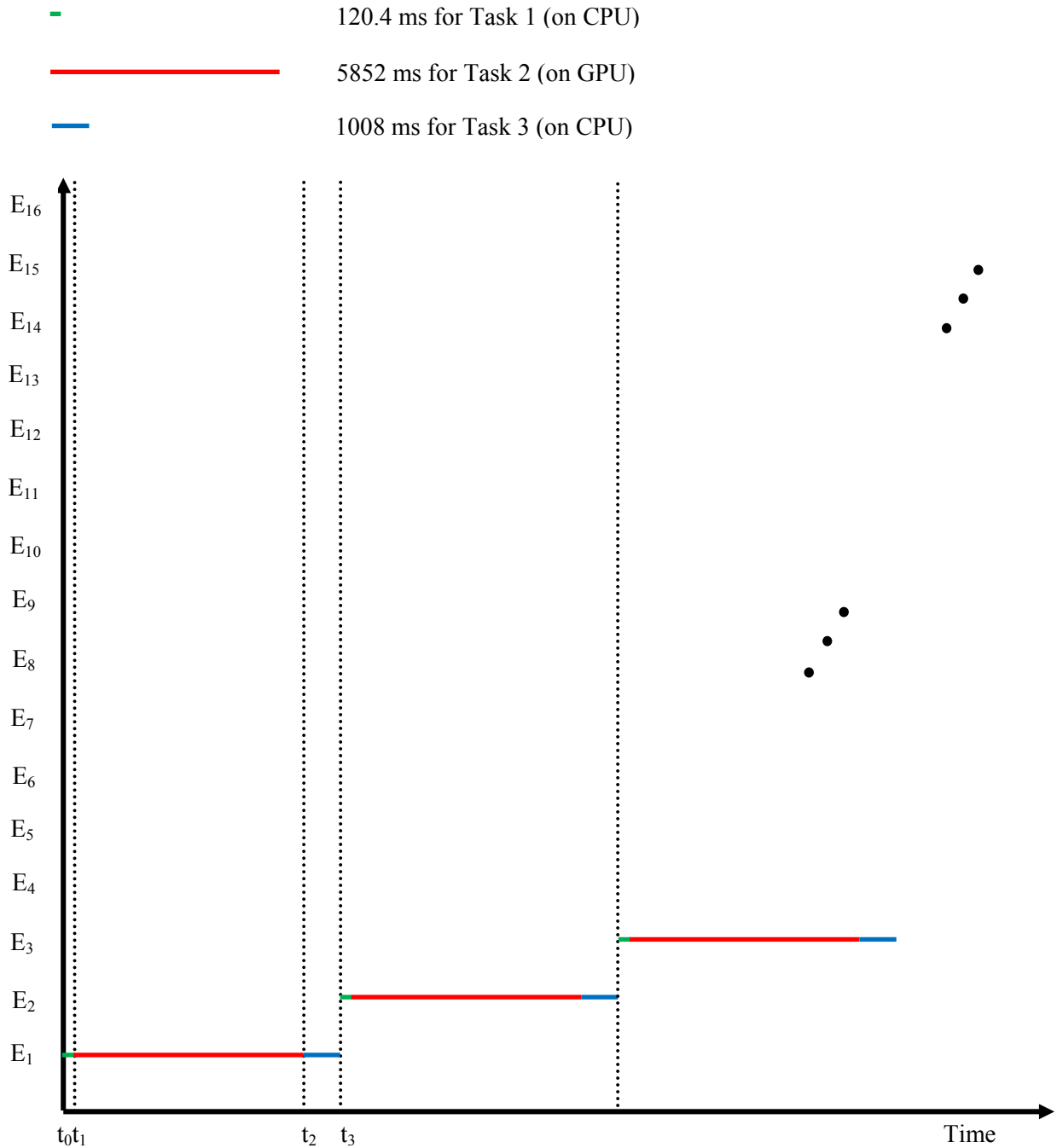
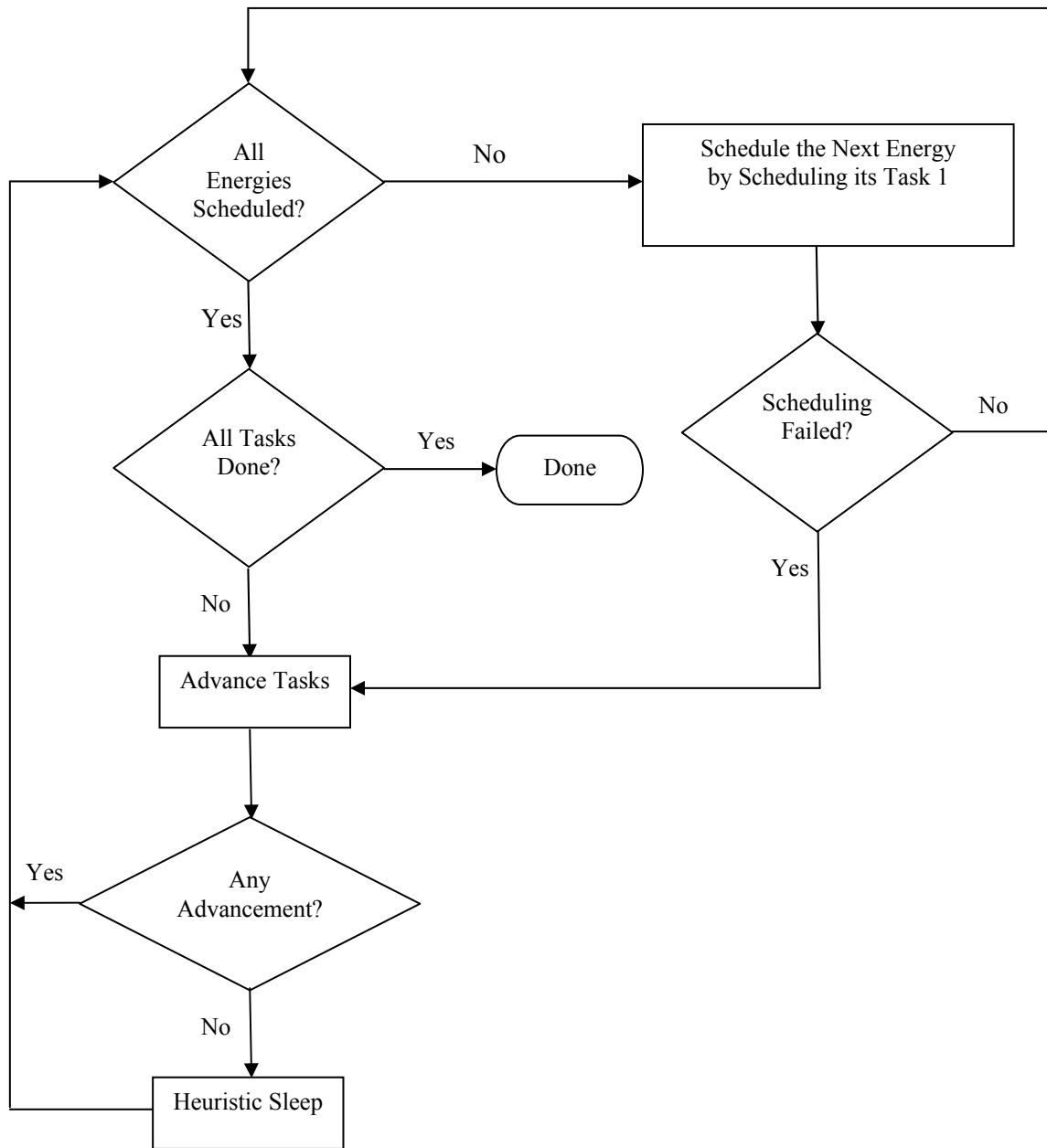


Figure 7B. The sequential strategy for generating a set of polyenergetic projection images over 360 angles. Task 1 of the E_1 initiates on a CPU core at t_0 and finishes at t_1 when Task 2 of E_1 initiates on GPU. At t_2 , Task 2 of E_1 ends and its Task 3 begins. At t_3 , Task 3 of E_1 finishes and Task 1 of E_2 starts on CPU. The rest energies follow the same pattern.



690 **Figure 8:** The dispatcher workflow chart.

The Computation time of DRR generation on GPGPU

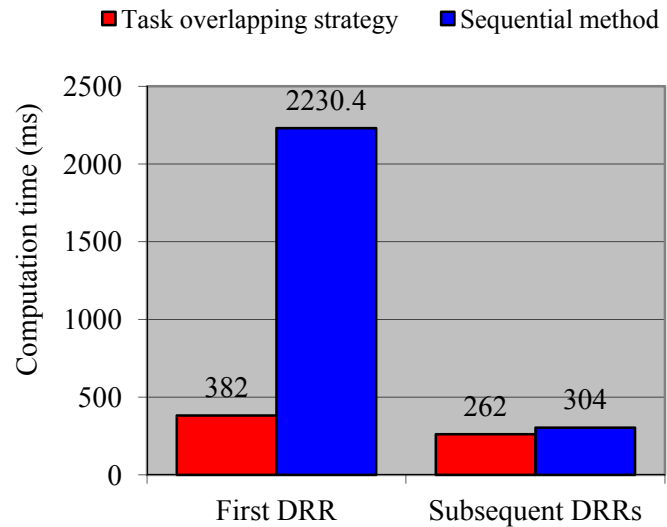


Figure 9A. The comparison of computation times for DRR generation using the task overlapping strategy and the sequential method.

The speedup of DRR generation and line integral

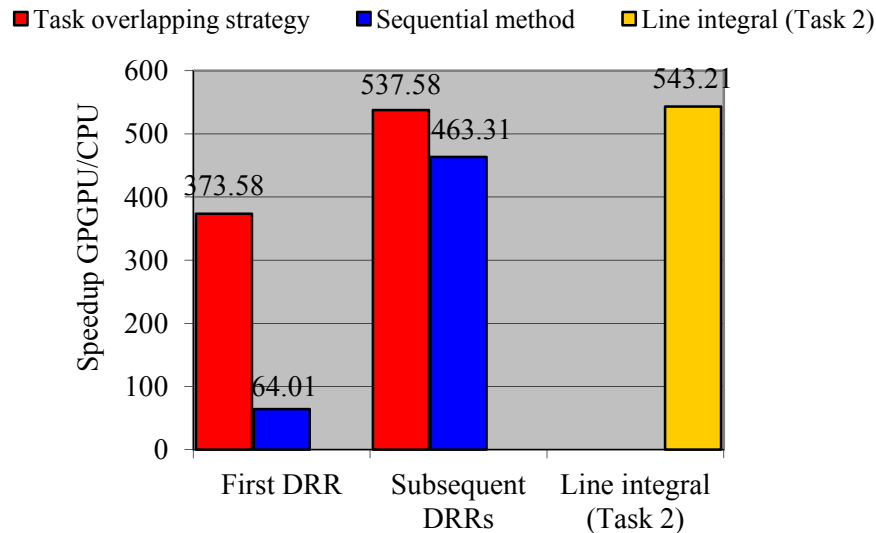


Figure 9B. The speedup for DRR generation and line integral over CPU.

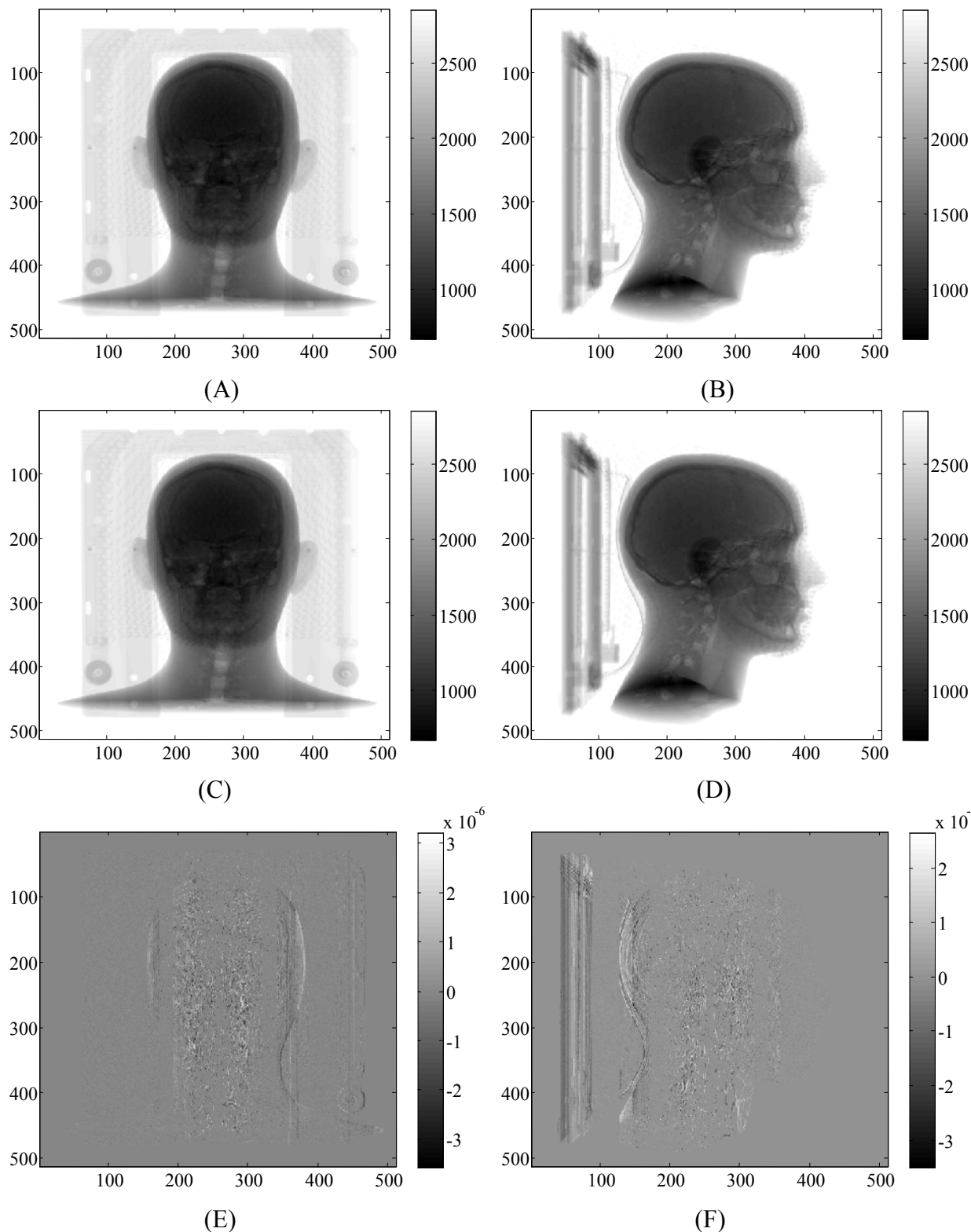


Figure 10. The projections calculated by (A) and (C) CPU-based, and (B) and (D) OpenCL-based GPU implementations. (A) and (B) at 0 degree. (C) and (D) at 90 degree. The relative difference images of (A) and (C) is shown in (E), and the relative difference of (B) and (D) in (F).

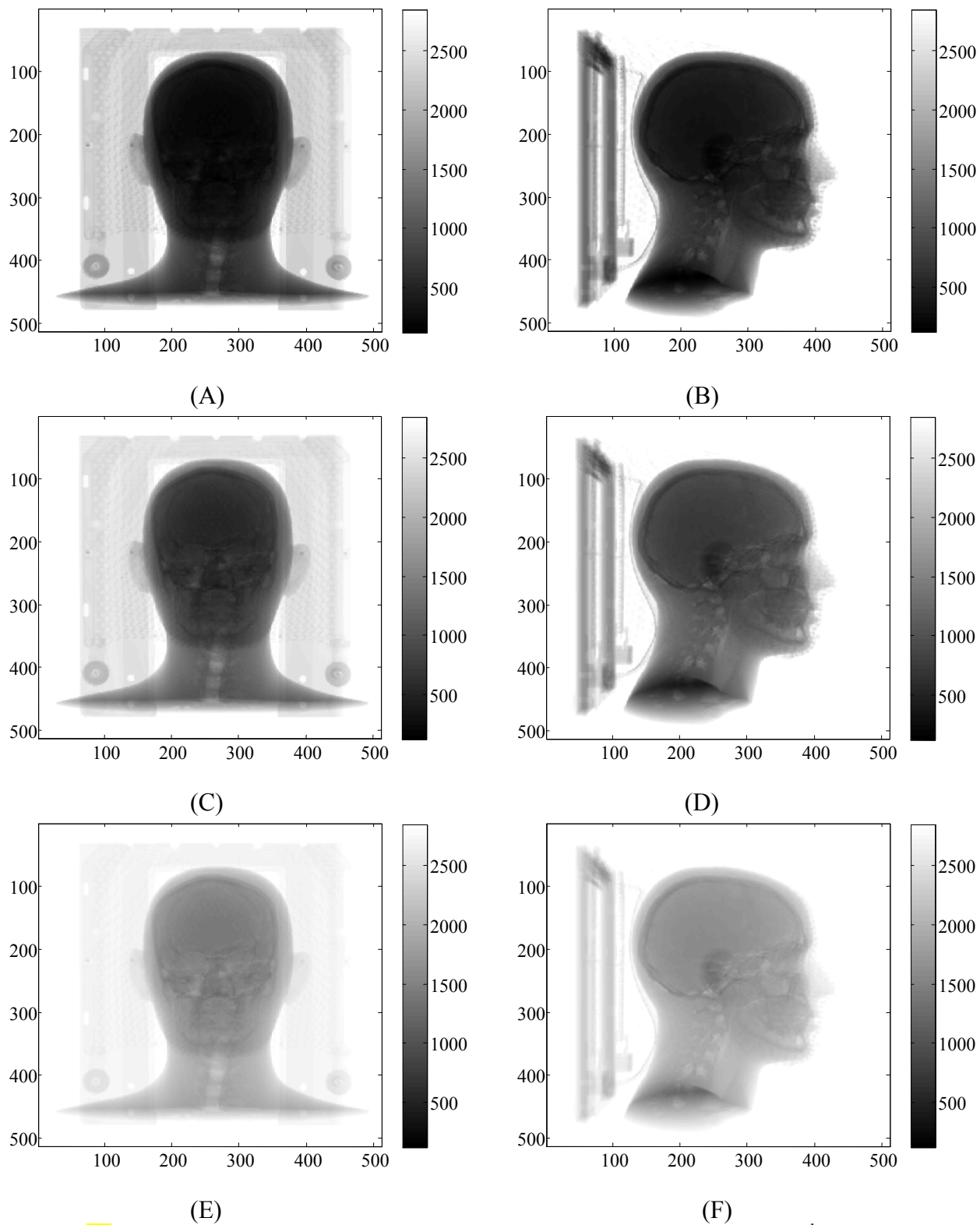


Figure 11. Projection images at 0 degree (the 1st column) and 90 degree (the 2nd column) for (A) and (B) 0.25 MeV, (C) and (D) 0.75 MeV, and (E) and (F) 4.0 MeV.

surrounding area. Finally, the gels were returned to the refrigerator and allowed to solidify for at least 24 hours. The samples were irradiated with 18MV and 250kVp photon beams such that the foils were perpendicular to the beam direction. T2-weighted images were acquired after 24 hours with a 3T-MRI scanner using a turbo spin-echo sequence. Imaging parameters were as follows: field-of-view = 180mm x 180mm, pixel-size = 0.35mm x 0.35mm, and slice-thickness = 5mm. Dose distributions were calculated by using a two-point method from the MR images taken at two echo times (20 and 101 ms). Results: There was no signal from the metal foil allowing ease of identification. All 18MV samples and the 250kVp aluminum sample did not show any appreciable change in the dose distribution. The 250kVp samples for lead and gold, however, had a significant decrease in absorbed dose downstream of the foil. The dose profiles along the beam direction revealed dose reductions of 18% and 16% for lead and gold, respectively. Conclusion: We demonstrated that polymer-gel dosimetry can be used to measure the fine dosimetric structures around a small metallic object although its accuracy still must be assessed.

SU-E-T-337

Monte-Carlo Study of Dose Perturbation Effects in External Beam Therapy of the Prostate Caused by the Presence of Post-Implant Brachytherapy Seeds

R Bassalow^{1*}, A Sabbas¹, M Delamerced¹, S Trichter¹, F Kulidzhanov¹, L Nedialkova¹, D Nori¹, K Chao¹, J Chang¹, (1) NewYork-Presbyterian Hospital/ Weill Cornell Medical College, New York, NY

Purpose: Previously it has been reported that brachytherapy dose distribution can be affected by seed self-attenuation. We investigate the magnitude of dose perturbation in external beam radiation therapy caused by the presence of remaining brachytherapy seeds in the prostate. Methods: A phantom from a patient CT data was generated. A custom Python code was developed to modify the phantom by replacing selected voxels with the Cs-131 seed material and density. 3D dose distributions and mean dose in the volume containing seeds for different seed arrangements were calculated using Monte-Carlo EGSnrc dosxyznrc code and compared to the dose distributions without the seeds for a typical 5-field treatment using 6MV and 18MV beams. Seeds were arranged symmetrically around the isocenter in a rectangular grid pattern with varying number of seeds along the x-, y- and z-axes. In calculating mean dose and dose difference maps, seed voxels were excluded from calculation. Results: Difference in mean dose in the volume containing seeds and the same volume without seeds, was calculated for 6 and 18 MV beams. Mean dose increase is linear with the number of seeds and ranges from 0.7% for 75 seeds to 1.4% for 175 seeds for 6 MV and from 1.8% for 75 seeds to 4.6% for 18 MV for 175 seeds. Conclusions: In the external beam radiotherapy of the prostate, that contains seeds from the previous LDR seed implant, the mean dose in the prostate is increased proportionally to the number of seeds and the external beam energy used.

SU-E-T-338

Percent Depth Dose Comparison Between Measurements From Three Varian Linear Accelerators and Varian AAA Golden Beam Data

G Wu^{1*}, G Courlas², D Lewis³, B Jackson⁴. Northwest Medical Physics Center, Lynnwood, WA

Purpose: To validate the use of Varian Golden Beam Data Percentage Depth Dose (PDD) information for the Eclipse AAA algorithm for newly installed Varian Linear Accelerators Methods: Comparison was made between measured data and Varian Golden Beam Data which is often used in AAA beam models in Eclipse treatment planning systems. Open field and wedge field data were compared for 4 x 4 cm, 10 x 10 cm, 20 x 20 cm, and 30 x 30 cm field sizes for four physical wedges and for two photon energies. Results: Small differences on the order of 1% are observed when comparing measured open field PDD data and PDD data from the AAA Golden Beam Data set. In contrast, larger differences were observed in wedge field percentage depth dose for these data sets with the measured data being greater than AAA data. The difference increases with increasing depth and decreasing field size. For a 4 x 4 cm field with a 15 degree wedge the average difference is 6 % at a 25 cm depth for 6 MV photons. These differences are slightly smaller for 18 MV photon data for most field size and wedge combinations. Conclusions: The Varian Golden Beam wedged field PDD data for photon beams is compiled from older linear accelerators and shows variations from data collected from recently installed machines. This variation could be due to increased beam hardening effect from the wedges compared to previous machines. Therefore, caution should be

applied when using the AAA Golden Beam model for wedged field calculations, particularly for field sizes smaller or equal to 20 x 20 cm and depths deeper than 15cm. It is recommended that carefully collected commissioning data be used for physical wedge PDDs in Eclipse.

SU-E-T-339

Target Change Effect On Surface Dose of Treatment and Imaging Helical Tomotherapy Beams

E Ehler^{1*}, B Gerbi¹, (1) University of Minnesota, Minneapolis, MN

Purpose: The target of the TomoTherapy unit is replaced at regular intervals. This work studies surface dose both before and after a target change for the treatment and imaging beams. Methods: Attix parallel plate chamber, as well as LiF powder thermoluminescent dosimeter (TLD) monolayer measurements were performed on the surface and at depths up to 1.5 cm in solid water before and after the target change. Due to the 1.0 cm diameter collecting volume of the Attix chamber, broad imaging beam measurements were performed with a 5 cm jaw width at isocenter; TLD measurements were performed using the narrow jaw width used for clinical MVCT imaging. Measurements at depths of 10 and 20 cm in solid water were also performed using A1SL cylindrical ionization chambers with a 5 cm field width. Results: Attix chamber measurements in the broad imaging beam showed surface dose versus dose at 5 mm to be constant before ($31.3 \pm 0.6\%$) and after ($31.4 \pm 0.3\%$) the target change. TLD monolayer measurements showed no change in the narrow imaging beam surface dose ($25.0 \pm 0.8\%$ before and $24.6 \pm 0.5\%$ after). The treatment beam showed a small decrease in surface dose after the target change ($18.2 \pm 0.7\%$ before and $17.0 \pm 0.3\%$ after). The ratio of dose at depths of 10 and 20 cm for the imaging beam was 2% greater after the target change whereas the treatment beam ratio was 0.6% greater after the target change as compared to the ratio measured before the target change. Conclusions: Even though degradation of the thin tungsten target occurs with use, little to no change is observed in the surface dose for either the imaging or the treatment beam. This is likely due to a thick, low atomic number metal block located immediately after the target.

SU-E-T-340

Dose Enhancement Due to Backscattered Electrons of Gold Nanoparticle: Size and Shape Dependency Study by Thermoluminescent Dosimetry

T Marques^{1*}, G Barbi², O Baffa¹, P Nicolucci¹, (1) University of São Paulo, Ribeirão Preto, SP, BR, (2) Hospital of Clinics of Ribeirão Preto / USP, Ribeirão Preto, SP, BR

Purpose: Quantify dose enhancement fractions (DEF) caused by backscattered electrons of gold nanoparticles with different size and shape using thermoluminescent dosimeters (TLD). Methods: Gold nanorods (AuNP-rod) of 45nm and spherical gold nanoparticles (AuNP) of 5nm average diameter were used in this study. Fourteen Lithium Fluoride TLDs (LiF-100) groups were pre-calibrated in the 200kV x-ray beam studied. Different mass-fractions of gold (0%, 0.1%, 0.2%, 0.3%, 0.5%, 0.7% and 0.8%) were casted only in one surface of each tablet. An acrylic plate with a small recess properly designed to fit tablets of a same group each time; 10cm of acrylic were also positioned down the TLDs to guarantee backscattering conditions. 2Gy were delivered to all groups. The AuNPs films were down positioned related to the beam incidence during the experiments aiming to measure backscattered electrons of AuNPs. TLDs were positioned in two depths: surface and build-up. DEF was calculated as the ratio between dose measured with TLD tablets with and without AuNP. Results: Experimental DEF varies between 1 and 1.26 to both AuNP-rods and AuNPs when positioned on the surface. At the build-up depth the experimental DEFs found were 1, 1.02, 1.04, 1.09, 1.12, 1.16 and 1.17 respectively to concentrations 0%, 0.1%, 0.2%, 0.3%, 0.5%, 0.7% and 0.8% of AuNP-rods; To the same gold concentrations of spherical nanoparticles the DEFs found were 1, 1.02, 1.02, 1.03, 1.04, 1.08 and 1.11. A linear behavior between gold concentration casted and DEFs measured was observed to both depths of irradiation. Conclusions: Differences of 6% in fractions of dose enhancements can be found when 45nm AuNP-rods and 5nm spherical AuNPs are considered. The angular distribution of scattered electrons in AuNP combined to nanoparticle size and shape implies in its self attenuation inside the nanoparticles and thereof the fractions of dose enhancements around the particles.

image guided system (IGRT). The displacements and angles given by the ExacTrac are analysed. Results: The mean shifts, rotations, and standard deviations were determined, as a measure of the system's accuracy. Average translations measured were 0.4 ± 0.7 mm, -0.9 ± 1.1 mm and 0.6 ± 0.6 mm, respectively, for vertical, longitudinal and lateral directions. The mean deviations take place in the longitudinal direction and usually in the same sense of direction. Conclusions: The system specifications (2 mm in all directions) are fulfilled in most of the analysed cases, however some special patients (those with orientation problems which no cooperate) present important deviations in the longitudinal direction up to 8 mm. Professionals must be aware in these cases, and should use an IGRT verification system.

SU-E-T-581

Correction Factors for Secondary Monitor Unit Calculation in Stereotactic Lung Radiotherapy

A Melancon^{1*}, R Sadagopan¹, (1) MD Anderson Cancer Center, Houston, TX

Purpose: Secondary MU calculation is an important verification step of treatment planning. Use of simple secondary MU program is limited in thoracic SBRT due to inaccurate modeling of the dose in low density medium - lung. The goal of this study was to quantify these inaccuracies and develop correction factors to improve the accuracy of the secondary MU calculation. Methods: We estimated the correction factors to account for the inaccurate modeling of the scatter by the Diamond (K&S) MU verification program by comparing the MU generated by the program to the pinnacle TPS using simulated water phantom with lung heterogeneities. The lung and tumor densities were assigned bulk relative densities of 0.33 and 1.0. Field size and depths of lung and tissue traversed were varied to establish a clear trend. Five patients were selected whose treatment MU calculations deviated by more than 5% and the developed correction factors were applied. Results: Comparison of MU in phantom indicated that the errors due to lack of re-buildup ranged from -5% to -4.0% for 4 cm x 4 cm and -3.3% to -4% for 10 cm x 10 cm. Inaccuracies due to lack of proper forward scatter modeling increased with field sized -5% to -3.0% and in general increased with increasing distance of lung traversed. Application of these correction factors to the five patients' verification results reduced the discrepancy from an average of 8.1% to 6.3%. Conclusion: The most significant correction factors were due to inaccurate modeling due to (lack of sufficient) re-buildup and forward scatter. Correction factors can improve the usefulness of secondary MU program.

SU-E-T-582

Monte-Carlo Study of Dosimetric Effects of Brachytherapy Seeds Presence in Lung External Beam SBRT

R Bassalow^{1*}, S Trichter¹, A Sabbas¹, B Parashar¹, F Kulidzhanov¹, L Nedialkova¹, G Wernicke¹, D Nori¹, K Chao¹, J Chang¹, (1) New York-Presbyterian Hospital/ Weill Cornell Medical College, New York, NY

Purpose: In lung SBRT seeds left from a prior intraoperative brachytherapy may perturb the dose distribution near the target. We investigate the dosimetric effects of seeds present in the beam paths. Methods: BEAMnrc dosxyznrc code was used to generate 3D dose distributions for different seed arrangements using five 6 MV SBRT fields. A custom C++/Python code was developed to assign seeds of variable quantity and configuration to selected voxels with the Cs-131 seed density. Two configurations of seed placement were considered: 1) an "odd" number of seeds per row, with the central column shadowing the isocenter, and 2) an "even" number of seeds per row without the isocenter shadowing. Results: For the "odd" configuration the isocenter dose decreased sharply with the number of seeds shadowing the isocenter (from 1.8% for 1 seed to 13.1% for 11 seeds). Adding more seeds in each row lowered the dose by additional 2.4% and this decrease was almost independent of the number of added seeds. A much smaller dose reduction (<1.8%) is observed for the "even" seed configuration, that does not shadow the isocenter directly. Conclusions: Dose reduction at the isocenter is proportional to the number of seeds that directly shadow the isocenter. Adding seeds in the beam path, without shadowing the isocenter, reduces the dose by a small amount. Since clinically the seeds are arranged in a mix of "odd" and/or "even" configurations with 1-2 rows and 1-2 columns, the isocenter dose is expected to be reduced by 0.6% to 5%.

SU-E-T-583

QA Verifications of RapidArc Type SBRT Treatment Plans

X Song^{*}, N Deb, T Xue, St Luke's Hospital, Bethlehem, PA

Purpose: RapidArc treatments combine features of IMRT and arc treatments. It may be a superior treatment technique for stereotactic body radiation therapy (SBRT) in both improved dose distribution as well as improved patient comfort and reduction in motion due to rapid treatment delivery. This is a study of the QA verification results on 15 spine and 9 lung patients treated with RapidArc SBRT since August 2009. Methods: Treatments were delivered on a Varian Trilogy with RapidArc upgrade. Plans generated used 6 MV photons utilizing Varian Eclipse software. Most plans consisted of a 2 arc technique. The 3D diode array is the Delta4 system from Scandidos. Delta4 has 1069 P type Si diodes on three wings, which are inserted to two planes in a cylindrical PMMA phantom. The three dimensional dose is transferred to the Delta4 by DICOM RT. To minimize the MLC leakage, and to reduce the finite leaf width (0.5 cm) effects, we used collimator angles of 155 and 215 (Varian scale). Fraction dose ranged from 400 cGy to 1800 cGy. For each plan, the planned dose distribution and measured dose distribution are compared by using 2D isodose display, profile comparisons, percentage dose deviation, and DTA and Gamma index. Results: The average percentage of diode with Gamma index (3% dose and 3 mm) 1 or less is 95.5% with standard deviation of 3.4% for spine SBRT plans, and average percentage of diode with Gamma index (3% dose and 3 mm) 1 or less is 97.4% with standard deviation of 2.0% for lung SBRT plans. Conclusions: All measurement results agree well with the dose distribution of all SBRT plans. Delta4 system is a good QA tool for RapidArc type SBRT treatments.

SU-E-T-584

The Accuracy of the Respiratory Motion Tracking with Robotic Radiosurgery System

M INOUE^{1*}, H Shiomi², K Okawa³, M Senda⁴, K Inada⁵, T Koshi⁶, N Yokota⁷, H Iwata⁸, K Sato⁹, (1) Yokohama CyberKnife Center, Yokohama, JP, (2) Osaka University Graduate School of Medicine, Suita, JP, (3) Yokohama CyberKnife center, Yokohama, JP, (4) Yokohama CyberKnife center, Yokohama, JP, (5) Yokohama CyberKnife center, Yokohama, JP, (6) Yokohama CyberKnife center, Yokohama, JP, (7) Yokohama CyberKnife center, Yokohama, JP, (8) Nagoya City University Graduate School of Medical Sciences, Nagoya, JP, (9) Japanese Red Cross Medical Center, Shibuya-ku, JP

Purpose: To evaluate the accuracy of the respiratory motion tracking system of the CyberKnife by Beam's eye view images from CCD camera. Methods: The ball, 20.1 mm in diameter, in which gold marker was placed was used as a target. Using a dynamic motion phantom, it moved based on motion either of data sets from a sine curve or irregular patterns of respiration that came from two patients, both of which had 1 cm amplitude. Treatment planning was based on a static CT scan using standard parameters for CyberKnife treatment, and all of the beams in the plan aimed center of the ball. Beam's eye view images were recorded with a CCD camera mounted on a linac head which was tracking the ball. The errors from displacement between the CCD camera's central axis and center of the ball were measured by fifteen times per second, with self-developed software. Results: In the case of the motion by the sine curve, errors were 2mm or less at 99% of the tracking time. In the case of the respiratory irregular motion, errors were 3mm or less in 99% of the tracking time. However, more than 5 mm errors were momentarily detected. Conclusions: We developed a method to measure statistically the error of the respiratory motion tracking. In this experiment, it was very small; however, larger errors were observed in irregular motion, comparing with regular motion with the same amplitude. The reason is the respiratory motion tracking system uses the algorithm based on prediction of the future target position using past pattern of motion. Thus, PTV margin may be set for each patient individually.

SU-E-T-585

A Dosimetric Analysis of Cranial Stereo-Tactic Radio Surgery Plans Treated by Gamma Knife

a pendse^{1*}, (1) P.D.Hinduja Hospital, MUMBAI, MAHARASHTRA, IN

Purpose: : To quantify the impact of dose planning using different clinically important parameters such as volume conformity index (VCI), appropriateness of target volume(ATV), conformity gradient index(CGI), integral dose (ID), by categorizing size of tumor volume(TV) in small,

SU-E-J-07**A Preliminary Study On Optimal Dose-Allocation Parameters for Low-Dose Cone-Beam CT**

Z Zhang*, X Han, E Pearson, J Bian, E Sidky, C Pelizzari, X Pan, University of Chicago, Chicago, IL

Purpose: Cone-beam CT (CBCT) is widely used for providing image guidance in radiotherapy and interventional procedures. Due to the patient safety concern involved in repetitive CBCT scans, significant effort has been devoted to possibly lowering imaging dose in CBCT. For a given total dose, it is also important to investigate how image quality can be affected by dose allocations over projection views and by image-reconstruction algorithms. In this work, we investigate quantitatively how image quality changes resulted from different combinations of dose-allocation parameters and some existing reconstruction algorithms. **Methods:** We performed simulation studies by using a numerical phantom containing structures of different contrast levels. We also acquired real data of a Catphan phantom (The Phantom Laboratory, Salem, NY) by using the on-board imaging system (Varian Medical Systems, Palo Alto, CA). At three different total dose levels, we allocated each of them to different numbers of views ranging from 120 to 650. For each allocation scheme we applied the FDK and ASD-POCS algorithms to obtain reconstructed images. A set of quantitative metrics were used to evaluate image quality based on relevant tasks. **Results:** Preliminary results showed that for total dose levels under study, both FDK and ASD-POCS algorithms yield images with comparable quality when a large number of views are considered and that images reconstructed by the ASD-POCS from smaller number of views generally exhibit higher quality. Overall, for each given total dose level the ASD-POCS algorithm yields images of comparable or higher quality than does the FDK algorithm. **Conclusions:** We demonstrated that CBCT image quality can be optimized for a fixed total dose by choosing an appropriate combination of dose-allocation parameters and reconstruction algorithm. This finding may potentially be used for improving current CBCT image quality and for designing innovative, low-dose CBCT imaging protocols.

SU-E-J-08**Research the Feasibility of High Dose Radiotherapy for Brain Metastases Guided by the Contrasted Cone Beam CT**

G Gong^{1*}, Y Yin², T Liu³, J Chen⁴, J Lu⁵, C Ma⁶, (1) Shandong Cancer Hospital and Institute, Jinan, Shandong, CN, (2), jinan, CN, (3) Shandong Cancer Hospital and Institute, Jinan, Shandong, CN, (4) Shandong Cancer Hospital and Institute, Jinan, Shandong, CN, (5) Shandong Cancer Hospital and Institute, Jinan, Shandong, CN, (6) Shandong Cancer Hospital and Institute, Jinan, Shandong, CN

Purpose: To research the feasibility of high dose radiotherapy for brain metastases guided by the contrasted cone beam CT through studying how to implement and improve the contrasted cone-beam CT scanning and image registration in the progress of CBCT guided brain metastasis radiotherapy. **Methods:** 8 brain metastases cases were selected (lung cancer 3cases, liver cancer 1 cases, breast cancer 2 cases and nasopharyngeal carcinoma 2 cases), and achieved the CBCT scanning, in 20 minutes, 30 minutes, 40 minutes after contrasted stimulation CT scanning. Analyzed the CBCT image quality and the demonstration capability of the tumor on CBCT images comparing with the simulation CT. Radiotherapy plans were designed quickly with the Prescription dose 5Gy/fraction and the image registration work were completed online, and analyze the potential role of the contrasted CBCT in radiotherapy for brain metastasis. **Results:** The contrasted CBCT could improve the image resolution, the tumor area and the location relationship between tumor and normal brain tissue were showed clearly. The demonstration capability of tumor on CBCT in 30 minutes was bigger than in 20 minutes and 40 minutes. The setup errors were 3.0 ± 0.8 mm in z-axial, 2.8 ± 0.6 mm in y-axial and 2.0 ± 0.5 mm in x-axial. **Conclusions:** The contrasted CBCT image can display the tumor and location relationship between tumor and normal tissue clearly, it can exhibit the result of adjustment for setup error directly, it could become an effective way to ensure the security in high dose radiotherapy for brain metastases.

SU-E-J-09**Feasibility Study of Volumetric Imaging in Cyberknife Room Using Scanning Beam X-Ray Sources**

T Li*, X Li, Y Yang, D Heron, M Huq, University of Pittsburgh Medical Center, Pittsburgh, PA

Purpose: Image guidance system such as the one used in Cyberknife or Brainlab ExacTrac, utilizes two x-ray sources underground, which generates a pair of 2D orthogonal images for target localization. This work investigates the feasibility of bringing 3D or 4D imaging into such environment. **Methods:** The x-ray sources in a Cyberknife room are replaced with scanning x-ray tubes, in which an electron beam is electromagnetically scanned across a 25cm x 25cm transmission target located behind a collimator. The collimator restricts the emerging x-ray photons to those directed towards the detector. The system is simulated to generate a series of orthogonal 2D projections, and a fully 3D reconstruction algorithm is developed using the total variation (TV) technique. Parameters such as the source-to-axis distance, the source-to-detector distance, the electron beam scanning pitch, and the detector resolution are varied to study their impacts on the image quality. **Results:** As the electron beam scanning across the transmission target, a moving x-ray source is formulated. With as few as 25 paired projections, a 3D image can be reconstructed. It is found that the image quality increases to a certain degree when finer scanning pitch is used. The image quality also increases as the distance between the x-ray source and the isocenter decreases, significantly, however the field of view (FOV) is reduced. The maximum FOV is about 16 cm under current setup. Using high detector resolution can also improve the image quality. **Conclusions:** With scanning beam technology, it is possible to obtain volumetric images for fixed x-ray imaging systems (i.e. without gantry moving). The image quality is comparable to the current on-board cone-beam CT used in the treatment room, however the FOV is limited and the image reconstruction time is relatively long.

SU-E-J-10**Panoramic Cone Beam Computed Tomography (CBCT)**

J Chang*, L Zhou, KSC Chao, NewYork-Presbyterian Hospital/Weill Cornell Medical College, New York, NY

Purpose: Cone-beam computed tomography (CBCT) is the main imaging tool for image-guided radiotherapy but its functionalities is limited by small imaging volume and restricted image position (imaged at the central instead of treatment position for lateral targets to avoid collisions). In this paper we present the concept of "panoramic CBCT" which can image patients at the treatment position with a volume as large as practically needed. **Methods:** This novel "panoramic CBCT" technique scans the target panoramically for different imager positions, stitch together the panoramic projection images of the same gantry angle to form a larger projection image, and perform CBCT reconstruction using the stitched projection images. To study the potential reconstruction artifacts of this imaging technique, we calculated cone-beam projections of the MCAT thorax phantom for one imager in three adjacent positions. Different gaps and exposure levels were introduced between adjacent imager positions to simulate imperfect stitching. Simultaneous algebraic reconstruction technique (SART) was used to reconstruct CBCT images using the stitched projection images for half-scan (180-degree+cone-angle/2 gantry rotation). As a gold standard, CBCT reconstruction using projection images big enough to encompass the target were also performed for full scan (360-degree gantry rotation). **Results:** Incomplete reconstruction with artifacts was observed for reconstruction using projections from the central imager position only. When stitching is perfect, complete reconstruction was obtained from the stitched projection images with quality similar to the gold standard. Streak and ring artifacts were observed when stitching is imperfect and the severity of artifacts increases with the gap size and exposure level difference. **Conclusions:** Since half-scan can be achieved for most treatment positions without collisions, the proposed "panoramic CBCT" can image tumors of any location for patients of any size at the treatment position. Good image stitching algorithms are needed to eliminate the reconstruction artifacts from imperfect stitching.

lowest for the most part, however, since larger margins were utilized for proton planning more investigation is required. On average, the dose to critical structures, normal brain, and integral dose was smallest for IMPT, followed by DS, and largest for IMRT. Conclusion: Preliminary data indicates that dose to critical structures, integral dose, and the dose to normal brain is reduced with proton therapy; therefore implying merit in this modality. This dose sparing is crucial because of the high sensitivity of normal tissues for very young patients.

SU-E-T-496

Dosimetric Comparison Between Protons and Photons in the Field Junction in Craniospinal Irradiation (CSI)

C Cheng^{1, 2*}, S Srivastava^{2, 3}, J Buchsbaum^{1, 2}, L Zhao^{1, 2}, M Wolanski^{1, 2}, J Simmons¹, P Johnstone^{1, 2}, I Das^{1, 2}, (1) Indiana University Health Proton Therapy Center, Bloomington, IN, (2) Indiana University School of Medicine, Indianapolis, IN, (3) Reid Hospital & Health Care Service, Richmond, IN

Purpose: In this study, we investigated the dosimetry in the moving gap region in proton CSI for various combinations of field junction widths and feathering step sizes. We have also compared the dosimetry in the field junction between proton and photon beams. Methods: Dose profiles for two proton ranges, 11.6cm and 16cm, both with 10cm SOB for the 30cm snout are used. Feathering of the junction is simulated by shifting the profiles by two successive steps. Three junction widths (0, 2, 4mm) and two feathering step sizes (5, 10 mm) are investigated. Similar simulations (but also include larger gap widths due to larger penumbra) are performed for 6 and 15 MV x-rays. Dose profiles at the field junctions are then compared for the proton and photon fields for various gaps and feathering step sizes. Results: For protons, full dose is achieved in the field junction for 0mm gap for both 5mm and 10mm featherings. However, with even a 2mm gap, the dose falls to below 90% in the moving gap due to the steep proton penumbra. For photons, even 4mm gap still results in >90% dose in the moving gap due to the large penumbra and the 'tail' in the profiles. Despite the different dose characteristics, it is possible to produce similar dose profiles in the moving gap for proton and photon fields by varying the gap and the feathering sizes for photon fields. Conclusion: Full dose can be safely achieved in the junction by 'hot-matching' the spine and the brain fields in proton CSI and feathering the junctions. The steep proton penumbra results in a large dose gradient even with 2mm gap between fields. It is possible to produce similar dosimetry in the junction with photon CSI. The difference is that there is no exit dose with protons.

SU-E-T-497

Experience in Prone Breast Setup Accuracy Improvement

F Kulidzhyanov*, A Sabbas, J Chang, S Trichter, M Hayes, G Wernicke, D Nori, K Chao, New York - Presbyterian Hospital, Weill Cornell Medical Ctr, New York, NY

Purpose: Quality Improvement of prone breast radiotherapy by modification of the simulation technique and a prone breast board (PBB). Methods: The "Horizon" PBB medial edge of the bridge was elevated and marked with radio-opaque BBs to avoid the bolus effect from the bridge and visualize the edge during simulation and treatment setup. Side bars were added to stabilize PBB. For support of the hands, shoulders and clavicles the superior platform was widened and elongated also indexed handles and shoulder support were installed. Head support was used for patient's longitudinal setup. A "two-step" setup procedure was introduced to improve the setup accuracy: the patient is setup on the board using the "setup" point that is easily and reliably identified on patient body and then shifted to the treatment isocenter based on the treatment planning calculation. Results: Implementation of the "two-step" setup procedure and modification of PBB significantly improved the setup accuracy. 74 patients were treated with this technique: 20% has a displacement (beam relative to the marked edge) of more than 1cm, 9.5% between 1cm and 0.5cm, and the rest 70.5% less than 0.5cm. Displacements more than 1cm mostly happened at the beginning of the implementation this procedure and there was a general trend of decreasing displacement as we became more familiar with this setup technique. The radio-opaque markers made it much easier to identify and avoid unexpected inclusion of the bridge in the treatment fields during the treatment planning and patient setup. Conclusions: There are currently no commercially available PBB that are durable, comfortable and flexible for satisfactory patient setup and alignment. The modification of the prone breast board and implementation of the new simulation technique have

partially addressed these concerns and significantly improved the quality of our prone breast RT program

SU-E-T-498

Comparison of Inter-Fraction Setup Uncertainty of Two Commercially-Available, Cranial Immobilization Masks Using KV-CBCT and ExacTrac® Imaging Systems

N Nayeibi^{1*}, A Gutierrez², N Papanikolaou³, University of Texas HSC SA, San Antonio, TX

Purpose: The 3-point thermoplastic Orfit mask and BrainLAB stereotactic mask provide immobilization of the head in fractionated radiotherapy. The purpose of this study was to compare the setup accuracy of these two masks using pre-treatment kV-CBCT and ExacTrac®. Methods: Both BrainLab and Orfit masks are currently used in our institution. The BrainLab mask is a two-part masking system custom fitted to the front and back of the patient's head. This mask is used in conjunction with the ExacTrac-based patient positioning. The Orfit 3-point mask is shaped to the patient's head similarly but also encompassing the superior aspect of the head. As part of our current setup procedure for patients immobilized by Orfit mask, daily portal images and weekly kV-CBCT image sets are acquired pre-treatment. In this study, kV-CBCT data from 6 Orfit patients (122 fractions) fixated with the Orfit mask and ExacTrac data from 11 patients (153 fractions) immobilized by the BrainLab mask were retrospectively analyzed. Daily patient positioning was evaluated as the translations between the pre-treatment and reference image after fusion registration. Results: The mean inter-fraction displacements in 3D were 2.7 ± 1.4 mm (max=6.4mm) and 3.3 ± 1.8 mm (max=7.9mm) for Orfit and BrainLab groups, respectively. The mean displacement and systematic setup uncertainty for the Orfit patients were -0.3 ± 1.0 , -1.0 ± 1.4 , and -1.0 ± 1.3 mm in the lateral, superior-inferior and anterior-posterior directions, respectively. For the BrainLab patients, the mean and systematic setup uncertainties were 0.2 ± 0.8 , -1.3 ± 1.8 , and -0.9 ± 2.5 mm in the lateral, anterior-posterior and superior-inferior directions, respectively. Conclusions: Both masks showed comparable performance in term of setup uncertainty. Daily image guidance is recommended with either immobilization system to optimize the accuracy of setup.

SU-E-T-499

Assessment of Patient Setup Accuracy at a Treatment Position After the Patient Has Been Registered at Another Location Using Robotic Positioner and a Dual KV Imaging System

A Ghebremedhin*, N Wang, B Patyal, Loma Linda University Medical Center, Loma Linda, CA

Purpose: We use cardinal angle and beam eye view images with DRRs to register a patient at every treatment position. This process is time consuming; moreover, every treatment position is not amenable to imaging. This study is to assess the combined robotic positioner and gantry movement accuracy at a treatment position relative to zero yaw image registration so that additional imaging at the new location can be avoided. Methods: A Styrofoam phantom 30 cm x 30 cm x 30 cm with beekleys embedded in such a way that they could easily be distinguished on a DRR. The phantom was CT scanned with a 2.5 mm slice thickness and a 50 cm field of view. Treatment planning DRRs were created at numerous table and gantry angles. The phantom was subsequently set up in the treatment room with both table yaw and gantry at zero. The table was loaded with 200 lb weight in order to replicate a typical patient. Image registration was carried out using cardinal angle images and the DRRs. The robotic positioner and gantry were then moved to a new treatment position. The accuracy of the move was evaluated using the beam eye view image, the orthogonal images at the new position and the DRRs for this location. The process was repeated for numerous table and gantry positions as predetermined during treatment planning. Results: The accuracy was found better than a 1.0 mm for all moves except near treatment position with table yaw 90o and Gantry angle between 180o to 270o, where the accuracy was still better than 1.7 mm. Conclusions: As such, the system can be clinically used for patient registration, but we are in the process of further improving the setup accuracy for all clinically relevant robotic positioner and gantry movements without additional imaging.

real-time for each field using an EPID in cine mode. The dose distribution was recalculated based on geometrical information obtained from the cine images. Results: It was observed that the volume of PTVconv is 16% smaller than PTV4D. Subsequently the SBRT plan using PTVconv provides suboptimal dose coverage to the tumor than PTV4D. The V100 of PTV4D decreased from 95% to 82% and D95 of ITV decreased from 47Gy to 42Gy. The cine EPID images have confirmed tumor excursion with respiratory motion is within the predefined ITV boundary. However if the plan is based on apertures designed using PTVconv, there could be geometrical misses resulting in target under dosage. Conclusion: It is recommended to perform 4D CT and use PTV4D for treatment planning for SBRT lung cancer.

SU-E-T-572

Dose Mass Histogram (DMH) Versus Dose Volume Histogram (DVH) for SBRT and Craniospinal Patients: What Can We Learn?

M Chao¹*, X Chen¹, J Penagaricano¹, E Moros¹, V Ratanatharathorn¹, P Corry¹, (1) University of Arkansas Medical Sciences, Little Rock, AR

Purpose: Dose volume histogram (DVH) has been a valuable tool for plan evaluation, but it provides limited information for dose assessment of irradiated tumors and organs, especially for those with significant density heterogeneities such as lungs. DVH is also at odds with the fact that radiation dose is defined as energy deposited in a unit mass of medium irradiated. In this study, dose mass histograms (DMH) were used to evaluate plans from patients treated with stereotactic body radiotherapy (SBRT) and craniospinal axis irradiation (CSAI). Methods: Eight patients were enrolled in the study, of which four of them were treated with SBRT using a BrainLAB system and the other half were CSAI patients treated with a Helical Tomotherapy unit. DMHs for these patients were computed based on the treatment plan's DVHs by weighting each voxel volume according to its density as derived from the CT number vs. density table used in the treatment planning system. All eight plans were exported to a personal computer for DMH computation and analysis. Comparison between each patient's DVH and DMH for planning target volume (PTV) and organs at risk (OAR) were performed. Results: DMH was generated for the PTV and OARs. No significant difference between DMH and DVH was observed for PTV and OARs (heart, kidneys, spinal cord) except for lungs. Lung DMHs from SBRT patients indicated potential room of dose escalation while those from CSAI patients showed the opposite. Conclusions: Dose mass histogram serves as an important tool for evaluation of treatment plans for organs with variable densities. For organs with uniform density distribution, DMHs were not significantly different than DVHs. The potential usefulness of DMH for plan evaluation for organs of heterogeneous density distributions warrants further study.

SU-E-T-573

Monte Carlo Simulated Peripheral Doses in SRS of the Brain

G Georgiev¹*, S Jang¹, R Hamilton¹, (1) University of Arizona, Tucson, AZ

Purpose: In arc based brain Stereotactic Radiation Surgery (SRS), a major concern is the accuracy of the peripheral doses to organs close to the treated lesions. This concern is more pronounced when planning software utilizes Pencil Beam algorithm. To evaluate the out-of-target radiation doses to Organs At Risk (OAR) the predicted organ doses by BrainLab Treatment Planning System (TPS) were compared with doses acquired by a Monte Carlo simulation. Methods and Materials: An arc based brain SRS treatment plan was developed in BrainLab® TPS to be treated on the Novalis® Varian linear accelerator, using 6 MV photon arcs with a 20 mm cone. The doses to different points of interest, representing major OAR were investigated. The photon spectrum in air for 20 mm cone at 100 SSD was designed and verified for the simulation with EGSnrc Monte Carlo particle transport code (DOSRZnrc user code). The resulting Percent Depth Dose (PDD) and dose profile at 75 mm depth were confirmed with respective measurements in a water phantom. Each arc will be approximated by summing simulated discrete angled beams following the arc path and accounting for the difference of their depths to the target. The doses of both calculations will be normalized to an ion chamber measurement at the isocenter. Results: The greatest difference in the PDD was less than 1%. MC simulated profile at 75 mm depth appeared to be less than 1mm wider than the measured data in the penumbra region. Conclusions: A method for simulating peripheral doses in SRS was developed. The agreement in the measured and simulated PDD and profile provide a basis for successfully utilizing this method and comparing the calculated peripheral doses by the TPS and the simulated doses by the Monte Carlo technique.

SU-E-T-574

Assessment of Target Motion in SBRT Lung Patients Using the Frame-Based Stereotactic Coordinates

A Sabbas^{*}, F Kulidzhyanov, S Trichter, R Bassalow, B Biritz, B Parashar, D Nori, K S Chao, J Chang, New York Presbyterian Hospital /Weill Cornell Medical Ctr, New York, NY

Purpose: To assess target movement for SBRT patients receiving hypofractionated radiation for lung. Knowledge of the magnitude of these movements can determine optimal margins around the GTV. Methods: We use the Elekta stereotactic body frame (SBF) to deliver an average of four fractions to lesions of diameter less than 4 cm. The SBF is an effective immobilizer utilizing a vacuum bag that conforms to the body. A patient is set up reproducibly in the SBF using its laser pointers. Its fiducial marks are used to stereotactically localize the target. The SBF's stereotactic coordinates are then used to set up the target to isocenter. We obtain a verification CT prior to each fraction for localization of the target. To quantify target movement, we have recorded its deviation from its initial position based on the treatment planning CT. We have then averaged these deviations over the number of fractions to obtain a mean deviation and its standard deviation per patient for each of the three directions. Results: For 35 patients that have received SBRT for lung lesions, we have calculated the weighted mean, the error of the mean and the sample standard deviation for the three stereotactic coordinates, Lateral, AP and Longitudinal of the centroid of the GTV that was outlined by the same physician on each of the verification CT's. The means are: -3.16 +/- 0.1, 1.27 +/- 0.09 and 0.66 +/- 0.31 mm. The sample standard deviations are: 4.33, 4.35 and 4.24 mm. Conclusions: Internal target motion is the main contributor to its positional uncertainty for our SBRT setup. Assuming a normal parent distribution of the deviations, a uniform margin of 1 cm will provide sufficient coverage of the target for 98% of the times. This is confirmed by the actual distribution of our sample.

SU-E-T-575

Comparison of Total Scatter Factor for SRS Measured by Various Detectors

k Fukata^{*}, S Sugimoto, S Ozawa, T Furuya, M Kawashima, T Inoue, C Toramatsu, K Karasawa, K Sasai, Juntendo University Graduate School of Medicine, Tokyo, JP

Purpose: Total scatter factor is one of the most important parameters in commissioning for stereotactic radiosurgery. We compared total scatter factors which were measured by various detectors. Methods: We attached circular collimators (7.5mm, 10.0mm, 12.5mm, 15.0mm, 17.5mm, 20.0mm, 25.0mm and 30mm diameters at isocenter) for stereotactic radiosurgery (BrainLAB) to Varian Clinac 21EX and irradiated 400MU of 10MV (600MU/min) to the detectors at 3cm depth in the water or water equivalent phantom. Total scatter factor was measured by PinPoint 3D chamber (PTW31016), diode detectors (Edge detector (Sun Nuclear), SFD (iba)) and GAFCHROMIC Film EBT2 (ISP). Data were analyzed using MATLAB (MathWorks). Results: We obtained total scatter factors of 0.74 (Edge detector), 0.71 (SFD), 0.67(EBT2), 0.62 (PinPoint 3D Chamber) in 7.5mm diameter collimator. These scatter factors were normalized by largest collimator (30mm) reading of each detector. For the decision of total scatter factors, we normalized these values by 15mm diameter collimator, and averaged diode detectors and EBT2 less than 15mm. We adopted PinPoint 3D chamber's data for 15mm and over. Conclusions: To obtain total scatter factor precisely, we need to take a measurement with various detectors and evaluate the results carefully. As the next step, we are preparing for Monte Carlo simulation to compare with measured data.

SU-E-T-576

A Comprehensive Approach for SBRT Irradiation On RPC Spine Phantom

Z Su¹*, Z Zhao², T Zhao³, Z Li⁴, (1) University of Florida, Jacksonville, FL, (2) University of Florida, Jacksonville, FL, (3) University of Florida, Jacksonville, FL, (4) University of Florida, Jacksonville, FL

Purpose: To evaluate the entire spine SBRT process and perform comprehensive quality assurance (QA) for RPC Spine Phantom irradiation. Methods: A RPC spine phantom was obtained for RTOG0631 protocol credentialing. A 7 beam, 6MV photon, step-and-shoot IMRT treatment plan was generated using Pinnacle3 treatment planning system (TPS). Total 6Gy

WEDNESDAY, AUGUST 3

Therapy Educational Course **Room 224** **Implanted Target Surrogates for Radiation Treatment Verification**

WE-A-224-01

Educational Course Therapy: Implanted Target Surrogates for Radiation Treatment Verification

Z Wang^{1*}, N Kothary², (1) Duke University Medical Center, Durham, NC, (2) Stanford University Medical Center, Palo Alto, CA

Target surrogates have been extensively used in radiation therapy, especially imaging guided radiation therapy and radiosurgery, for the purposes of target localization and treatment verification. A wide variety of surrogates have been used including gold markers (seeds or coils), surgical clips, long-lasting contrast agents, brachytherapy seeds, and electro-magnetic markers. This course will review different types of applications of target surrogates in radiation therapy and discuss the issues related to marker implantation, such as patient complication, marker migration, dropping, deformation, minimum numbers of fiducials, and timing between the implantation and planning imaging acquisition. Application for specific treatment sites, such as prostate, lung, liver, pancreas, and breast will be addressed. Issues related to image guidance techniques with target surrogates will be discussed. Planning target volume (PTV) margin requirements for implanted marker guided setup will be discussed for each individual site. Marker applications in verifying the accuracy of respiratory gated treatments will also be discussed. Quality assurance with respects to marker stability during the whole course of radiation therapy, deformability with specific implantation sites, and geometrical accuracy will be addressed.

Learning objectives:

1. Attendees will learn how to assess the quality of marker placement.
2. Attendees will learn how to set up QA programs for treatment with implanted target surrogates.

Therapy Educational Course **Ballroom A** **Commissioning and Implementation of New Equipment or Treatment Paradigms**

WE-A-BRA-01

Commissioning and Implementation of New Equipment Or Treatment Paradigms

J Soen^{1*}, M Pankuch^{2*}, (1) Advocate Christ Medical Center, Oak Lawn, IL, (2) CDH Procure Proton Therapy Center, Warrenville, IL

A fundamental responsibility of the Clinical Medical Physics is to assist in the project management and commissioning of new equipment. The undertaking of such responsibilities may appear overwhelming when added to the routine clinical physics responsibilities of an operational center. In addition, the unique challenge of effective implementation requires extensive collaborative efforts from the entire staff, including physicians, therapists, nursing and administration. Methods for successful cooperation typically fall outside the realm of formal training programs. It is the responsibility of the onsite medical physicist to first understand the functionality, the capabilities, and the limitation of their new equipment and then to productively pass this information along to the clinical staff.

Several simple strategies can be considered before, during and after the commissioning duties. These include creating a clear, well defined plan with transparent expectations of the physicians, the clinical staff and administration. While this is obvious, it is not always clear how this is accomplished and what pitfalls one may encounter in the process. A new modality often requires the use of the latest, possibly less familiar tools. The physicist must ensure proper access and appropriate training for these tools often leading to unanticipated problems and unfamiliar results. A key component is to realistically estimate the amount of time it will require and to communicate that to the whole team. A comprehensive awareness of the complete system by entire planning team must be a fundamental beginning product of the project and should be permitted to be flexible enough to process unexpected complications exposed in the commissioning process.

The use of these tactics will be discussed in two clinical cases: 1) The implementation of 4-D CT in a proton therapy environment and 2) the commissioning of an Elekta accelerator for both CMS-XIO and CMS Monaco. While specific vendors will be used in the examples, the tactics discussed will be generally applicable to any vendor or equipment.

Learning Objective:

1. Understand basic strategies, processes and techniques employed in safe and effective execution of a project plan.
2. Examine the described strategies used by the speakers in two actual clinical examples.
3. Understand organizational issues that one may have to address prior to and during the commissioning and implementation of new equipment.

Therapy Scientific Session **Ballroom B** **Brachytherapy and Radionuclide Therapy**

WE-A-BRB-01

Accurate Dosimetric Characterization of a Fully Loaded 20 Mm COMS I-125 Eye Plaque Using Specially Designed GAFCHROMICTM Film

S Trichter^{1*}, S Chiu-Tsao², M Zaider³, A Sabbas¹, F Kulidzhianov¹, J Chang¹, G Cohen³, D Nori¹, K Chao¹, (1) New York - Presbyterian Hospital, Weill Cornell Medical Ctr, New York, NY, (2) Quality MediPhys LLC, Denville, NJ, (3) Memorial Sloan-Kettering Cancer Ctr., New York, NY

Purpose: The majority of eye plaques used in the U.S. are of Collaborative Ocular Melanoma Study (COMS) design with I-125 brachytherapy seeds. Treatment planning is usually done using the TG-43 formalism, not accounting for the gold alloy backing and Silastic insert, which significantly reduce the dose, as calculated by BrachyDose Monte Carlo (MC) (www.physics.carleton.ca/clrp/eye_plaque/). Dosimetric characterization of a fully loaded 20 mm COMS plaque using radiochromic film is reported. Methods: A 20 mm COMS eye plaque was uniformly loaded with 24 6711 I-125 seeds at 6.75 U/seed. Measurements were performed using specially designed single layer GAFCHROMIC EBT1 film sandwiched perpendicular to the plaque's central axis at depths 0 – 19 mm between inserts of a Solid Water "eye" phantom located at the center of a 30x30x30 cm³ full scatter Solid Water phantom. The films were calibrated using a 6711 I-125 seed in Solid Water, applying the TG-43 formalism. Results: Dose distributions in planes perpendicular to the central axis of the plaque are radially isotropic and uniform. Measured depth dose on central axis as well as off-axis profiles, agree well with the results of MC. At 3 mm from the inner sclera, the measured dose rate is 12.5% lower than TG-43 dose rate in homogenous water, similar to 11.9% for MC. The thin flexible film enabled measurements of the dose at the surface of the plaque. Results on duplicate films agree within 5.5%. Conclusions: GAFCHROMIC film in a Solid Water phantom is a convenient, accurate, and reproducible dosimeter for I-125 eye plaque dosimetry. Dose measurements on the inner surface of the plaque enable precise assessment of the scleral dose and its homogeneity, and of the active area of the plaque for coverage determination. This work validates the MC simulations about the dose reduction effect by the plaque's backing and insert.

In-Kind support of materials provided by Oncura, Inc., Arlington Heights, IL and by International Specialty Products, Inc., Wayne, NJ

WE-A-BRB-02

Gold Nanoparticle-Aided Brachytherapy with Vascular Dose Painting: Estimation of Dose Enhancement to the Endothelial Cell Nucleus

W Ngwa^{1*}, M Makrigiorgos¹, R Berbeco¹, (1) Brigham and Women's Hospital, Dana Farber Cancer Institute and Harvard Medical School, Boston, MA

Purpose: Microdosimetry is employed to estimate dose enhancement to endothelial cell nuclei, caused by radiation-induced photo/Auger electrons originating from gold nanoparticles (AuNP) targeting the tumor endothelium, during brachytherapy. Methods: A tumor vascular endothelial cell (EC) is modeled as a slab of 2µm (thickness) × 10µm (length) × 10µm (width). The EC nucleus is centrally located with 5µm diameter and

reduction of 31% was attained using this modulation scheme. Visual inspection of a modulated CBCT slices shows appreciable image quality relative to the conventional CBCT. The noise characteristics of the modulated scan were about 20 HU worse than a conventional scan, likely due to the presence of scatter in the enlarged CATPHAN phantom because theoretical predictions are based on primary beam attenuation alone. Conclusions: Initial results demonstrate that the use of a modulated scanning technique, developed by taking into account patient anatomic variation, may be a feasible method to reduce dose while preserving image quality in CBCT-based IGRT.

SU-E-J-20

Dose Calculation for Pelvic Megavoltage Cone Beam CT Image with a Quadratic-Fit Based Correction

W Hu¹*, Z Zhang¹, J Pouliot², (1) Fudan University Cancer Hospital, Shanghai, Shanghai, CN, (2) UC San Francisco, San Francisco, CA

Purpose: The accurate dose recalculation requires that the original pelvic megavoltage cone beam CT (MVCBCT) images be corrected for cupping and truncation artifacts caused by beam scattering and field-of-view limitation. Our group previously developed a pelvic phantom-based correction algorithm. The purpose of this study is to introduce a simple yet accurate pelvic MVCBCT image correction strategy based only the planning kVCT and treatment-day MVCBCT images to allow accurate dose calculation. Methods: The quadratic-fit (QF) based correction algorithm uses the planning kVCT as a reference, and individually corrects the MVCBCT images slice by slice. A realistic pelvic-size water phantom, an anthropomorphic pelvic phantom, and a clinical pelvic patient were used to validate the method. Furthermore, a prostate patient with large anatomy changes in planning CT and a treatment-day MVCBCT was selected for evaluating the clinical applicability of the method. The dose differences with and without QF correction were compared. Results: The QF correction reduced the cupping artifact significantly. The maximum mean CT number deviations in the soft tissue part of the anthropomorphic phantom between the conventional CT and MVCBCT without and with QF correction were 15% and 2%, respectively. After applying the QF and data missing correction, 96.5% of the voxels showed a dose agreement better than 3% between the planning CT and MVCBCT. In a clinical patient without significant anatomy changes, the dose difference in the targets and organ at risks between the planning CT and a treatment-day MVCBCT was within 1.1%. Conclusions: The QF based method is feasible for correcting the cupping artifact in the pelvic MVCBCT. And, based on the corrected MVCBCT images, the monitoring of treatment-day dose distributions is possible.

Research supported in part by Siemens

SU-E-J-21

Verification of a Monte Carlo Model of CBCT Flat Panel Detector Using BEAMnrc/EGSnrc Code

S Kim¹*, L Ren¹, J Jin¹, J Kim¹, B Movsas¹, I Chetty¹, (1) Henry Ford Health System, Detroit, MI

Purpose: Cone beam computed tomography (CBCT) provides wide scan coverage per rotation; however, its image quality is compromised due to large amounts of scatter. In this study, we performed detailed Monte Carlo (MC) simulations of a CBCT flat panel detector to characterize scatter for the purposes of scatter correction. Methods: An amorphous silicon (aSi) flat panel detector (Varian Medical Systems) of an On-Board Imager (Varian Medical Systems) was modeled using BEAMnrc/EGSnrc code system based on detailed geometric information provided by the manufacturer. Layers from the proximal Al cover to the light reflector encompassing the 10:1 anti-scatter grid were simulated using the block component module (BLOCK_CM) in BEAMnrc. Layers from the cesium iodide (CsI) detector to the proximal Pb electronics protection cover were modeled in DOSXYZnrc to create a voxelized representation of the detector layer. Various scatter properties were elicited from phase space files within the grid and detector layers. A two-dimensional (2-D) cone-beam image "in-air" (without the phantom) was acquired (125 kVp, 80 mAs). 2-D and 1-D pixel intensities were compared to the simulated projection to verify the accuracy of MC simulation of the entire detector system. Results: 2-D pixel intensities of the computed image agreed well to the measured image as the difference map showed values within $\pm 10\%$. However, given the large number of histories required for detector simulation, the MC uncertainty was quite

high, up to 10% in some regions. The central axis profile also showed good agreement between simulation and measurement within 3% on average, except in the regions where the statistical uncertainty was larger ($1\sigma = 7.5\%$). Conclusions: A CBCT imager has been modeled in detail using the BEAMnrc/EGSnrc code system. Additional verification of the MC-based modeling is warranted for the purposes of scatter characterization.

SU-E-J-22

Measurement-Based Cross-Scatter Correction in Dual Detector Cone-Beam CT

W Giles^{*}, J Bowsher, H Li, F Yin, Duke University Medical Center, Durham, NC

Purpose: A dual detector cone-beam CT (CBCT) system could potentially allow for dual energy CBCT and dual-view DTS. However, image quality in this system is severely degraded by the presence of scatter between the two imaging chains, i.e. cross-scatter. The aim of this work is to develop a measurement-based method for correcting cross-scatter without increasing scan-time or exposure and without adding additional hardware. Methods: The dual detector CBCT imaging system has two tube/detector pairs mounted orthogonally; each 40x30 cm detector has an anti-scatter grid. The cross-scatter distribution was measured at a certain angular intervals by firing a single x-ray tube and reading out both detectors. Cross-scatter at intermediate angles was estimated by cubic spline interpolation. The cross-scatter estimates were subtracted from the projections prior to reconstruction. The angular interval between cross-scatter measurements was optimized for an anthropomorphic pelvic phantom. Accuracy of scatter interpolation was evaluated by comparing to directly measured cross-scatter. Effectiveness of scatter correction was evaluated by measures of contrast and contrast-to-noise ratio (CNR) in reconstructions of an image quality phantom from projection data acquired with and without cross-scatter. Results: For the pelvic phantom and an angular interval of 11 degrees, interpolated cross-scatter distributions were within 2.5% of measured cross-scatter distributions. This error remained constant as the angular interval decreased below 11 degrees and rose sharply to about 90% as the angular interval increased to 34 degrees. The contrast was 58.0%, 70.8% and 70.8%, in the uncorrected, corrected, and cross-scatter free reconstructions and similarly the CNR was 23.6, 22.8 and 24.9. Conclusions: This measurement-based method effectively corrects for cross-scatter without any additional hardware or imaging dose.

This work is partially supported by a research grant from Varian Medical Systems.

SU-E-J-23

Construction of Digital Phantoms for X-Ray Image-Guided Radiotherapy (IGRT)

L Zhou¹, J Chang²*, (1) NewYork-Presbyterian Hospital/Weill Cornell Medical College, New York, NY, (2) NewYork-Presbyterian Hospital/Weill Cornell Medical College, New York, NY

Purpose: To construct digital phantoms for testing x-ray-based IGRT software using anatomic CT images and NIST mass attenuation coefficients table of different tissue types for photon energies ranging from 1keV to 20MeV. Methods: CT images of the interested sites are first segmented into different tissue types based on the CT numbers, and converted to a three-dimensional (3D) attenuation phantom by linking each voxel to a lookup table of that voxel's tissue type containing the energies and corresponding mass attenuation coefficients from the NIST table. The x-ray source can be a radio isotope or an x-ray generator with known spectrum data consisting of the weight $w(n)$ for each energy bin $E(n)$. Siddon's method was used to compute the x-ray transmission line integral for detector m and energy $E(n)$ by ray tracing through the attenuation phantom from the x-ray source to detector m and summing up the interpolated attenuation coefficient for $E(n)$ along the ray. The x-ray fluence at detector m is then the weighted sum of the exponential of line integral for all energy bins with added Poisson noise. Results: We built a digital phantom using the CT scan of a Rando head phantom segmented into three (air, grey/white matter and bone) regions and simulated poly-energetic projection images for Mohan 4MV energy spectrum. The projection images are similar to typical portal images obtained with 4 or 6 MV x-ray source. The CBCT reconstructed from the simulated projection images showed similar but noisier and blurrier geometric features in comparison to the segmented CT scan, which is

expected for a 4 MV source. Conclusions: We have successfully built digital phantoms using anatomic CT images and NIST mass attenuation coefficients table. The constructed digital phantoms can be used to generate 2D projection images and 3D CBCT images for testing x-ray-based IGRT algorithms/systems.

SU-E-J-24

Measurement of Skin Dose Toward Real-Time Tumor Tracking Irradiation in MHI-TM2000 (VERO): A Preliminary Study

T Nakai^{1*}, A Sawada², S Kaneko³, HTanabe¹, M Sueoka¹, K Kubo¹, M Kokubo¹, (1) Institute of Biomedical Research and Innovation, Kobe, Hyogo, JP, (2) Kyoto University, Kyoto, Kyoto, JP, (3) Mitsubishi Heavy Industries, Ltd., Hiroshima, JP

Purpose: The purpose of this study was to estimate skin dose from real-time X-ray fluoroscopy imaging to do clinical trials for real-time tumor irradiation in MHI-TM2000 system (Vero). Methods: First, exposure dose with backscatter was measured using a single set of kilovoltage X-ray tube and a flat panel detector; a cylindrical ionization chamber (DC300, IBA); and a water-equivalent plate phantom. The chamber was rigidly attached on the plate phantom of 200 mm in thickness. Then, the chamber was positioned to 150 mm upper from the isocenter. Subsequently, exposure dose to an irradiation field of 171 mm x 226 mm was measured at a speed of 5 fps with 200 mA of the X-ray tube current; and 40~120 kVp of the X-ray tube voltage, respectively. The nominal exposure time was set to 5 ms. Next, half-value layer of aluminum was measured using a spherical ionization chamber (A4, Exradin) to calculate the effective energy and absorbed dose conversion factors of soft tissue. Then, the skin dose was calculated from the exposure dose and absorbed dose conversion factors. Results: There were good liner correlations between the X-ray tube current and skin doses; and therefore, estimated skin dose from the X-ray fluoroscopy with 1 mAs and 100 kV was 140 μ Gy. Furthermore, estimated skin dose for one successive minute exposure at a speed of 5 fps with 0.1 mAs and 100 kV was 4 mGy. The skin doses in the MHI-TM2000 were greater by a factor of 1.4~1.6 than those in Elekta Synergy system with the tube voltage of 100 or 120 kV. Conclusions: We have observed that the skin dose is a little larger than in the Synergy system while the filtration to the X-ray source has not been applied to the MHI-TM2000. To perform real-time tumor tracking, further investigation may be required.

This research was in part sponsored by Mitsubishi Heavy Industries, Ltd., Japan.

SU-E-J-25

Just-In-Time Tomography (JiTT): A New Imaging Technique for Monitoring Target Motion During Volumetric Modulated Arc Therapy (VMAT)

G Pang^{1*}, (1) Odette Cancer Centre, Department of Radiation Oncology, University of Toronto, Toronto, ON, CA

Purpose: Volumetric modulated arc therapy (VMAT) is a new efficient way of delivering intensity-modulated radiation therapy (IMRT) on a conventional linear accelerator (Linac) in which the gantry rotates while the beam is on. Intrafraction target motion is still a concern for high precision VMAT treatments. In this work, we propose to apply a new concept --- just-in-time tomography (JiTT) to monitor target motion during a VMAT delivery. Methods: Similar to the cone beam computed tomography (CBCT) approach, JiTT (Pang and Rowlands, Phys. Med. Biol. 50, N323 (2005)) uses a gantry mounted X-ray source (e.g., a kV source on a Linac) and an X-ray area detector to acquire projection data by simultaneously rotating them around the target. Differing from CBCT, JiTT can be performed during the treatment (i.e., imaging and treatment at the same time), and it takes less time to generate the needed tomographical, beam's-eye-view images of the treatment target in real time. A computer simulation using MATLAB has been conducted to investigate the feasibility of this new approach. Results: JiTT images of the Shepp-Logan phantom with motion have been obtained. It has been shown that target motion can result in significant motion artifacts in JiTT images. These motion artifacts in the images could then be used to determine target motion and guide the VMAT treatment. Conclusions: We have proposed to apply a new concept --- just-in-time tomography (JiTT) to image-guided VMAT delivery on a conventional Linac equipped with a kilovoltage cone beam computed tomography (kV-CBCT) system. A computer simulation has been conducted and it has been demonstrated that JiTT images are sensitive to target motion.

SU-E-J-26

Real-Time Dynamic Management of the Correlation Between Internal Tumor Movement and External Abdominal Motion

H Wu^{1*}, D Jain¹, Q Zhao², (1) IUPUI, Indianapolis, IN, (2) IU Health Proton Therapy Center, Bloomington, IN

Purpose: To reduce radiation exposure, internal/external correlation has been applied to derive tumor position based on radiation free external motion tracking. However, the reliability and stability of the correlation is a big concern. This study will characterize the temporal correlation patterns and provide a dynamic approach to build reliable correlation with minimum internal imaging. Methods: Retrospective analysis has been performed on simultaneously collected 3D internal and 1D external motion of eight patients with 51 treatment days and 165 beams. Both static and dynamic correlations are built through linear and quadratic functions. Static approach compares and summarized the correlation patterns of different granularities (different patients, treatment fractions, beams, and breathing cycles). Dynamic approach studies the temporal correlation patterns and derives tumor positions by adjusting three parameters: internal imaging frequency, previous acquired tumor positions, and future tumor positions. The correlation coefficient and the difference between derived and truly observed tumor positions are used to evaluate the accuracy. Results: The statistical analysis showed that the internal/external correlation is patient specific. Overall, the quadratic correlation outperforms the linear correlation. For the 8 patients, three patients have steady internal/external correlation (1 SD <0.35%), three with medium variation (<0.65%), and two with significant changes (<2.50%). The temporal changes of the last two patients showed that considerable correlation variations exist from day to day, beam to beam, and breathing cycle to cycle during the same beam delivery. Different combinations of the three parameters for the dynamic approach showed the most recent breathing patterns are of more importance in building a reliable correlation and internal imaging frequency of 1 Hz is sufficient for most patients. Conclusions: This study addressed several major concerns for establishing reliable internal/ external correlations. Dynamic correlation with proper settings will yield improved tumor tracking precision with minimal internal imaging.

In part supported by NIH/NCI 1R21CA130849

SU-E-J-27

4DCT-Derived Treatment Planning Scan with Improved Quality

D Michalski^{1*}, G Bednarz², M Huq³, D Heron⁴, (1) UPMC, Pittsburgh, PA, (2) University of Pittsburgh Medical Center, Pittsburgh, PA, (3) University of Pittsburgh Medical Center, Pittsburgh, PA, (4) UPMC cancer institute, Pittsburgh, PA

Purpose: To improve the quality of the treatment planning CT volume for cancer occurring in upper abdomen. Method and Materials: Delineation of tumors in liver or pancreas critically depends on the image quality due to rather weak radio-opacity difference between the tumor and surrounding tissue. Since for cases with tumor motion > 0.5cm, phase 50% scan is used for treatment planning the quality of this image is worse than its helical equivalent. Thus in order to improve Signal to Noise ratio (SNR) and Contrast to Noise ratio (CNR) of the phase 50 scan a synchronized averaging of the entire 4DCT data set is applied to create a composite CT volume equivalent to phase 50 scan. Four dimensional CT scans of ten patients with liver and pancreas cancer were used retrospectively in this study. In-house implementation of Demons algorithm allowed for adding the deformed CT phases to phase 50% scan. Results: Improved SNR for all cases was observed. Average improvement of SNR for all cases in the region of interest was by a factor of 2.8. The scan also look better for a visual inspection. Conclusion: Synchronized averaging of the 4 DCT scan can be used to obtain better quality treatment planning scans. However possible artefacts in 4DCT phases might preclude effective use of the entire set of CT phases.

surface irregularity and scattering characteristics differ from each other. As for the lower dose regions, the pass ratio was up to 30.1%, indicating that large differences were observed between the AAA and the AcurosXB. The presence of low density regions, such as lung and bowel gas, and the accuracy of beam modeling in penumbra regions were attributed to the differences. Particularly in breast cases, lower doses were spread over the contralateral breast surface with the AAA, but not with the AcurosXB.

Conclusions: This study demonstrated that the AcurosXB algorithm had a good agreement with the AAA in homogeneous region; however, large differences were observed in the penumbra regions and heterogeneous regions. When the AcurosXB is applied in the clinical practice, the detail examinations are required for various sites.

Author Disclosure: S. Sato: None. M. Nakamura: None. M. Nakata: None. Y. Tsuruta: None. Y. Miyabe: C. Other Research Support; Research contract with Varian Medical Systems. T. Mizowaki: None. A. Sawada: None. M. Hiraoka: C. Other Research Support; Sponsored research program of Varian Medical Systems.

3459 Non-Vertical Co-Planar Beam Arrangement Can Improve Dose to Organs at Risk (OARs)

L. Nedialkova, M. Delamerced, A. Sabbas, J. Chang, C. Chao

New York-Presbyterian Hospital/Weill Cornell Medical Center, New York, NY

Purpose/Objective(s): Although non-coplanar beams can achieve better sparing of the OARs, they usually require complex and undesirable combination of gantry and couch rotations. In this study, we investigate an alternative approach-the non-vertical coplanar beam arrangement in which the patient or the linear accelerator (LINAC) is tilted to best match the patient anatomy and avoid the OARs.

Materials/Methods: We used the built-in body board function of our treatment planning system to simulate the tilt of the patient or the LINAC for skull base/brain, head and neck, and prostate planning. This function allows the tilting of patient body up to 60 degrees from the gantry side and 10 degrees from the couch side. Thirty treatment (10 for each site, most IMRT but some 3D conformal) plans were randomly selected and retrieved from the archive for this study. For each plan, we first found the optimal tilt angle by re-optimization using different body angles while keeping the original planning parameters including collimator angle, gantry angle, jaw sizes, dose-volume histogram constraints. The plan with the optimal tilt angle was then further optimized by adjusting the planning parameters. The considered OARs were brainstem, optic nerves, optic chiasm, and optic lenses for the skull base/brain; oral cavity, brain stem, parotid, mandible, cord, larynx, cochlea and esophagus for head and neck; and rectum, bladder and right/left femur for prostate. Dose volume histograms (DVHs) of these OARs were compared between the original and new plans.

Results: By changing the body angle of the treatment position, we were able to decrease the doses to the OARs and keep the PTV coverage for skull base/brain and prostate plans. No significant improvements were observed for head and neck cases. The most substantial improvement was achieved for skull base/brain cases, in which the dose reductions were significant for lenses (right $57.3 \pm 27.9\%$, left $48.7 \pm 40.7\%$), optic nerves (right $16.2 \pm 49.0\%$, left $19.6 \pm 52.3\%$), and optic chiasm ($17.7 \pm 33.3\%$) but not for brain stem ($0.1 \pm 19.4\%$). For prostate cases, significant dose reduction was achieved for femurs (right $11.0 \pm 10.5\%$, left $11.9 \pm 9.3\%$) while dose only decreased slightly for bladder ($1.0 \pm 0.7\%$) and rectum ($1.4 \pm 1.8\%$). We expect better sparing of bladder and rectum for prostate cases if the patient could have been tilted at a larger angle from the couch side.

Conclusions: The non-vertical co-planar beam arrangement provides an additional flexibility for treatment planning to achieve similar OAR sparing as the non-coplanar beam arrangement. Since this new beam arrangement accomplished dose reduction by tilting the patient or LINAC instead of rotating the couch, it also allows dose delivery using volumetric modulated arc therapy.

Author Disclosure: L. Nedialkova: None. M. Delamerced: None. A. Sabbas: None. J. Chang: None. C. Chao: None.

3460 Evaluation And Analyze Of Out-of-field Doses In Head And Neck Radiation Therapy For Different Delivery Techniques: From 3DCRT To VMAT

C. Lafond^{1,2}, M. Olivier¹, E. Chajon¹, J. Manens^{1,2}

¹Eugene Marquis Center, Regional Cancer Center, Rennes 35042, France, ²INSERM U642, University of Rennes, Rennes, France

Purpose/Objective(s): In radiotherapy, the dose delivered by a linear electrons accelerator out of the treatment field depends on the implemented delivery technique. The purpose of this study is to evaluate and set for head and neck (H&N) treatments the out-of-field dose level in Volumetric Modulated Arc Therapy (VMAT), when compared with conformal radiotherapy (3DCRT), step-and-shoot (S&S) and sliding window (SW) IMRT.

Materials/Methods: This study used the treatment planning system Pinnacle V9.0, two linear accelerators: an Elekta Synergy and a Varian Clinac 2100C. We used GR200A thermoluminescent dosimeters that were placed in the ATOM-CIRS phantom: i) to plot dose profiles until 57 cm from the field edge with a 5 cm step, j) to measure the dose at radiosensitive organs, k) to establish the spatial dose distribution around two transverse sections. Measured doses were rescaled to the total treatment. We analyzed and compared these doses basing on out-of-field dose components.

Results: When the distance from the field edge increased from 5 to 57 cm, the measured doses decreased from 149 to 4 cGy in SW, from 113 to 2 cGy in VMAT, from 100 to 3 cGy in S&S, and from 85 to 4 cGy in 3DCRT. In SW, in VMAT, in S&S, and in 3DCRT, the measured doses were respectively of 211, 120, 111 and 102 cGy for the left crystalline lens, respectively of 70, 29, 27, and 27 cGy for the left breast, and respectively of 4, 2, 3 and 4 cGy for the gonads. Around each transverse sections located at 4,5 and 9,5 cm from the field edge, the mean measured dose was respectively of 78 and 37 cGy in VMAT, and of 75 and 32 cGy in S&S- IMRT.

Conclusions: For H&N treatments, VMAT out-of-field doses were in the same order of magnitude compared to S&S doses, but out-of-field doses were spatially differently distributed. VMAT doses were on average 60% smaller than in SW for distances ranging from 5 to 57 cm from the field edge.

Author Disclosure: C. Lafond: None. M. Olivier: None. E. Chajon: None. J. Manens: None.

Materials/Methods: Patients with large pendulous breasts were selected to be treated in the prone position to benefit the dosimetric advantages. Each patient was positioned prone on the immobilization board allowing the ipsilateral breast to fall in the open slot. The contralateral breast was pulled out in the opposite direction to clear a beam path. The treatment isocenter was placed about 7cm below the surface of the immobilization board, centered in the left-right and crania-caudal directions. A separate imaging isocenter was placed 15cm posterior to the treatment isocenter, which is 8cm above the surface of the immobilization board, in the same left-right and crania-caudal planes. Images taken at this isocenter allowed improved imaging of the ribs and sternum compared to imaging at the treatment isocenter. Medial- and lateral-tangential beams were designed to cover the entire breast with 2-3cm skin flash. Daily setup was done by aligning lasers in the treatment room to the imaging isocenter based on the skin markers. Next, two orthogonal images in posterior-anterior (PA) and left-lateral (LLat) views were acquired using on-board MV and kV imaging systems to verify the patient position. Patient positioning correction was performed by manually rotating the patient and automatically applying the translational shift of the table. After repositioning, the table was shifted 15cm from the imaging isocenter to the treatment isocenter. The medial-tangential treatment beam was then imaged with the MV imaging system to verify skin-flash, treatment isocenter, and field shape and weekly lateral-tangential beam was also imaged.

Results: Average shifts for repositioning in vertical, longitudinal, and lateral directions were 0.9cm, 0.6cm, and 0.8cm at the initial imaging isocenter and were 0.3cm, 0.2cm, and 0.0cm at the treatment isocenter. No repositioning was performed after imaging of lateral tangential ports. The average time spent for daily imaging was 9.2 minutes. The daily average numbers of images were 1.2 for kV and 3.9 for MV.

Conclusions: A dual-isocenter image guidance technique was developed for prone-breast treatment. This allows us to perform IGRT without collision for large patients. Further improvements are expected to reduce the patient setup time and the number of images.

Author Disclosure: S. Yoo: None. J. O'Daniel: None. J. Horton: None. R. Blitzblau: None. F. Yin: None.

3288 Feasibility Study of Panoramic Cone Beam Computed Tomography (CBCT)

L. Zhou¹, Y. Chi², K. S. C. Chao¹, J. Chang¹

¹NewYork Presbyterian Hospital/Weill Cornell Medical College, New York, NY, ²Columbia University, New York, NY

Purpose/Objective(s): We have previously proposed a novel "panoramic CBCT" technique which can image patients at the treatment position with a volume as large as practically needed, and demonstrated its concept and reconstruction artifacts with simulated data. In this study, we investigate its clinical feasibility using phantom data.

Materials/Methods: In panoramic CBCT we scan the target panoramically for half scan ($180^\circ + \text{cone angle}/2$ gantry rotation), stitch together the panoramic projection images of the same gantry angle, and use the stitched projection images for CBCT reconstruction. To study the feasibility of this imaging technique, we acquired projection data for a CT calibration phantom using the on-board kV CBCT system of a linear accelerator (LINAC). The center of the phantom was positioned 12 cm to the right of the LINAC central axis. Two CBCT scans were performed: one with kV detector in the center position and the other with kV detector shift by 14.8 cm to the right. The projection images of the same gantry angles were stitched together according to the reported detector positions to form large projections. Each stitched projection image consisted of images from the central position, the right and the left lateral positions (14.8 cm to each side). We averaged the image intensity for pixels in the overlapping region, adopted the original image intensity of pixels in the non-overlapping regions and padding open-air intensity for the left position since no real projection images were acquired (no object on the left side). Both conventional FDK (Feldkamp filtered backprojection) and SART (Simultaneous Algebraic Reconstruction Technique) methods were used to reconstruct CBCT images for half scan. The reconstructed volume was a matrix of $512 \times 512 \times 256$ voxels with a voxel size of 1mm. No additional correction and image processing were used before reconstruction.

Results: The projection images of individual imager location were incomplete for half scan CBCT reconstruction as the images of the target were truncated at certain gantry angles. Complete reconstructions were obtained for both FDK and SART methods from the stitched projection images for half scan. SART reconstruction had better contrast-to-noise ratio than FDK reconstruction at the expense of computation time (a day vs. a half hour). Image artifacts were observed due to misalignment of the projection images and exposure fluctuation during image acquisition.

Conclusions: Implementation of the proposed panoramic CBCT in a clinical environment is feasible for half scan ($\sim 200^\circ$ gantry rotation), which can be performed for most cases in treatment position without collisions. Good image stitching algorithms are needed to minimize the reconstruction artifacts due to imperfect stitching. Fast parallel processing is also required to speed up SART reconstruction for clinical use.

Author Disclosure: L. Zhou: None. Y. Chi: None. K.S.C. Chao: None. J. Chang: None.

3289 Peripheral Patient Dose Measurements for IMRT Delivered with Helical Tomotherapy and Linac

D. D. Deshpande¹, R. A. Kinshikar¹, R. Upreti¹, S. Chaudhari¹, C. Tambe¹, S. Kadam¹, D. Dhote²

¹Tata Memorial Hospital, Mumbai, India, ²Department of Electronics, Brijlal Biyani Science College, Amravati, India

Purpose/Objective(s): To estimate peripheral doses (PD) to the healthy tissues outside the treated region for intensity-modulated radiotherapy (IMRT) delivered with helical Tomotherapy (HT) and linac with dynamic multileaf collimator (dMLC). The PD is a result of the increased x-ray leakage radiation to the patient due to the longer beam-on times associated with IMRT. The increasing use of IMRT has focused attention on the need to account for PD because of increasing probability of secondary malignancies. It was attempted in this study to measure the PD for IMRT patients.

Materials/Methods: On Trilogy linac (Varian) and HT, both with 6 MV photons, 20 patients each were randomly selected for this study. Radiotherapy plans were generated with the Eclipse (Varian) and with the Tomoplan planning system. Measurements of PD were done with the help of thermoluminescent dosimeters (TLD: LiF:MgTi) and Semi Conductor Diodes (DPD-12) along the longitudinal axis of the patient outside the primary beam at different distances (5 cm interval up to 25 cm) from the edge of the planning target volume (PTV). Diodes and TLDs (for low dose sensitivity) were calibrated in Linac and HT prior to the measurements. TLDs were irradiated for ten consecutive fractions considering the sensitivity of the detector. Diodes were kept at 10

excellent outcomes. However, the commonly used dose-volume metrics for normal liver do not correlate well with NTCP. A new metric is proposed in this study.

SU-C-BRB-05

Accounting for Anisotropic Growth of Glioma in Radiotherapy Planning

J Unkelbach^{1*}, B Menze², E Konukoglu³, A Motamedi⁴, N Ayache⁵, H Shih⁶, (1) Massachusetts General Hospital, Boston, MA, (2) ETH Zurich, Switzerland, (3) Microsoft Research, Cambridge, UK, (4) Massachusetts General Hospital, Boston, MA, (5) INRIA Sophia Antipolis, France (6) Massachusetts General Hospital, Boston, MA

Purpose: We study a phenomenological tumor growth model for improved target volume definition for radiotherapy of glioblastoma. Currently, an isotropic margin is added to the visible tumor to account for microscopic tumor cell infiltration in normal appearing brain tissue. However, it is known that glioma growth is not isotropic. The ventricular system and the dura, including falx cerebri and tentorium cerebelli, represent anatomical barriers for migrating cells. Such anatomical constraints are currently not consistently and quantitatively incorporated in target delineation. **Methods:** We assume that tumor growth is characterized by local proliferation of tumor cells and diffusion into neighboring tissue. Mathematically, this can be described via a partial differential equation of reaction-diffusion type, the Fisher-Kolmogorov-Equation. Anatomical constraints are modeled via no-flux boundary. Solving the model equations provides a three-dimensional distribution of the tumor cell density. The radiotherapy target can be defined as an iso-line of the cell density. **Results:** Two specific questions were investigated: First, tumor locations in which the model may be particularly useful have been identified; and second, a sensitivity analysis with respect to the model inputs was performed. Tumors located in proximity to the falx cerebri may benefit: The model is able to describe both the falx as a boundary and the corpus callosum, which provides a route for tumor cells to spread to the contralateral hemisphere. This effect is often not consistently accounted for in manual target delineation. Among all model parameters, correct segmentation of the brain is a critical prerequisite. **Conclusions:** The tumor growth model represents a tool to objectively create target volumes for radiotherapy of glioblastoma by consistently accounting for known growth patterns. All model inputs can be linked to model outputs, making it possible to assess the impact of uncertainties - an essential step for an application in clinical practice.

SU-C-BRB-06

Modeling Stereotactic Body Radiation Therapy (SBRT) Including Cell Cycle-Dependent Radiosensitivity, Hypoxia, Reoxygenation and Proliferation: Is SBRT Explainable Based On Classical Radiobiological Factors?

J Jeong^{1*}, J O Deasy², (1) University of Missouri, Columbia, MO, (2) Memorial Sloan Kettering Cancer Center, New York, NY

Purpose: The tumoricidal effectiveness of standard fractionation radiotherapy is usually understood qualitatively in terms of proliferation, hypoxia, and reoxygenation. We have developed a novel, state-based computational model that includes those factors. The efficacy of SBRT has been hypothesized to be due to other factors, such as apoptosis of vasculature and/or immune-response factors. The goal of this project is to see if SBRT can potentially be explained using only those classical radiobiology factors. **Methods:** The state-based computational model considers the cell cycle effect on radiosensitivity and cycle reassortment. Varying fractionation schemes were compared in terms of model predicted equivalent dose at 2 Gy/fx (EQD_{model}). Using relevant parameters for lung cancer tumors, the EQD_{model} was estimated for several typical SBRT regimens. **Results:** SBRT is predicted to benefit from less repopulation (as expected) and high cell-kill relative effectiveness, but is also predicted to suffer from less reoxygenation and the absence of cell-cycle reassortment. Overall, the model predicted EQD_{model} was significantly reduced from the BED-based NTD2 (NTD2=BED/1.2, assuming alpha/beta=10), typically by about 25-30%. The treatment duration of SBRT affected the treatment efficacy and the ratio of EQD_{model}/NTD2 was lowest for high dose single fraction SBRT (~60%). With longer treatment duration, the EQD_{model} increased and approached to NTD2, due to increased reoxygenation. For most evaluated SBRT regimens, predicted cell-survival levels were too high to account for the reported high local-response rates of the SBRT outcomes. **Conclusions:**

Considering four Rs of radiobiology, the equivalent dose in 2 Gy/fx was estimated for several SBRT regimens. The treatment efficacy of SBRT estimated from BED is significantly overestimated compared to the model results and the SBRT schedule seems to affect the treatment efficacy. Non-classical biological or radiobiological principals are apparently at work in high-dose SBRT treatments. Supported by the Enid A. Haupt Endowment for Medical Physics

Joint Imaging-Therapy Short Oral Ballroom A Motion Assessment and Management: CT, CBCT, & Fluoroscopy

SU-C-BRA-01

4D Cone-Beam CT Acquisition Using Respiratory Phase Predication Technique

P Yan^{1*}, L Zhou², Z Li², Y Chi¹, J Chang², C Chao^{1, 2}, (1) Columbia University Medical Center, New York, NY, (2) Cornell University, New York, NY

Purpose: Respiration-correlated CBCT reduces respiratory motion artifacts at the cost of increased view-aliasing artifacts due to the gaps in projection data that are sorted to other phases. Respiratory-gated acquisitions can cover the full scanning range but is inefficient (~5 minutes per phase). In this study, we developed a 4D CBCT acquisition method using respiratory phase predication technique that can potentially acquire full projection data for each phase within a clinically acceptable (~10 minutes or less) time. **Methods:** The proposed 4D CBCT continuously scans the target until sufficient number of projections is acquired for all phases. The respiratory phase predication technique consists of the following iterative steps: (1) training using respiratory signal for the first few (e.g., five) breathing cycles; (2) initial optimization of the gantry rotation speed; (3) adaptive control of the rotation speed and image acquisition during the scan (4) sorting the projection images into different phases. The method was validated using the 4D XCAT digital lung phantom with the motion driven by a sinusoid wave and a real patient respiration signal acquired with RPM system. CBCT images were reconstructed for each phase using the simultaneous arithmetic reconstruction technique and compared with the mixed-phase reconstruction. **Results:** Sufficient projection images (an angular interval less than 1 degree) were acquired for all 10 phases after 10 gantry rotations. The acquisition time was estimated from 10-12 minutes assuming each gantry rotation took ~1 minute. The CBCT images reconstructed from the mixed-phase projections were blurred in comparison to those for individual phases. **Conclusion:** A respiratory prediction technique for 4D CBCT has been developed and validated with real patient breathing pattern. We plan to further reduce the number of gantry rotations and therefore the scanning time by improving the control of adaptive image acquisition and taking advantage of data redundancy as in 4D CT.

SU-C-BRA-02

Evaluation of 2D DIR From CBCT to 4DCT Projections as a Tool for IGART

V Kearney^{1*}, X Wang¹, X Gu², H Yan¹, X Zhen¹, X Jia¹, S Jiang¹, L Cervino¹, (1) University of California San Diego, La Jolla, CA, (2) UT Southwestern Medical Center, Dallas, TX

Purpose: To demonstrate 2D parallelized DIR as a method to correct for anatomical changes of patient anatomy and respiratory motion. CBCT to simulated 4D-CT projections using DIR can be used in real time for respiratory phase determination, patient setup or as a retrospective analysis to track inter- and intra-fractional deformations. **Methods:** Ten phases of simulated 4DCT respiratory projections were individually registered to pulmonary CBCT projections using a modified 2D-DIR demons algorithm implemented on GPUs. An automated global image-preprocessing algorithm of the simulated projection was implemented to account for the relative local inter-modality intensity mismatch. The deformation vector field intermodality congruence was inspected using bony structures, diaphragm position, and tumor position. A phase prediction matrix was constructed by choosing the lowest sum absolute value of the ten deformation vector fields generated by DIR. **Results:** For AP projections SI and tangential respective deformation maximum displacements were 4.8mm and 4.78mm with a mean displacement of 1.71mm +/- 1.17mm and 1.07mm +/- 0.94mm. For Lateral projections SI and tangential respective deformation maximum

Projection images demonstrate that the iris produces effective collimation with minimal leakage. Reconstructed CBCT images are affected by truncation artefact, but this may be remedied by data filling techniques or other (e.g. pi-line) reconstruction algorithms. **Conclusions:** The technology presented is a novel approach to kV CBCT, localizing imaging dose to a chosen VOI while, compared to full-field CBCT, reducing dose both inside and outside of the VOI. No conflict of interest exists.

TH-C-BRA-03

Fast Iterative Cone Beam CT Reconstruction On GPGPU Using OpenCL

L Zhou*, J Chang, Cornell Medical College, New York, NY

Purpose: Algebraic reconstruction technique (ART) type algorithms produce superior image quality for CBCT and CT reconstructions over the popular filtered-back-projection based approaches but are too slow for real-time clinical applications. The purpose of this study is to employ the emerging OpenCL architecture to accelerate simultaneous ART (SART) by parallelizing the most time-consuming forward- and back-projections using General-Purpose-Graphics-Processing-Unit (GPGPU). **Methods:** For each iteration, SART sequentially performs three ray-driven projections (one forward- and two back-projections) for each acquired projection image. To accelerate SART reconstruction, both forward projection and back-projection kernels were scheduled on GPGPU using data parallelism to take full advantage of compute units on GPGPU. The single-work-item-for-single-ray technique was employed as parallelization mechanism. We conducted numerical experiments to test OpenCL-based implementation on a Dell Precision T7500 workstation with two quad-core CPUs and one Nvidia Tesla C2050 GPGPU. Poly-energetic projection data (512x512) for the Mohan 4 MV energy spectrum were simulated each degree for 360 gantry angles for a head-and-neck digital phantom and were fed into the SART algorithms for CBCT reconstruction of 256x256x256 volume. To accelerate poly-energetic projection computation, we partitioned the workloads using task parallelism and data parallelism and scheduled them in a parallel computing ecosystem consisting of CPU and GPGPU using OpenCL only. **Results:** The GPGPU computation time including the kernel launch time, kernel running time and data transfer time was 42 ms for forward-projection and 95 ms for back-projection. Each SART iteration took 101 s on GPGPU in comparison to 7195 s on a single-threaded CPU. The proposed method achieved a ~71-times speedup. The relative difference of the reconstructed images between the CPU-based and OpenCL/GPGPU-based implementations was on the order of 0.00001 and virtually indistinguishable. **Conclusions:** We have successfully implemented the SART algorithm on GPGPU using OpenCL and significantly reduced the reconstruction time to a level that is almost suitable for real-time clinical applications.

TH-C-BRA-04

Endorectal Balloons in Post-Prostatectomy: Do Gains in Stability Lead to More Predictable Dosimetry?

M Jameson^{1,2*}, J De Leon¹, A Windsor^{1,3}, K Cloak¹, L Holloway^{1,2,4}, P Vial^{1,4}, M Sidhom^{1,3}, P Metcalfe², (1) Liverpool and Macarthur Cancer Therapy Centres, Liverpool, NSW, Australia (2) University of Wollongong, Wollongong, NSW, Australia (3) Collaboration for Cancer Outcomes Research and Evaluation, Liverpool, NSW, Australia (4) School of Physics, University of Sydney, Sydney, NSW, Australia

Purpose: To perform a comparative study assessing potential benefits of endorectal balloons (ERB) in post-prostatectomy patients **Methods:** Ten retrospective post-prostatectomy patients without ERB and ten prospective patients with the ERB in situ were treated with IMRT using kilo voltage cone beam computed tomography (kVCBCT) image guidance (IGRT). A kVCBCT dataset from each treatment week was registered to the planning dataset, recontoured and the original plan recalculated on the kVCBCTs to recreate actual anatomical conditions during treatment. The imaging, structure and dose data were imported into Matlab. In house applications analysed geometric variation in the two groups and calculated cumulative equivalent uniform dose (EUD). **Results:** Analysis of the kVCBCT datasets showed that the ERB improved target volume stabilization from millimetre to sub-millimetre reproducibility. The variation in bladder location in the non ERB cohort was 1.5 ± 0.9 cm compared to 0.6 ± 0.4 in the ERB group. While the superior rectum location variation was 1.1 ± 0.8 cm and 0.3 ± 0.3 cm for non ERB and ERB respectively. The mean difference in cumulative EUD and planned EUD for the clinical target volume (CTV) was 0.6 ± 0.04

Gy for non ERB and 0.4 ± 0.1 Gy for ERB. The largest normal tissue differences were seen for the bladder with an increase of 4.4 ± 0.1 Gy for non ERB and 1.2 ± 0.02 Gy for ERB in the cumulative compared with the planned EUD. Differences in delivered superior rectal EUD was improved in the ERB cohort with a difference of -0.2 ± 0.04 Gy verse 3.0 ± 0.3 Gy in the non ERB group. **Conclusions:** The ERB cohort was found to have more stable and reproducible anatomy when compared to the non ERB cohort. Planned and cumulative EUD differences were greatest for the bladder and rectum.

TH-C-BRA-05

High Quality Four Dimensional Cone-Beam CT by Deforming Prior Planning CT

J Wang*, X Gu, T Solberg, UT Southwestern Medical Center, Dallas, TX

Purpose: To enhance the image quality of four dimensional cone beam computed tomography (4D-CBCT) of lung cancer patients through using information from the initial planning CT. **Method and Materials:** 4D-CBCT is obtained by deforming the planning CT. The estimation of the deformation vector fields (DVF) to deform the planning CT is formulated as a unconstrained optimization problem. The objective function to be minimized is the sum of the squared difference between the forward projection of the deformed planning CT and the measured 4D-CBCT projection. A non-linear conjugate gradient (NLGC) method is used to solve the DVF. As the number of the variables in the DVF is much greater than the number of measurements, the solution to such a highly ill-posed problem is very sensitive to the initial parameters during the optimization process. We propose to estimate the DVF using demons registration between planning CT and 4D-CBCT reconstructed by total variation minimization as the initial parameters in the optimization process. A 4D nonuniform rotational B-spline based cardiac-torso (NCAT) phantom and a patient 4D-CBCT are used to evaluate the algorithm. **Results:** Image quality of 4D-CBCT is substantially improved by using the proposed strategy in both NCAT phantom and patient studies. For the NCAT phantom, the relative error within lung in 4D-CBCT reconstructed using the standard FDK from 20 projection views is 43.3%; the relative error is 21.5% in images reconstructed by total variation minimization, and further reduced to 12.5% in images reconstructed using the proposed strategy. **Conclusion:** Using the proposed strategy, high quality 4D-CBCT can be obtained by deforming an initial planning CT. Results from the phantom evaluation study demonstrates that 20 projections are sufficient to reconstruct 4D-CBCT of high accuracy. This work was supported in part by Cancer Prevention and Research Institute of Texas (CPRIT RP110562-p2).

TH-C-BRA-06

Measurement Based Source Model for On-Board Imager Monte Carlo Dosimetry Simulations

K McMillan*, A Michailian, M McNitt-Gray, D Ruan, University of California, Los Angeles, Los Angeles, CA

Purpose: The purpose of this study is to investigate and develop a systematic approach to quantify the dose impact of the radiographic and cone-beam computed tomography (CBCT) modes of operation of the on-board imager (OBI) on radiotherapy treatment machines, independent of manufacturer's data specifications. **Methods:** In order to facilitate dose calculations using Monte Carlo (MC) methods, we have developed an equivalent source model for OBI systems consisting of an equivalent spectrum module incorporative of intrinsic filtration and an equivalent filter module characterizing the added bowtie filter. The equivalent spectrum was generated by iteratively updating the source spectrum estimate until the calculated beam behavior matched the measured half-value layer and quarter-value layer values. The equivalent filter was established by obtaining a series of exposure readings along the bowtie profile and calculating the equivalent path lengths of a particular filter material. The equivalent spectrum module was validated by assessing the consistency of the estimation results obtained from half- and full- bowtie measurements. The end-to-end system was validated by comparing dose distributions from MC simulations based on an equivalent spectrum and an equivalent filter with dose distributions from film measurements for both the full- and half-bowtie scenario. **Results:** Results were generated using a 95 kVp beam. Agreement was observed between the equivalent source spectrums derived from measurements using either full- or half- bowtie filters. This consistency indirectly validates the consistency and accuracy of the equivalent source approach, as the experimental data are mutually